PROCESSING ALUMINUM OXIDE FOR THE CONTROL OF MICROSTRUCTURAL TEXTURE AND OPTICAL PROPERTIES

by

Andrew P. Schlup

A Dissertation

Submitted to the Faculty of Purdue University

In Partial Fulfillment of the Requirements for the degree of

Doctor of Philosophy
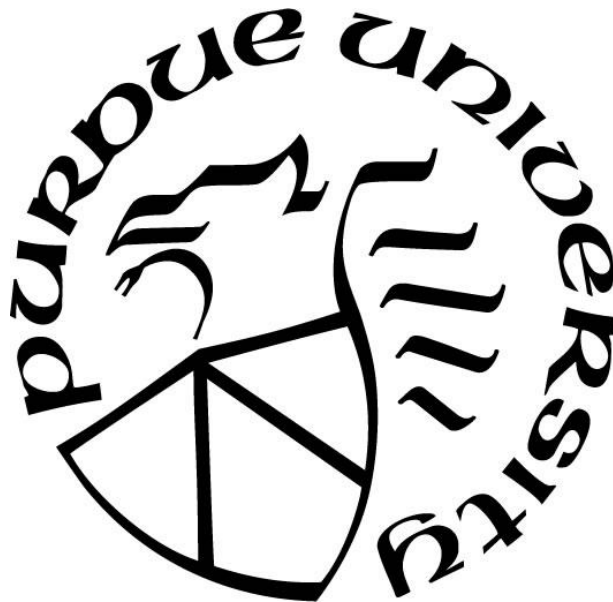
School of Materials Engineering

West Lafayette, Indiana

May 2020

THE PURDUE UNIVERSITY GRADUATE SCHOOL
STATEMENT OF COMMITTEE APPROVAL

Dr. Rodney Trice, Co-Chair

School of Materials Engineering

Dr. Jeffrey Youngblood, Co-Chair

School of Materials Engineering

Dr. Kevin Trumble

School of Materials Engineering

Dr. Elliot Slamovich

School of Materials Engineering

Approved by:

Dr. David Barr

Dedicated to my mother, whose support over the years has been invaluable.

ACKNOWLEDGMENTS

TABLE OF CONTENTS

LIST OF TABLES

LIST OF FIGURES

ABSTRACT

Transparent polycrystalline aluminum oxide is a promising optical material, particularly in applications that require ballistic protection. However, the rhombohedral crystal structure of alumina limits its transparency due to birefringent scattering. One method of reducing birefringent scattering is to align the particles along the same crystallographic direction, minimizing the refractive index mismatch. This dissertation explores the use of high aspect-ratio platelet-morphology alumina powder in order to process a crystallographically aligned polycrystalline alumina part, with improved optical properties. The optimal hot-pressing parameters of non-pre-aligned platelet alumina were explored, showing that a low pre-load pressure (0MPa), a high maximum temperature (1800°C), a low maximum pressure (10MPa), and a long isothermal hold time (>5hrs) yields dense, transparent parts. These parameters resulted in samples with a high in-line transmission (>65%) despite a large grain size (>60µm). This is due to a high degree of crystallographic orientation, which minimizes the refractive index mismatch between grains, reducing birefringent scattering. Pre-alignment resulted in a further increase in crystallographic orientation, indicating that the pre-alignment procedure effectively aligns the platelets along the same crystallographic orientation. However, pre-alignment resulted in a minimal improvement in optical properties due to the pre-aligned platelets decreasing the densification. Mechanical properties were characterized, resulting in a flexure stress and Vickers hardness of approximately 175MPa and 17GPa, respectively. These low mechanical properties are due to the large grain size. The Vickers hardness was also characterized along different alignment/hot-pressing directions, showing that the hardness matches that of sapphire along corresponding crystallographic directions. Modifications to the Rayleigh-Gans-Debye model were made, accounting for crystallographic orientation. The modified model more closely matches the experimental optical data, illustrating the importance of accounting for crystallographic alignment. This dissertation emphasizes the importance of characterizing optical losses in transparent ceramics and how they relate to the microstructure, as well as the significance of crystallographic alignment in a birefringent transparent ceramic like alumina.

1. INTRODUCTION

1.1 Motivation, Background, and Proposed Methods

Transparent alumina is a candidate for protection applications, such as nose cones, radomes, and ballistic blast shields.[1–3] Alumina can reach optical transparency at high relative densities.[4] However, alumina is birefringent due to its anisotropic rhombohedral crystal structure, causing light scattering at the grain boundaries and limiting transparency.[5] There are two main approaches to reduce birefringence effects: decreasing grain size and decreasing refractive index mismatch. The first method, reducing grain size, was first observed by Hayashi et al.[6] then later explored in detail by Apetz.[7] By reducing the grain size, the scattering cross section of an individual grain is decreased, which decreases the scattering intensity, reducing the amount of light that scatters at wide angles relative to the incident beam. This is shown mathematically in Equation 1, also known as the Rayleigh-Gans-Debye model:[7]

$$T_{ILT} = (1 - R_S)exp\left(-\frac{3\pi^2 r_g \Delta n_g^2 d}{\lambda_0}\right)$$
1

Where T_{ILT} is the in-line transmission of a birefringent polycrystalline ceramic, R_S is the surface reflection, r_g is the grain radius (grain size, $G = 2r_g$), Δn_g is the refractive index mismatch between adjacent grains, d is the sample thickness, and λ_0 is the wavelength. As grain size decreases, the in-line transmission will increase. Therefore, controlling the grain size during processing is critical, and is the main approach used by transparent alumina found in the literature.[7–11]

The second method is reducing the refractive index mismatch (Δn_g, also shown in Equation 1) via crystallographic orientation. Some of the earliest uses of this method were shown by Heuer et. al using a sinter-forging method to induce orientation during hot-pressing.[12–14] More recent uses of this method are shown by Mao,[5] Yi,[15] and Suzuki,[16] where a magnetic field is used to orient alumina particles in a suspension, then subsequently densified. The refractive index of alumina along its ordinary axis (c-axis), is $n_{o,645nm} = 1.765$, while the refractive index along its extraordinary axis (a-axis) is $n_{e,645nm} = 1.757$.[17] Therefore, for a maximally birefringent polycrystalline sample, the maximum refractive index mismatch will be $\Delta n_{g,max} = 0.008$. In this hypothetical sample, each

grain must be crystallographically oriented such that the ordinary axis is adjacent to the extraordinary axis of the immediately adjacent grain. Apetz et al.[7] calculated that for an angle of incidence of 45° and the maximum Δn_g (0.008), light will be deflected a maximum of 0.28° from its original direction, which is further exacerbated across several grain boundaries through the thickness of the sample. This example is highly unlikely, as alumina processed using an equiaxed morphology alumina powder will be randomly oriented, resulting in an average refractive index closer to $\Delta n_g = 0.0053$.[7] However, such a Δn_g will still result in significant scattering losses if the grain size is too large, as shown by Equation 1. Therefore, Δn_g must be drastically minimized in order to achieve high transparency if the grain size is large.

It has been shown that light scattering from birefringence can be minimized via this second method, specifically by aligning alumina powders along the same crystallographic direction with a high magnetic field prior to densification.[5,10,15,16] While this alignment method is effective, it may be limited in terms of scalability as the high magnetic fields required (>12T) can only be obtained in small volumes. Therefore, it is important to investigate other methods of alignment. In the case of alumina, it is possible to synthesize powders with a platelet-morphology, where the basal plane of the platelets correspond to the c-plane of the alumina crystal structure.[18–20] Trice et al.[21] found that warm-pressing h-boron nitride platelets in a thermoplastic polymer resulted in an aligned microstructure. In this research, a similar warm-pressing alignment method is adapted to align high aspect-ratio platelet alumina powders. Subsequent binder burnout and hot-pressing should result in a fully-dense and crystallographically aligned polycrystalline alumina sample, with minimized birefringent scattering losses.

1.2   Transparency in Polycrystalline Ceramics: Mechanisms of Optical Loss

When studying transparent ceramics, it is important to have a fundamental understanding of how light interacts with the sample. This is important for characterizing the level of transparency of the sample, as well as identifying where optical losses are occurring. When a light beam interacts with a sample, one of three events can occur:

1. The light can reflect backwards off the sample (Reflection, R)
2. The light can be absorbed as it passes through the sample (Absorption, A)
3. The light can pass through the sample (Total Transmission, T)

Conservation of energy yields Equation 2:

$$I = R + A + T = 100\%$$

2

where I is the incident beam's intensity (the beam from the light source), R is reflectance, A is absorption, and T is total transmission. These three events are shown schematically in Figure 1.1.
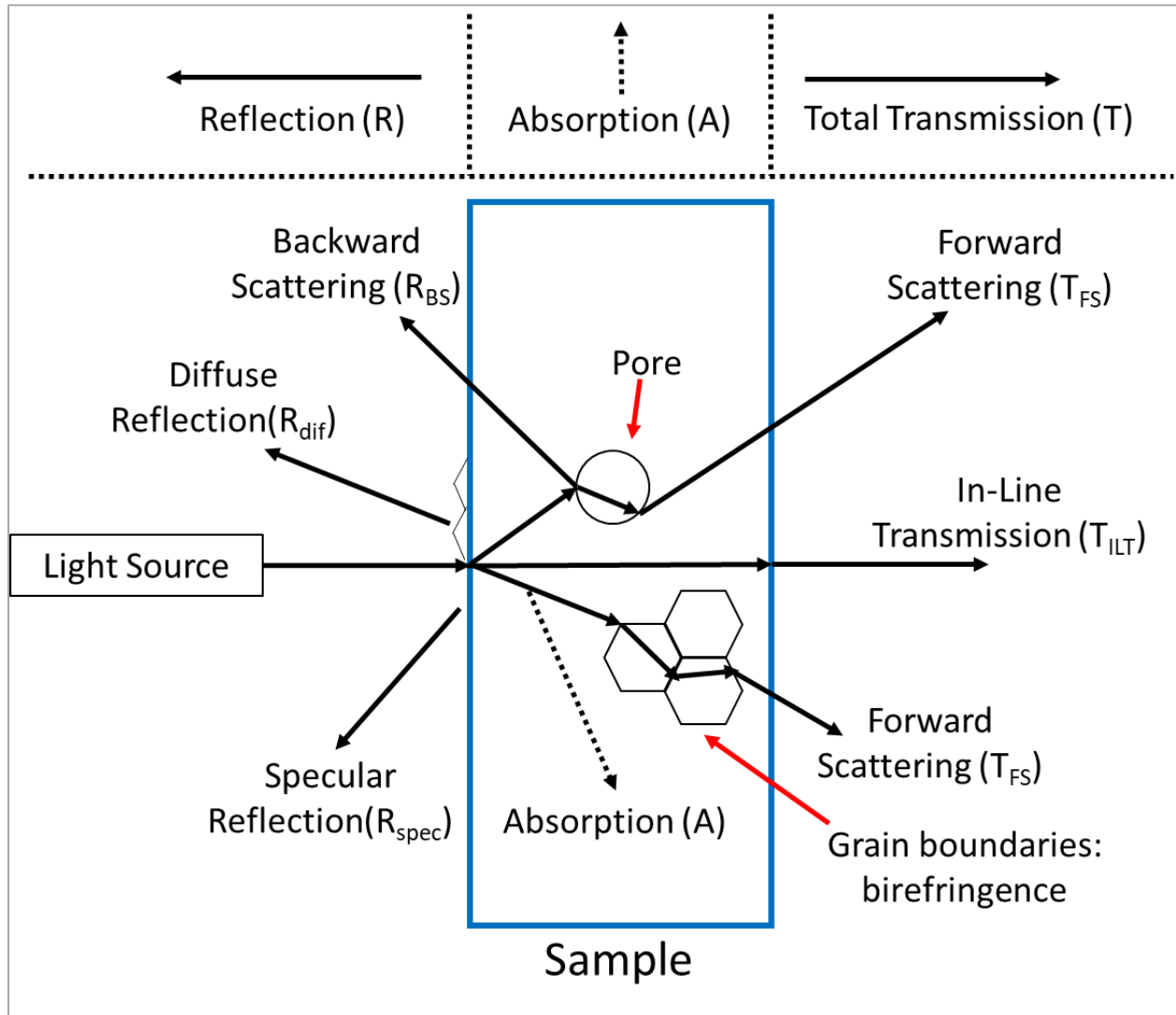
Figure 1.1. Schematic illustrating the different ways in which light can interact with a transparent polycrystalline ceramic sample.

The first event that can occur is reflection, as shown by the left-side of Figure 1.1. This includes all light that reflects backwards from the sample. Reflection can be further defined as the sum of surface reflection (R_S) and backward scattering (R_{BS}), as shown in Equation 3:

$$R = R_S + R_{BS} \qquad\qquad 3$$

Surface reflection is caused by the difference in refractive index between the polished ceramic surface and air. It is due to either smooth (specular reflection, R_{spec}) or rough surfaces (diffuse surface scattering, R_{dif}), as shown in Figure 1.1. In this research, the diffuse surface scattering has been minimized by polishing the surfaces of the samples. Samples had similar surface reflective losses when compared to a polished single-crystal sapphire standard. Therefore, losses due to surface reflection can be ignored if the surfaces of the sample are sufficiently polished.

The other aspect of reflection losses is backward scattering (R_{BS}), which is due to residual porosity in the sample, as shown in Figure 1.1. This arises due to the large refractive index mismatch between the ceramic and a pore. For example, the refractive index mismatch between alumina and a pore is $\Delta n_p = 0.76$.[7] This is not insignificant, and is why relative densities exceeding 99.95% are required to achieve transparency. Therefore, optimal processing is paramount for transparent ceramics, generally requiring high temperatures and pressures.

The second event that can occur when a light beam interacts with a transparent ceramic sample is absorption, as shown by the dotted arrows in Figure 1.1. The light energy lost due to absorption is not "deflected at some angle" as the dotted arrows might suggest. Instead, the light energy is transformed into heat when it interacts with secondary phases and impurities in the sample.[22] Absorption qualitatively manifests as a discoloration in the sample, and as will be shown, several samples in this research have a distinct gray discoloration, which is a common defect observed in transparent spinel.[23,24] In the case of spinel, the primary mechanisms for absorption were identified to be carbon contamination, oxygen vacancies, and impurities in the raw powder. It is believed that similar mechanisms are responsible for the discoloration in the samples produced in this research. By using the direct absorption measurement technique described in a later section, the amount of light lost due to secondary phases can be determined.

The third event that can occur when a light beam interacts with a transparent ceramic sample is total transmission, as shown by the right-side of Figure 1.1. Total transmission can be further

17

defined as the sum of in-line transmission (T_{ILT}) and forward scattering (T_{FS}), as shown in Equation 4:

$$T = T_{ILT} + T_{FS} \qquad\qquad 4$$

A high total transmission does not necessarily mean that a sample is "transparent", as objects observed from a distance can still appear to be hazy due to forward scattering losses. Forward scattering losses are due to two separate things: porosity and birefringence.[7] Porosity causes forward scattering for the same reason as it causes backward scattering: the large refractive index mismatch between the ceramic and a pore. Birefringence causes forward scattering due to refractive index mismatches between adjacent grains, as previously discussed in Section 1.1.

The other aspect of total transmission is in-line transmission, which is defined as the amount of light that transmits through the sample at an angle that is very close to the incident beam. If a sample has a high in-line transmission, objects observed from a distance will qualitatively appear to be "clear" or "less hazy", and vice/versa if it has a low in-line transmission. This is the true measurement of the transparency of a polycrystalline ceramic.[7]

By understanding these different optical properties, as well as the mechanisms of optical loss and how they relate to the microstructure, one can better understand how "transparent", "translucent", or "discolored" a polycrystalline alumina sample is. From there, one is better equipped to process a sample with improved optical properties. Relating optical losses to the microstructure is a common theme in this dissertation.

2. HOT-PRESSING PLATELET ALUMINA TO TRANSPARENCY

2.1 Contributions

The individuals listed below contributed the following tasks:

- Andrew Schlup: Powder preparation, hot-pressing, optical polishing, density measurements, scanning electron microscopy, optical measurements, and data analysis

- William Costakis: X-Ray diffraction measurements

- Dr. Wolfgang Rheinheimer: expertise on the pore-swelling phenomenon

- Monica Viers: Computer aided design (CAD) of the cylindrical graphite hot-press die and sample processing

- Adam Smith: CAD of replacement graphite heating elements and sample processing

2.2 Introduction

In order to study the effects of crystallographic orientation on the transparency of alumina, a high relative density must first be achieved. Relative densities greater than 99.95% are required to achieve transparency in polycrystalline ceramics.[7] There are several different sintering methods used to process alumina to such densities, including pressureless sintering.[5,15,26,27] hot-isostatic pressing (HIP),[7–11] spark plasma sintering (SPS),[16,28–33] and hot-pressing.[13,34] Pressureless sintering experiments performed presently with RonaFlair® platelet alumina powder showed that a relative density of approximately 55% could be achieved (1700°C, 1 hour, air). This low density is due to the powder morphology, as the platelets have a diameter of about 11μm, yielding very low driving forces for sintering. At such low densities, porosity is entirely open porosity, which means that HIP is not available for further densification.[9] Thus, uniaxial pressure as supplied by SPS or hot-pressing is required to densify platelet alumina powder. SPS has received much attention for

densifying transparent ceramics, including spinel[35–39] and alumina.[16,28–33] However, for both spinel[36] and alumina,[31] it has been found that lower heating rates (2 to 10°C/min) resulted in samples with higher transmission. The necessity of lower heating rates defeats the primary benefit of SPS over hot-pressing, i.e. the ability to heat at rates >100°C/min, which is beneficial for maintaining small grain sizes and decreasing processing time.[40] Graphite hot-press furnaces are a cost-effective alternative, they are capable of heating rates up to 50°C/min, and pressures are only limited by the grade of graphite and die design. These characteristics make hot-pressing a promising candidate for densifying platelet alumina powder to transparency.

There is a plethora of research on hot-pressed alumina[41–46] with few investigators reporting attempts to hot-press alumina to transparency. Peelen[4,34] showed that alumina could be sintered to transparency using a continuous hot-pressing method.[47] However, this method requires extremely specialized equipment and precisely machined high-strength alumina dies, a stark contrast to the common graphite dies that are used in conventional hot-pressing. Heuer et al.[12–14,48] showed that alumina can be hot-pressed to transparency using a method they termed 'sinter-forging'. This sinter-forging method is similar to HP in that a conventional HP furnace and graphite dies are used, but it is different in that uniaxial pressure is not applied until the max temperature, allowing the powder compact to pressureless sinter to ~60% relative density. They found that when the pressure is slowly applied at the max temperature, the undersized alumina billet will shrink in the axial direction and expand in the radial direction, inducing substantial strain in the compact. This strain resulted in primary recrystallization, where the pores and some grain boundary regions in the undersized compact were thought to serve as the strain-free nucleation sites.[14] After recrystallization, the pores are located along the grain boundaries, and subsequent annealing at max temperature and pressure is sufficient to fully densify the recrystallized matrix by vacancy flow, resulting in a transparent alumina part. A schematic of this recrystallization and densification process is given by Heuer.[14] However, Heuer et al. used an equiaxed-morphology alumina powder in their studies,[12–14,48] as have all other studies aiming to produce transparent alumina.[1–5,7–11,15,16,26–33] To the extent of the author's knowledge, there have been no reported attempts to hot-press platelet-morphology alumina powder to transparency.

In this chapter, the sintering behavior and resulting optical properties of hot-pressed platelet alumina powder with no intentional alignment prior to hot-pressing (non-pre-aligned) will be explored. The effects of hot-pressing parameters on the densification and optical properties of

platelet-morphology alumina will be discussed, with an emphasis on the optical losses and how they are manifested in the samples. A large array of samples were processed, studying the effects of maximum temperature, powder heat-treatment, pre-load pressure, and isothermal hold time.

2.3   Experimental Methods

2.3.1   Powder Preparation

RonaFlair® White Sapphire (Merck KGaA, EMD Performance Materials) platelet alumina powder was used. It has a platelet morphology as shown in Figure 2.1, with a diameter and thickness of approximately 11 and 0.5 µm, respectively. The impurity content of the powder was measured via inductively coupled plasma mass spectrometry (ICP-MS), and was found to contain 0.012% Ca, 0.002% Cr, 0.018% Fe, 0.001% K, 0.26% Na, 0.015% Si, and 0.002% Ti (weight percent). The platelet alumina powder was washed in ethanol and heated at 105°C overnight in air to evaporate the ethanol, then sieved through a 250µm nylon mesh to break apart soft agglomerates (P1 in Table 2.2). For some samples, the ethanol-washed/evaporated powder was heated-treated at 1100°C for 1 hour in air prior to sieving (P2 in Table 2.2). The specific surface area of the ethanol-washed and heat-treated powder was 2.00 ± 0.03 and 1.13 ± 0.02 m^2/g, respectively, as measured by the Brunauer–Emmett–Teller (BET) method. The mass-loss of the ethanol-washed and heat-treated powders were measured by high-temperature thermogravimetric analysis (TGA) under flowing air.
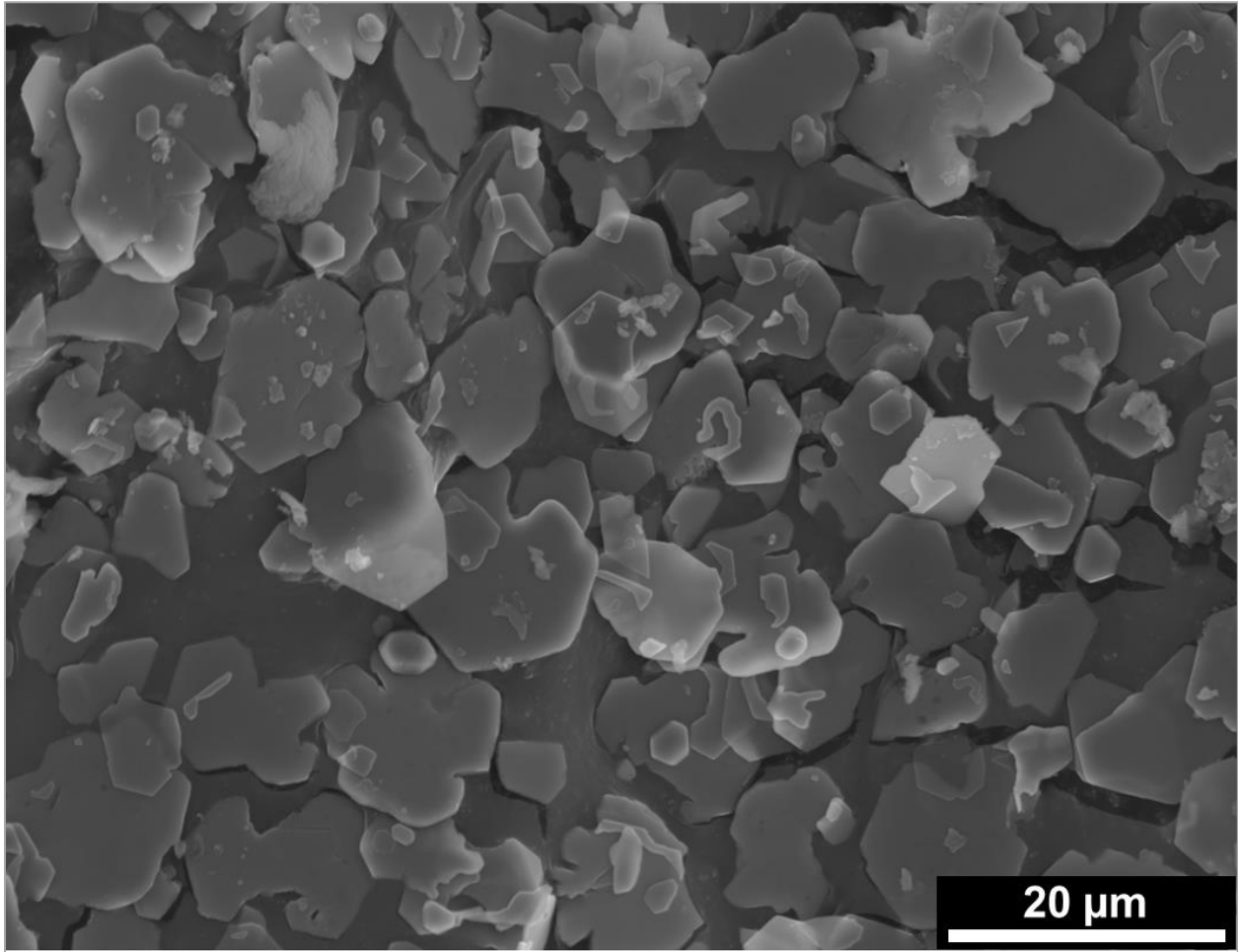
Figure 2.1. SEM micrograph of ethanol-washed (P1) RonaFlair® platelet-morphology alumina powder.

2.3.2 Hot-Pressing

Hot-pressing was performed using a cylindrical graphite die with an inner diameter of 25.4mm. Molybdenum foil sheets (0.14mm thick) were placed above and below the powder bed, and a layer of graphoil (0.26mm thick) and boron nitride spray between the molybdenum sheets and the graphite spacers, as shown in Figure 2.2. This assembly prevented the alumina samples from bonding to the graphite spacers, and reduced carbon contamination from the graphite die. 6.0 grams of the sieved powder were poured into the graphite die, and uniaxially cold-pressed at approximately 7 MPa to initially consolidate the powder (determination of the green density of the powder compacts at this stage is discussed below). The resistively-heated graphite hot-press furnace (Centorr, Testorr™ series) was constructed such that it sits within a hydraulic load frame

22

(MTS, Model 312.21). The assembled graphite die was placed in the furnace chamber and a vacuum was pumped for approximately 12 hours, until a 40 to 50 millitorr (5.3 to 6.7 Pa) vacuum was achieved, and a vacuum of better than 150 millitorr (20 Pa) was maintained from room temperature to 1550°C. At 1550°C, the vacuum was turned off and the furnace chamber was backfilled with high-purity gettered nitrogen, which continuously flowed at approximately 4 liters/min and 2psi (1.4×10^4 Pa) for the remainder of the hot-press run. A vacuum atmosphere was reported to be beneficial for removing volatiles during hot-pressing of transparent ceramics.[39] However, alumina will severely react with graphite in a vacuum atmosphere above 1600°C,[44,49] whereas only minimal reactions were observed in a nitrogen atmosphere even up to 1825°C in the present study. The pre-load pressure (P_i, 0 to 8 MPa) was applied to the die at room temperature and maintained during heating (25°C/min) to the maximum temperature. For P_i = 0 MPa, the top platen of the load frame was positioned ~5mm away from the top ram of the assembled hot-press die, allowing the die to expand freely during heating. The furnace was controlled by a C-type thermocouple positioned near the edge of the graphite die for temperatures up to 1500°C, and a pyrometer viewing the edge of the graphite die for temperatures above 1500°C. When the furnace reached the maximum temperature (T_{max}, 1750 to 1825°C), the maximum pressure (P_{max}, 2.5 to 80 MPa) was applied at a rate of 1.3 MPa/min. After the maximum pressure was achieved, the furnace was held at T_{max} and P_{max} for the isothermal hold time (t_{iso}, 1 to 7 hours). The pressure was removed prior to cooling (25°C/min), and the ~2.8mm thick transparent alumina sample was removed from the die. Load and ram displacement were recorded throughout the run. A schematic illustrating the hot-pressing parameters is shown in Figure 2.3.
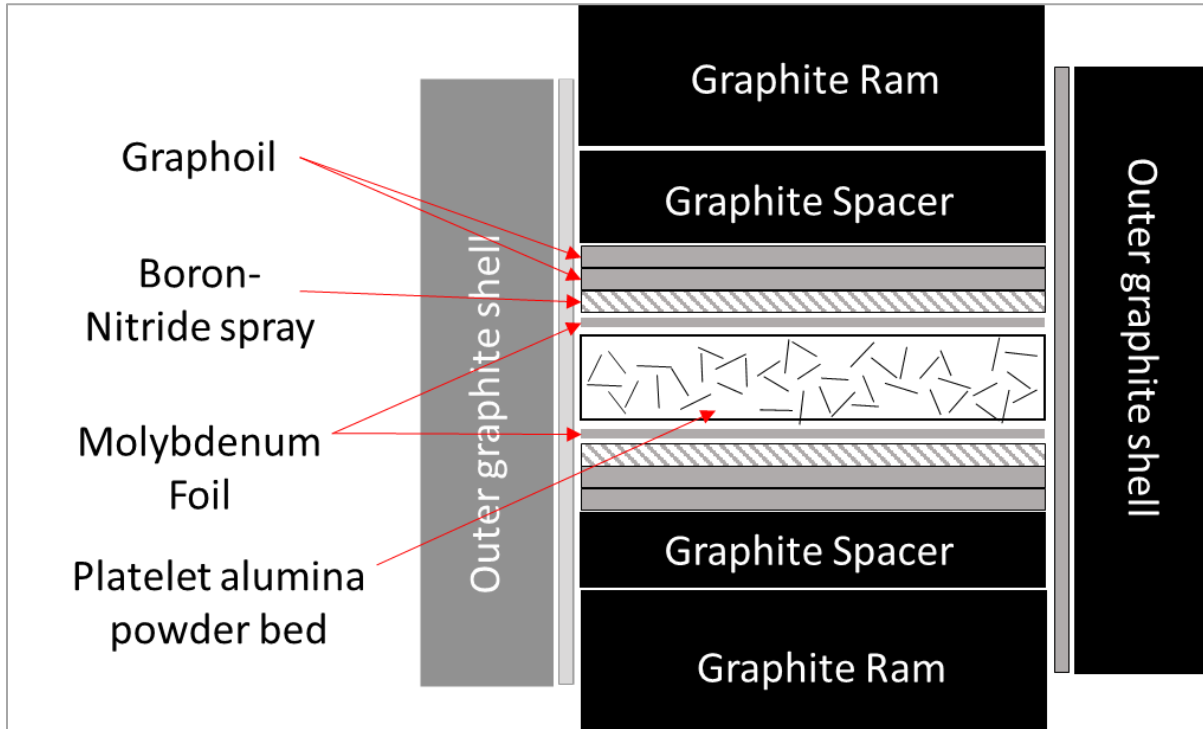
Figure 2.2. Schematic of hot-press die assembly.
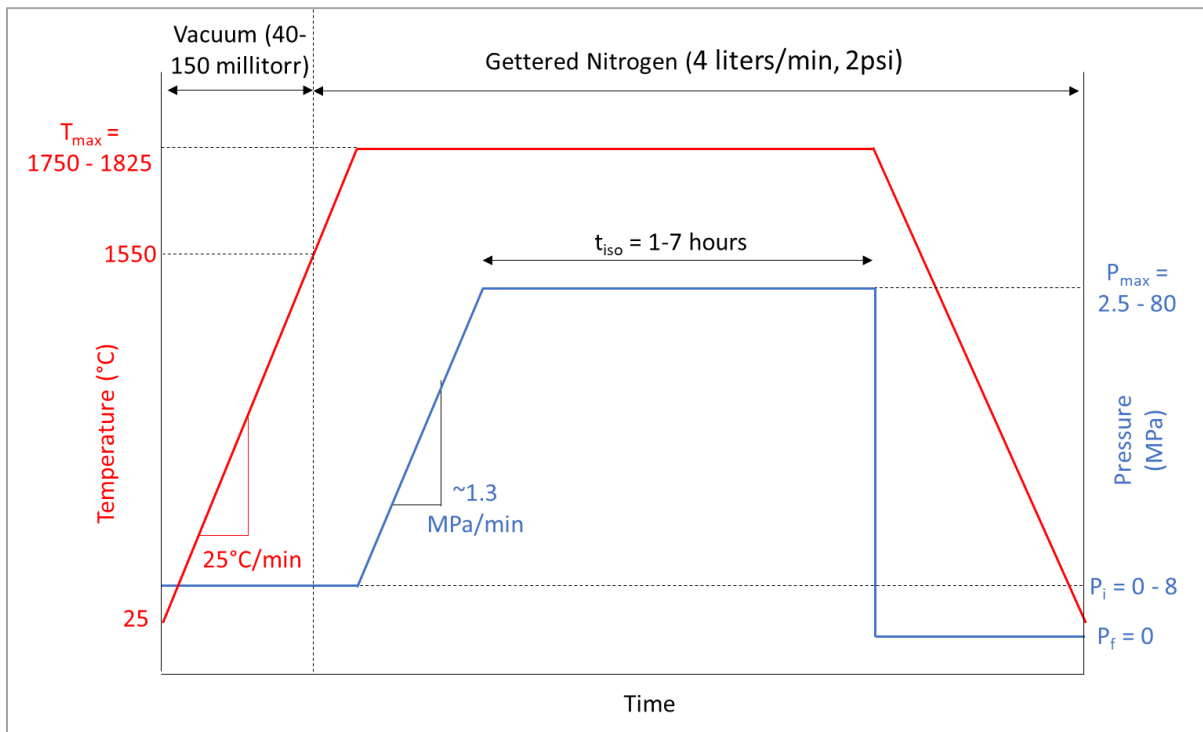
Figure 2.3. Schematic illustrating the hot-pressing parameters.

2.3.3 Optical Polishing

Hot-pressed samples were ground and polished to minimize surface scattering. A 100-grit metal-bonded diamond grinding wheel was used to machine equal amounts of material from each side of the samples to a thickness of approximately 1.5mm. Both sides of the samples were polished using progressively finer diamond grinding pads and/or suspensions, as shown in Table 2.1. Such long polishing times (sometimes 6 hours per step) were required to polish past the significant amount of grain pull-out. The polished samples resulted in final thicknesses ranging from 1.15 to 1.40mm.

Table 2.1. Polishing parameters for hot-pressed transparent alumina samples.

Step #	Grit size (µm) & type	Pad type	Time (min)	Load (N)	Platen Speed (rpm) & direction	Head Speed (rpm) & direction	Lubricant
1	77 (pad)	[a]Cameo	2	37	300, [d]CCW	150, [e]CW	Water
2	44 (pad)	Cameo	10	37	300, CCW	150, CW	Water
3	30 (pad)	Cameo	10	37	300, CCW	150, CW	Water
4	15 ([c]sus.)	[b]DiaMat	30	37	160, CCW	150, CW	[b]GreenLube™
5	9 (sus.)	DiaMat	60	37	160, CCW	150, CW	GreenLube™
6	6 (sus.)	[b]Gold Label	360	37	160, CCW	150, CW	GreenLube™
7	3 (sus.)	[b]White Label	120	37	160, CCW	150, CW	GreenLube™
8	1 (sus.)	White Label	180	37	160, CCW	150, CW	GreenLube™

Notes:
[a]Product of LECO
[b]Product of Allied High Tech
[c]"sus." is an abbreviation for "suspension". Allied High Tech suspensions were used
[d]CCW = Counter Clock-Wise
[e]CW = Clock-Wise

2.3.4 Density Measurements

The geometric green-body densities of the powder compacts at the start of a given hot-press run were determined. The mass of powder (6.0g) and diameter of the compacts (25.4mm) are constants, but the height of the compact will change depending on the powder type (EtOH-wash vs. heat-treated) and pre-load pressure (0 to 8MPa), resulting in different green-body densities. The heights of the compacts were determined by subtracting the height of an empty (no powder) hot-press die under a given pre-load pressure from the height of a prepared (6.0g of powder) hot-press die under the same pre-load pressure. Geometric green-densities can then be calculated with this height, and are shown in Table 2.2. The densities of the hot-pressed samples were measured using the Archimedes method,[50] accounting for the temperature-density dependency of the

distilled water (21.2°C), resulting in a standard error of ±0.09%. A commercially available piece of single-crystal sapphire was measured alongside the hot-pressed samples, resulting in a density of 3.977 g/cm^3. Relative densities of the samples were calculated by dividing their density by the density of the single-crystal sapphire standard, and are listed in Table 2.2.

2.3.5   X-Ray Diffraction

The crystallographic orientation of the hot-pressed samples were determined via X-Ray Diffraction (XRD) on a Panalytical Empyrean Diffractometer (Malvern Panalytical Ltd, Royston, UK). The instrument was equipped with a bent Ge incident beam monochromator that is tuned to transmit Cu Kα_1 radiation. Intensity was measured from a 2θ of 20 to 95°. Scans of the top surfaces of the samples were obtained, and maximum intensities were normalized to a value of 1 for ease of comparison.

2.3.6   Scanning Electron Microscopy

Cross sections of the samples were polished to a 1µm diamond finish using a procedure similar to what is shown in Table 2.1, and thermally etched at 1600°C for 30 minutes in air. The samples were sputter-coated with Au-Pd, and the microstructures were observed by scanning electron microscopy (SEM) with a FEI Quanta650 at 10kV. Line intercept analysis was performed, obtaining at least 200 intersections. The average intercept length was multiplied by the geometric factor 1.56 to obtain the average grain size.

2.3.7   Optical Measurements

Optical measurements were made using a PerkinElmer Lambda 950 UV-VIS-NIR spectrophotometer equipped with an integrating sphere. The visible spectrum was measured from 200-800nm using a photomultiplier tube (PMT) detector, and the near-infrared (IR) spectrum was measured from 1000-2500nm using a lead sulfide (PbS) detector. A wavelength of 645nm was chosen as the representative value for optical properties in the present study, which is a similar wavelength used in the literature.[7,9,11] Total transmission, in-line transmission, reflection, and absorption can be measured using the spectrophotometer, and the forward and backward scattering

can be derived from them. Figure 2.4 schematically illustrates how the sample is placed in the UV-Vis to obtain these different measurements.
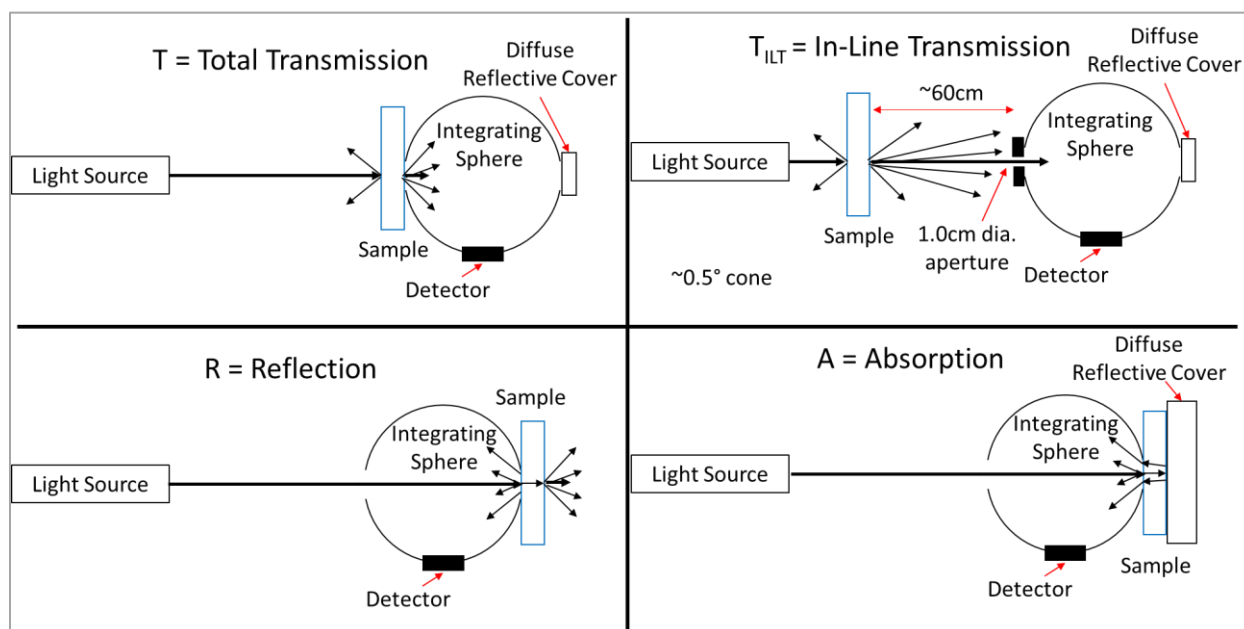
Figure 2.4. Schematic illustrating the different optical measurements. Configuration and sample size are not to scale.

Total transmission (T_T) was measured by placing the sample directly against the edge of the integrating sphere, allowing all light that passes through the sample to enter the integrating sphere and be measured. In-line transmission (T_{ILT}) was measured by positioning the sample approximately 60cm away from a 1.0cm diameter aperture placed in front of the integrating sphere. Given the distance between the sample and the aperture, as well as the diameter of the aperture, all light that is scattered at an angle greater than an approximately 0.5° cone is not measured. This falls under the definition of "Real In-Line Transmission", as defined by Apetz et al.[7] Reflection (R) was measured using an arrangement similar to that of Apetz et al.,[7] where the sample was placed directly against an inlet on the back-side of the integrating sphere. Absorption (A) was measured using a configuration similar to the reflection measurement, except a diffuse reflective cover was placed behind the sample. The absorption measurement is described in greater detail below.

The optical loss mechanisms, absorption (A), forward scattering (T_{FS}), and backward scattering (R_{BS}), are calculated by the following Equations:

$$A = \frac{I - I_{raw}}{2} \qquad 5$$

$$T_{FS} = T_T - T_{ILT} \qquad 6$$

$$R_{BS} = R - R_S \qquad 7$$

Where I is the incident beam, I_{raw} is the raw light intensity measured by the detector during the absorption measurement, and R_S is the surface reflection of a single-crystal sapphire sample that was ground/polished using the same procedures as the hot-pressed samples. The optical properties of the sapphire sample were measured and used as a comparison.

Absorption was directly measured in this research. This was done by placing the samples against an inlet positioned behind the integrating sphere and a diffuse reflective cover placed behind the sample, as shown in Figure 2.4 and in even further detail in Figure 2.5. This configuration, along with a simple Newtonian ray-diagram analysis, allows for a direct measurement of absorption. The incident beam, I, enters the integrating sphere and hits the sample, and some amount of light is reflected at the surface, R_S. The incident beam minus the surface reflectance beam continues to transmit through the sample, and some amount of it is lost due to absorption, A_1. The beam reflects off the diffuse reflective cover and is transmitted back through the sample a second time, and some amount of it is lost due to absorption again, A_2. The raw light intensity, I_{raw}, includes the surface reflection and the light that passed through the sample (indicated by bold arrows in Figure 2.5), and is given by Equation 8:

$$I_{raw} = I - R_S - A_1 - A_2 + R_S \qquad 8$$

The surface reflection value cancels out, and for the absorption $A_1 = A_2 = A$ holds. Solving for A gives Equation 5.
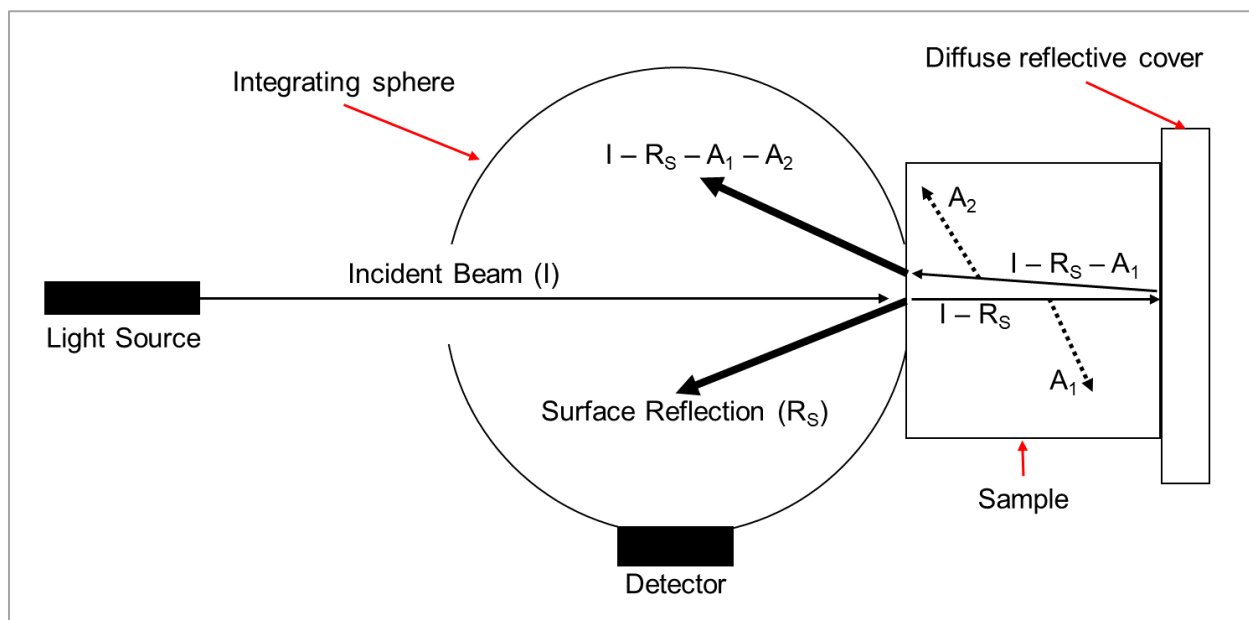
Figure 2.5. Ray diagram illustrating direct measurement of light absorption (modified from Apetz et al.[7]). The bold arrows indicate the raw light intensity that is measured by the detector (I_{raw}), and the dotted lines indicate the light lost to absorption ($A_1 = A_2 = A$). This configuration and sample size are not to scale.

2.3.8   Normalizing Optical Properties to Sample Thickness

Total transmission, in-line transmission, forward scattering, backward scattering, and absorption of transparent polycrystalline ceramics are all thickness-dependent.[3] A thicker sample will have a lower total and in-line transmission, and a higher forward scattering, backward scattering, and absorption. Grinding and polishing the hot-pressed samples to a consistent thickness was challenging, so it was necessary to normalize the optical properties of the samples to the same thickness. A modified version of Krell et al.'s equation[9] was used to normalize the optical properties of the hot-pressed samples to a thickness of 0.8mm, which is the thickness most commonly reported in the literature.[5,7,9,11,16,31,33] Transmission was normalized via Equation 9:

$$T_n = (T_{SCS}) \left(\frac{T_m}{T_{SCS}} \right)^{\frac{d_n}{d_m}} \qquad\qquad 9$$

Where T_n is normalized transmission, T_m is measured transmission, d_n is normalized thickness, d_m is measured thickness, and T_{SCS} is the transmission of the single-crystal sapphire standard. This

equation was used to normalize both total and in-line transmission, and normalized forward scattering was then calculated by using these normalized transmission values in Equation 6.

Reflection was normalized via Equation 10:

$$R_n = (R_S) \left(\frac{R_m}{R_S}\right)^{\frac{d_n}{d_m}}$$

10

Where R_n is normalized reflection, R_m is measured reflection, and R_S is the surface reflection of the polished single-crystal sapphire standard. Normalized backward scattering was then calculated by using this normalized reflection in Equation 7.

The raw light intensity that is used to calculate absorption (Equation 5) was normalized via Equation 11:

$$I_{raw,n} = (I_{SCS}) \left(\frac{I_{raw,m}}{I_{SCS}}\right)^{\frac{d_n}{d_m}}$$

11

Where $I_{raw,n}$ is the normalized raw light intensity, $I_{raw,m}$ is the measured raw light intensity, and I_{SCS} is the raw light intensity of the single-crystal sapphire standard.

2.4 Results and Discussion

2.4.1 Effect of Maximum Temperature

The maximum temperature (T_{max}) during hot-pressing is important as there must be enough thermal activation to achieve adequate diffusion for densification. Figure 2.6 shows the ram displacement over time for samples hot-pressed at T_{max} between 1750 and 1825°C. The displacement was normalized to zero at time equal to zero to show the total amount of displacement for each sample. To observe the sintering behavior during heating, a small pre-load pressure (P_i = 2MPa) was applied. All curves initially increase due to thermal expansion, then begin to shrink at approximately 1175°C, indicating the onset of densification. An anomaly in the data is observed for all curves at ~1550°C, where the samples appear to suddenly expand then shrink. This expansion/shrinkage is due to the furnace chamber being backfilled with gettered nitrogen, which

changes the pressure being exerted on the load cell. At T_{max} (1750°C to 1825°C), the sudden shrinkage is due to the application of the maximum pressure. The onset of this shrinkage is offset by 1 minute for the different T_{max} because the respective temperature is reached after different times at a constant heating rate of 25°C/min. At the onset of pressure application, the rate of displacement is higher at higher maximum temperatures. This is because alumina will plastically deform more readily at higher temperatures.[14] After approximately 1.3hr, the slope of each curve spontaneously decreases, which is discussed in more detail in a later section. Once the maximum pressure is reached after about 1.7hr, continued shrinkage is minimal, as the powder bed has nearly completely densified.
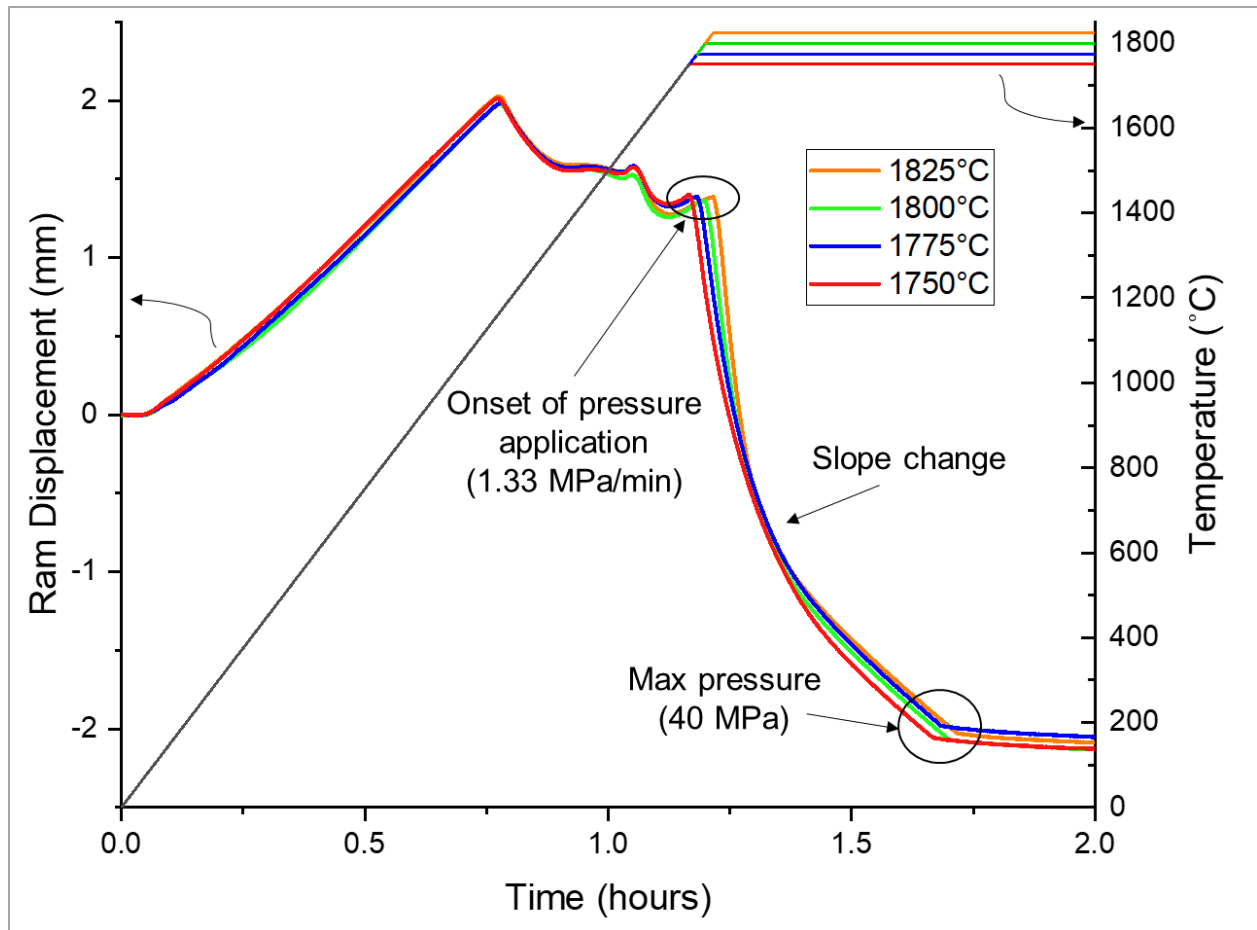
Figure 2.6. Ram displacement versus time of samples hot-pressed at different maximum temperatures.

Table 2.2. Processing parameters and microstructural properties of hot-pressed alumina samples.

Sample ID	Powder & treatment	Hot-Pressing Parameters				Relative Density (%TD)		Grain size (µm)
		Max Temperature, T_{max} (°C)	Pre-Load Pressure, P_i (MPa)	Max Pressure, P_{max} (MPa)	Isothermal Hold Time, t_{iso} (hours)	Green-body (geometric)	Hot-pressed (Archimedes, ±0.09%)	
P1-1750-2-40-5	P1	**1750**	2	40	5	45.1	99.74	34.1±3.3
P1-1775-2-40-5	P1	**1775**	2	40	5	45.1	99.74	38.6±5.0
P1-1800-2-40-5	P1	**1800**	2	40	5	45.1	99.82	52.3±6.3
P1-1825-2-40-5	P1	**1825**	2	40	5	45.1	99.80	75.7±15.3
P2-1800-0-40-5^a	P2	1800	**0**	40	5	37.2	99.81	61.1±8.6
P2-1800-2-40-5	P2	1800	**2**	40	5	40.2	99.64	57.2±8.4
P2-1800-4-40-5	P2	1800	**4**	40	5	41.2	99.80	49.9±6.1
P2-1800-8-40-5	P2	1800	**8**	40	5	43.3	99.89	45.4±6.5
P2-1800-0-2.5-5	P2	1800	0	**2.5**	5	37.2	99.09	69.8±15.0
P2-1800-0-5-5	P2	1800	0	**5**	5	37.2	99.66	57.7±11.7
P2-1800-0-10-5	P2	1800	0	**10**	5	37.2	99.93	61.8±11.6
P2-1800-0-20-5	P2	1800	0	**20**	5	37.2	99.81	57.2±7.2
P2-1800-0-40-5	P2	1800	0	**40**	5	37.2	99.81	61.1±8.6
P2-1800-0-80-5	P2	1800	0	**80**	5	37.2	99.79	60.2±10.8
P2-1800-0-10-1	P2	1800	0	10	**1**	37.2	99.68	29.3±2.1
P2-1800-0-10-3	P2	1800	0	10	**3**	37.2	99.72	43.4±5.6
P2-1800-0-10-5	P2	1800	0	10	**5**	37.2	99.93	61.8±11.6
P2-1800-0-10-7	P2	1800	0	10	**7**	37.2	99.89	64.7±9.3
E3-1825-0-40-5^a	E3	1825	0	40	5	N/A	99.96	92.0±20.3

Note:

The significance of the bold in the table is to highlight different sets of samples.

Powder P: Platelet morphology alumina powder, RonaFlair® White Sapphire, Merck KGaH.

Powder E: Equiaxed morphology alumina powder, AA03, Sumitomo

Treatment 1: Ethanol-washed

Treatment 2: Ethanol-washed & heat-treated at 1100°C for 1hr in air

Treatment 3: As Received

[a]Sample replicated with similar powder and parameters as Sellers et al.[48]

It was found that an increase in T_{max} resulted in a minimal change in final sample densities and a significant increase in grain size, as shown in Table 2.2. Samples sintered at a T_{max} of 1750 and 1825°C have a grain size of 34 and 75 µm, respectively. Heuer et al[12–14,48] used equiaxed alumina at T_{max} between 1810 and 1880°C to fabricate transparent samples, resulting in grain sizes on the order of 50 µm. One such sample hot-pressed at T_{max}=1880°C resulted in a grain size of 46 µm.[12] The larger grain size at lower temperatures observed in the current study may be due to the larger starting particle size (11 µm diameter) of the platelet-alumina powder, compared to the 0.3 µm diameter equiaxed alumina powder used by Heuer et al.[12–14,48]

The optical properties of samples hot-pressed at different T_{max} are shown in Figure 2.7. The total and in-line transmission both increase with increasing T_{max}. There are minimal losses due to backward scattering, which implies that these samples have very little porosity, as supported by the high relative densities of these samples (Table 2.2). Most of the optical losses are due to forward scattering and absorption, which decrease with increasing temperature. Accordingly, these samples still have significant birefringence effects and impurities. A gray discoloration is observed in the bulk of all samples, and a severe black discoloration is observed at the outer perimeter of the sample hot-pressed at 1825°C (P1-1825-2-40-5). The reason for this is not clearly understood. However, 1825°C is close to the eutectic between alumina and aluminum-carbide,[51] so there may be some reaction occurring between the graphite die and the alumina powder. 1800°C was chosen as the optimal T_{max} to prevent such a reaction, but discoloration is still present in the interior of the hot-pressed samples. Therefore, parameters that have been reported to minimize this discoloration were explored.
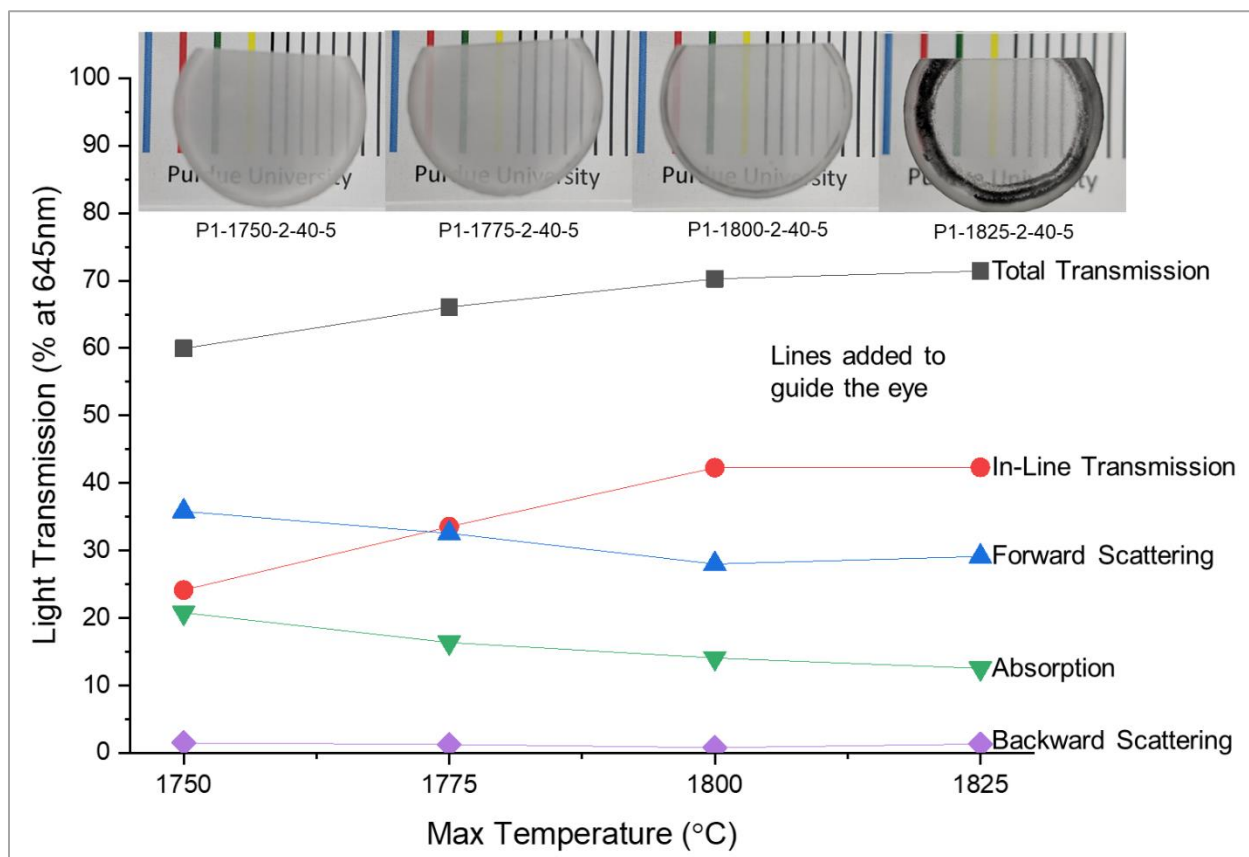
Figure 2.7. Light transmission as a function of maximum temperature, normalized to d = 0.8mm. Samples are placed 2cm above the colored lines, in order of increasing temperature.

2.4.2 Effect of Powder Heat-Treatment and Pre-Load Pressure

The discoloration observed in the hot-pressed alumina samples is a defect that is common in transparent spinel.[23] Two methods were found in the literature that reduce this defect: a heat-treatment of the powders prior to densification,[52] and an application of different pre-load pressures (P_i) during heating.[24,37] Both methods were explored in the current study.

Figure 2.8 shows the ram displacement versus time for samples hot-pressed with or without a powder heat-treatment, and at different pre-load pressures (P_i). Samples with P_i = 2, 4, and 8 MPa initially expand due to thermal expansion. No such expansion is observed for P_i = 0MPa because the top platen of the load frame was not in contact with the assembled hot-press die, allowing the die to expand freely during heating. Samples hot-pressed at higher pre-load pressures expand at a slower rate, which is likely due to the higher pre-load pressures promoting particle rearrangement. Shrinkage begins at 1175°C for the ethanol-washed powders, and 1250°C for the

34

heat-treated powders, indicating the onset of densification. This onset of densification at a lower temperature for the ethanol-washed powders may be due to it having a higher green-body density than the heat-treated sample: 45.1% (P1-1800-2-40-5) vs. 40.2% (P2-1800-2-40-5), as shown in Table 2.2. However, when the onset of densification begins for the heat-treated powder samples, it occurs at a much faster rate than the ethanol-washed powder sample, and samples hot-pressed with higher P_i undergo more shrinkage (densification) during this stage due to the increased driving force for sintering from the applied P_i.[42] It is likely that by heat-treating the powder prior to densification, impurities in the powder are removed,[23] which may allow the powder to densify more readily. High-temperature TGA of the different powder types showed that mass loss initiated around 825°C and 1200°C for the ethanol-washed powders and heat-treated powders, as shown in Figure 2.9. This confirms that some volatile species are being driven from the powders during the heat-treatment. Chemical analysis of the powder indicates that sodium is the most prevalent impurity. The sodium is likely in the form of either sodium carbonate or sodium oxide, both of which thermally decompose well below the heat-treatment temperature of 1100°C.[53,54]
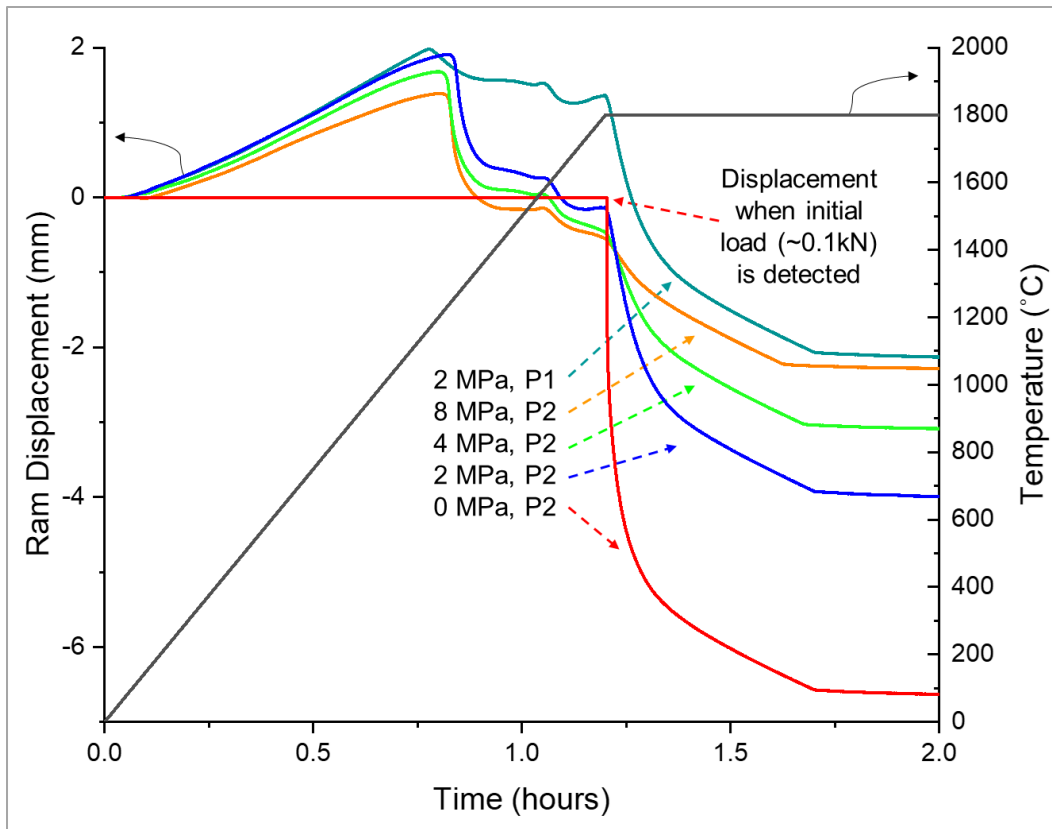
Figure 2.8. Ram displacement versus time of ethanol-washed (P1) and heat-treated (P2) samples hot-pressed at different pre-load pressures.
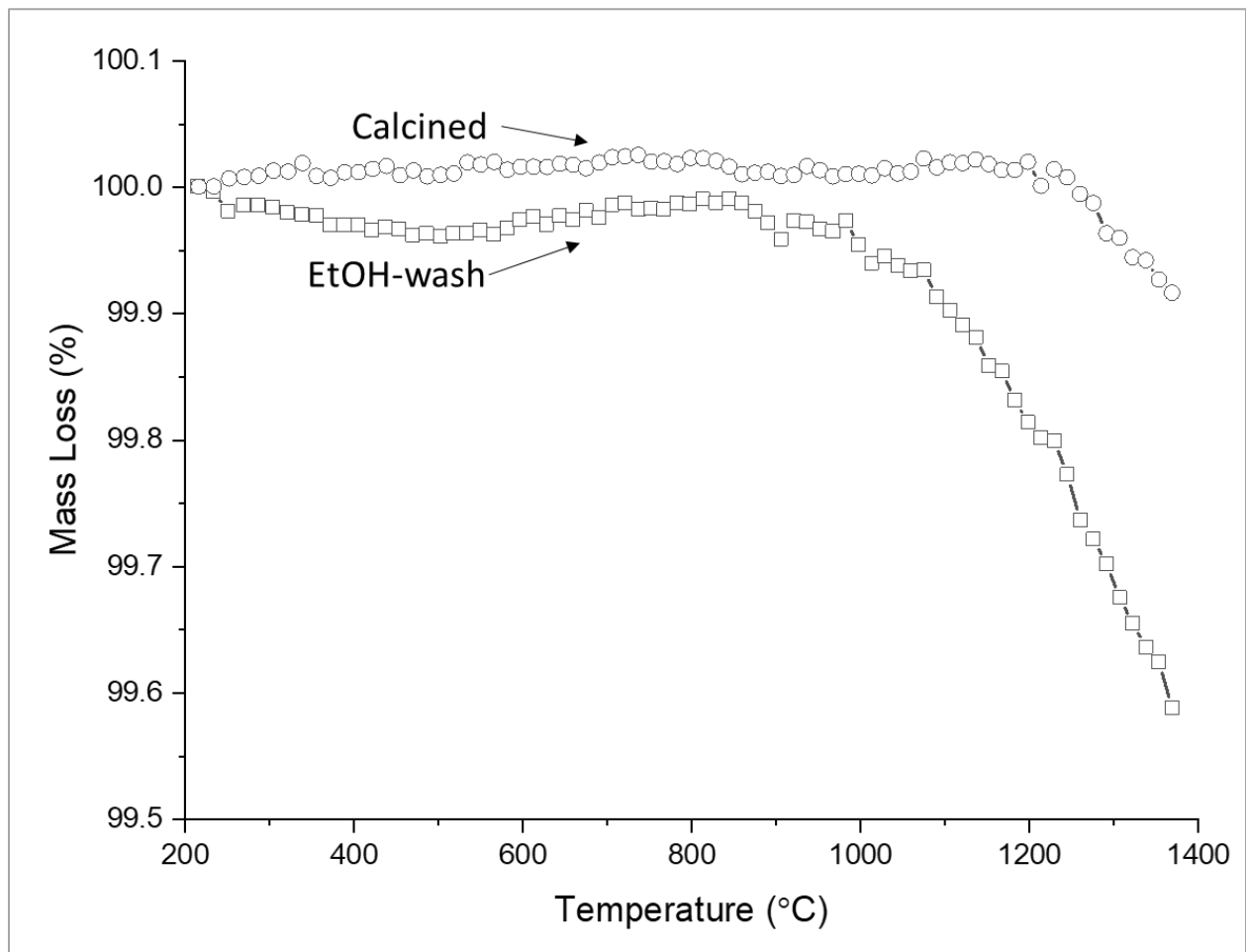
Figure 2.9. Thermogravimetric analysis of ethanol-washed (P1) and heat-treated
(P2) platelet alumina powders.

At the maximum temperature (T_{max} = 1800°C), the maximum pressure (P_{max} = 40MPa) is slowly applied at a rate of 1.3 MPa/min. During this pressure-application step, the ethanol-washed powder (2MPa, P1) experienced ~3.4mm of shrinkage, while the heat-treated powder (2MPa, P2) experienced ~3.8mm of shrinkage. This difference in shrinkage is due to the ethanol-washed powder having a higher green density at the start of the hot-press run, as shown in Table 2.2. Additionally, the shrinkage during this step increases with decreasing pre-load pressure: ~1.7mm at P_i = 8MPa and ~6.6mm at P_i = 0MPa. This is because the green densities at the start of the hot-press run are lower at lower pre-load pressures (Table 2.2), yielding a greater amount of displacement when the maximum pressure is applied. For all samples, the slope of the curves

spontaneously decreases after approximately 1.3hr, similar to the behavior observed in Figure 2.6, and is discussed in more detail in a later section.

The effects of the powder heat-treatment on the optical properties are shown in Figure 2.10. The ethanol-washed sample at P_i = 2MPa (open shapes, P1-1800-2-40-5) has inferior optical properties compared to the heat-treated sample at P_i = 2MPa (closed shapes, P2-1800-2-40-5). Losses due to absorption decreases for the heat-treated sample, suggesting that heat-treating the powder at 1100°C in air prior to hot-pressing causes impurities to be driven off. Morita et al.[52] found that heat-treating spinel powder prior to SPS improved the in-line transmission by 10%, which they claim to be due to impurities being reduced during the heat-treatment. In the current study, the heat-treatment increased the in-line transmission of the hot-pressed platelet alumina by approximately 4%. As previously mentioned, high-temperature TGA indicates that some volatile species are being driven from the powders during the heat-treatment, and sodium is likely the primary impurity being driven off. The removal of the sodium impurity from the powder prior to hot-pressing may explain the decrease in absorption losses for the heat-treated samples. Additionally, TGA showed that some mass loss is still occurring beyond 1100°C (Figure 2.9), suggesting that a higher heat-treatment temperature, or even longer heat-treatment time, may additionally purify the powders and further reduce optical losses due to absorption.
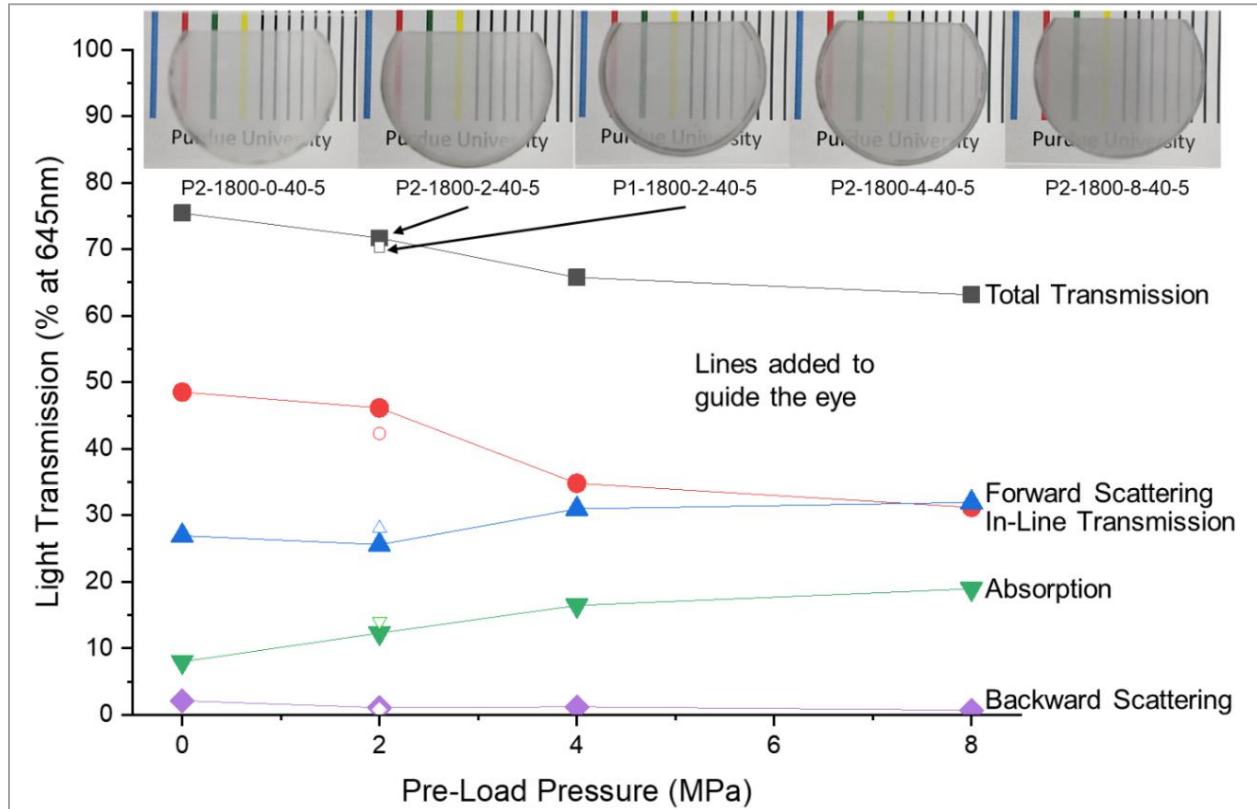
Figure 2.10. Light transmission as a function of pre-load pressure, normalized to d = 0.8mm. Open points are samples with ethanol-washed powder (P1), and closed shapes are samples with heat-treated powder (P2). Samples are placed 2cm above the colored lines, in order of increasing pressure.

Pre-load pressure has a more significant effect on the optical properties than heat-treatment, as shown in Figure 2.10. The total and in-line transmission both decrease as P_i is increased. P_i has minimal effect on losses due to backward and forward scattering, suggesting that it has a minimal effect on the porosity. The similarities in the hot-pressed densities of these samples confirm this (Table 2.2). Losses due to absorption, however, notably increase with increasing P_i. Wang et al.[37] observed a similar qualitative trend in spark plasma sintered spinel and attributed this to dislocations formed during densification. However, Merac et al.[24] found that for hot-pressed spinel, it was beneficial to wait until higher temperatures before applying the maximum pressure, and they claimed that this allowed volatile species to escape from the unconstrained powder bed during heating. In the present study, a similar phenomenon may be occurring, where a higher P_i results in a higher green-body density (Table 2.2), resulting in less open-porosity for volatiles species to

escape. As a result, impurities are entrapped during fast sintering at high P_i, and thus more light lost due to absorption. Therefore, a lower P_i is preferred, with 0 MPa being optimal.

2.4.3   Effect of Maximum Pressure

When hot-pressing ceramics, higher maximum pressure (P_{max}) generally results in higher densities and improved optical properties.[34,39] However, the slope-change of the ram displacement data in Figure 2.6 and Figure 2.8 implies that there may be an optimum at lower pressures. To investigate this, samples hot-pressed at P_{max} of 2.5 to 80 MPa were studied, and the shrinkage rate versus time for these samples are shown in Figure 2.11. The shrinkage rate was calculated by taking the derivative of the displacement data. For each sample, the shrinkage rate is initially high (>1mm/min), and abruptly decreases when the respective P_{max} is achieved. The 2.5 and 5 MPa samples continue to shrink at a significant rate for approximately 10 minutes after reaching their respective P_{max}. This could be due to particle rearrangement, as well as a considerable amount of porosity remaining in the powder bed after these low pressures are applied.[55] On the other hand, the shrinkage rate of samples hot-pressed at $P_{max} \geq 10MPa$ abruptly decreases to virtually 0 mm/min after reaching their P_{max}. This is likely due to minimal porosity remaining at this higher pressure.
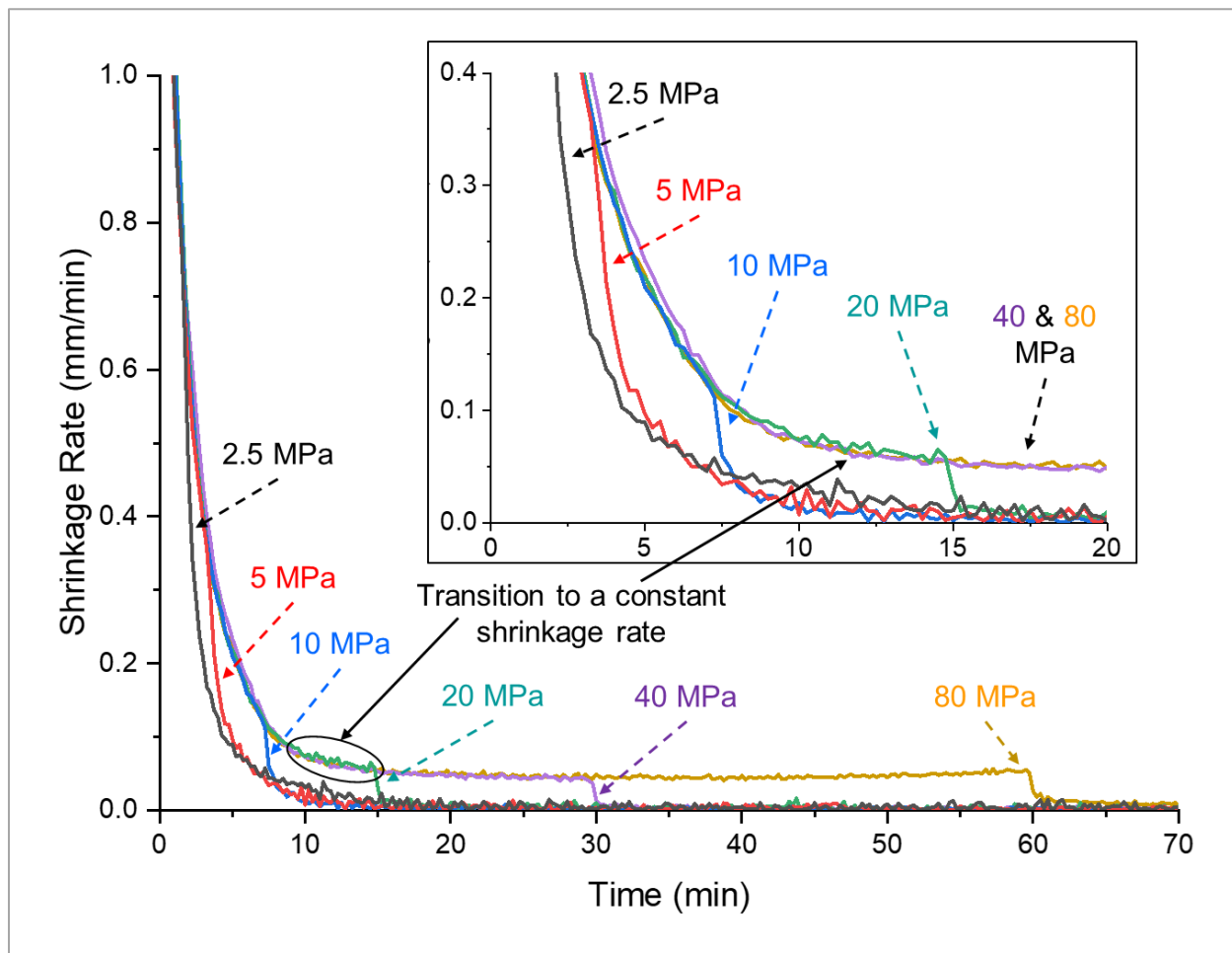
Figure 2.11. Shrinkage rate as a function of time for samples hot-pressed at different maximum pressures. The sudden decrease in each curve indicates when the maximum pressure was achieved.

Another important feature of Figure 2.11 is the transition to a constant shrinkage rate of approximately 0.05 mm/min, which begins after approximately 10 minutes. This is more clearly seen in the inset plot. It is important to note that the pressure for all samples in the current study was applied at a constant rate of 1.3 MPa/min, so this transition must be indicative of some phenomenon occurring during the slow application of maximum pressure. This transition corresponds to a pressure of approximately 15 MPa, so it occurs for samples with P_{max} of 20, 40, and 80 MPa. These samples go through this transition and maintain the constant shrinkage rate until their respective P_{max} is achieved, at which point the shrinkage rate promptly decreases to virtually 0 mm/min. It is thought that at pressures beyond 15 MPa, the powder bed has nearly completely densified, remaining porosity is closed-porosity, and any further pressure results in

40

linear-elastic strain of the powder compact and graphite die assembly. Hot-pressing at pressures beyond this transition results in a decrease in density, as shown in Table 2.2. Such results are contradictory to the commonly observed trend that higher pressures result in higher densities[34,39] (due to an increased driving force for sintering[55]). Therefore, hot-pressing at a pressure that corresponds to the transition to a constant shrinkage rate appears to be optimal for this powder under these conditions. Heuer et al.[12–14,48] used pressures between 27.5 and 46.8 MPa to achieve transparent alumina parts, but no discussion is given regarding the optimal pressure. They do, however, suggest that the hot-pressed parts must undergo a "critical strain" for recrystallization to occur.[13,14] Their initial experiments determined that a "critical strain" of more than 3.8% is necessary to induce primary recrystallization.[13] It is possible that the transition to a constant shrinkage rate of the current samples correspond to this "critical strain", though a more detailed analysis would be required to confirm this.

Table 2.2 shows the relative densities of samples hot-pressed at different maximum pressures. Relative density is low at lower maximum pressures (99.09% at P_{max} = 2.5MPa), then increases with increasing maximum pressure (99.93% at P_{max} = 10MPa). At maximum pressures beyond 10 MPa, the relative densities decrease with increasing maximum pressure (99.79% at P_{max} = 80MPa), though differences in density at these pressures may not be statistically significant. Lower pressures yielding lower densities is well understood: a lower pressure will result in less driving force for densification.[42] Higher pressures resulting in lower densities is not well understood. A possible explanation for this could be a pore swelling phenomenon that occurs after the maximum pressure is removed. This can be shown by considering the internal pore pressure (P_p) during hot-pressing:

$$P_p = P_{max} + \frac{2\gamma}{r_p} \qquad 12$$

Where P_{max} is the externally applied maximum pressure, γ is the surface energy of the pore-matrix interface, and r_p is the pore radius. Equation 12 shows that an increase in P_{max} will result in an increase in P_p. Additionally, r_p will decrease as the sample densifies, further increasing P_p, though the effect of decreasing pore size is minimal when compared to the externally applied maximum pressure. For example, at an externally applied pressure of 80MPa, and if it is assumed that γ =

41

$1J/m^2$ and $r_p = 0.5\mu m$, the internal pore pressure will be 84MPa. This means that the pore pressure will be effectively equal to the maximum pressure. As described in Section 2.3.2, the maximum pressure is released at the end of the isothermal hold, prior to cooling. It is thought that when P_{max} is released prior to cooling, P_p is still very high, and the surrounding matrix (which is still at temperatures >1700°C for several minutes) will creep to relieve the high pore pressure. The pores will swell, resulting in a lower density, and diminished optical properties. A schematic of this phenomenon is shown in Figure 2.12. This effect will be exacerbated at higher P_{max} due to P_p scaling with P_{max}. Furthermore, the transition to a constant shrinkage rate (Figure 2.11) may correspond to the P_{max} at which the P_p is too high, resulting in pore swelling when the pressure is released.
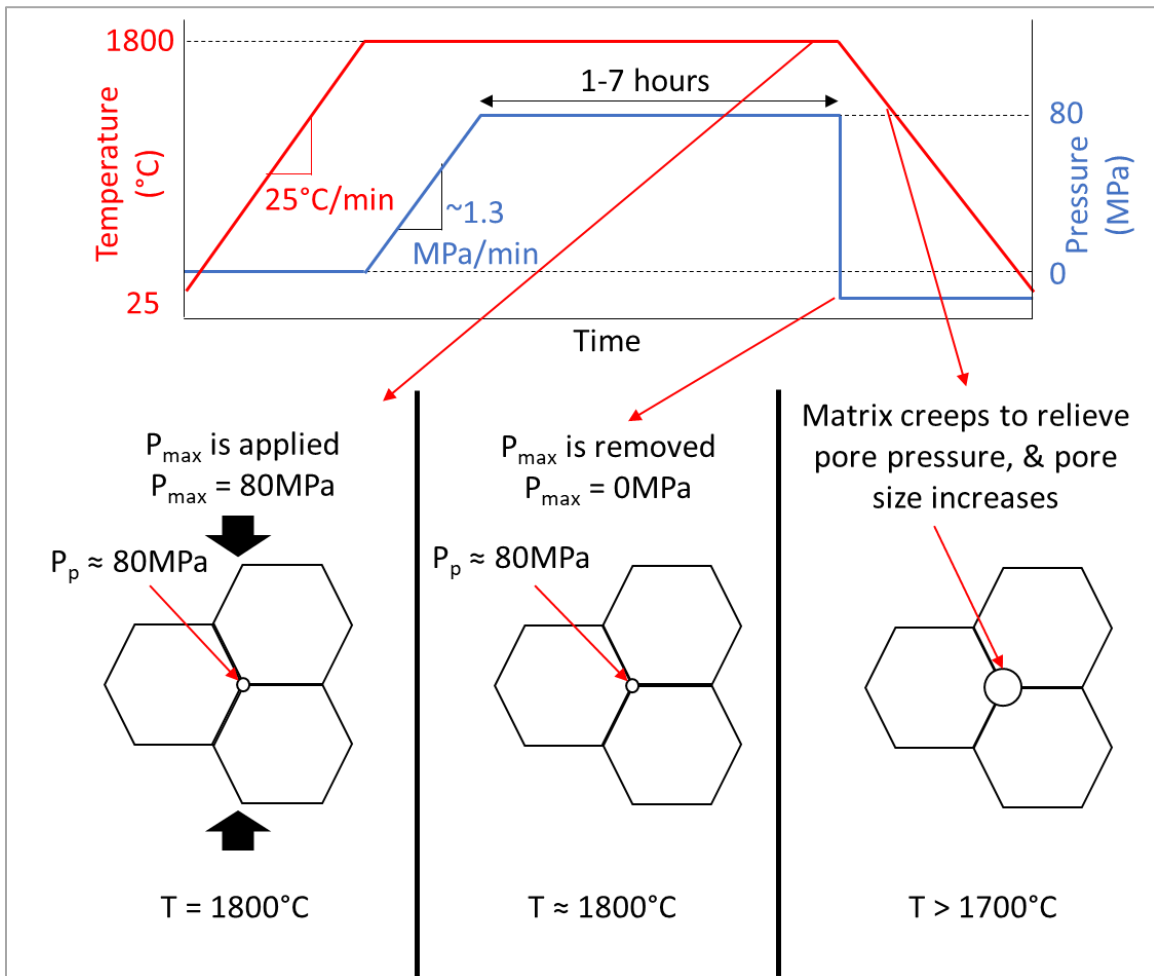
Figure 2.12. Schematic illustrating the proposed pore-swelling phenomenon.

Figure 2.13 shows the microstructure of samples hot-pressed at a P_{max} of 10MPa and 80MPa. The 10MPa sample has nearly no porosity, except for a single small intragranular pore. This lack of porosity corresponds to its very high in-line transmission. The 80MPa sample, however, has noticeable porosity at the triple-junctions and along the grain boundaries, which could be evidence of the proposed pore-swelling phenomenon. Figure 2.14 shows a lower magnification micrograph of the same 80MPa sample in Figure 2.13, showing how the intergranular porosity preferentially occurs along grain-boundaries that are horizontal with respect to the hot-pressing direction. Hot-pressing is uniaxial, so it follows that pore-swelling would occur along these horizontal grain boundaries when the uniaxial pressure of hot-pressing is released. This evidence further suggests that the proposed pore-swelling phenomenon is occurring.
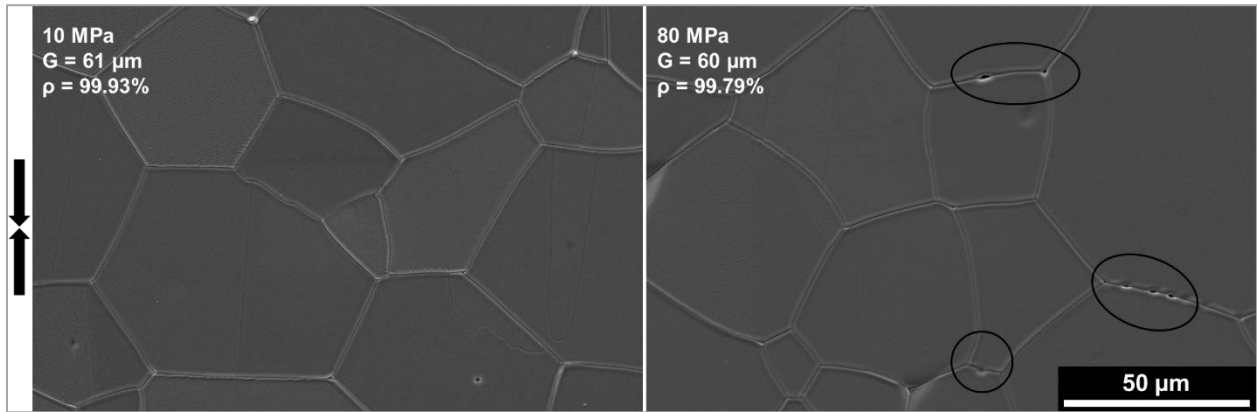
Figure 2.13. SEM micrographs of samples hot-pressed at P_{max} = 10 and 80 MPa. The arrows indicate the hot-pressing direction.
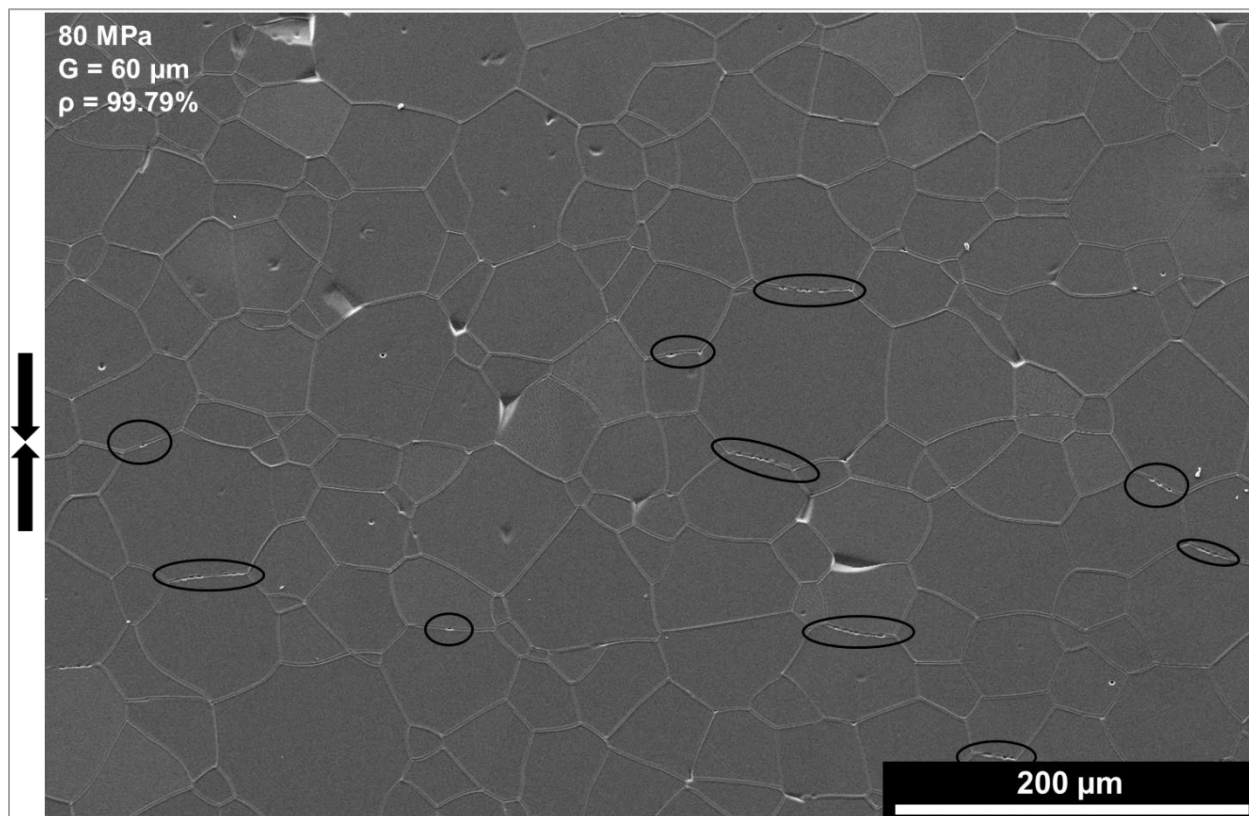
Figure 2.14. SEM micrograph of a sample hot-pressed at P_{max} = 80 MPa. The arrows indicate the hot-pressing direction.

It may be possible to mitigate this pore swelling phenomenon by maintaining P_{max} during cooling since the surrounding matrix cannot creep at lower temperatures. Literature regarding SPS of alumina reports that the pressure is typically maintained during cooling. Kim et al.[30–32] spark plasma sintered alumina to transparency at 1150°C and 80MPa for 20 minutes, followed by maintaining the 80MPa of pressure during cooling to 1000°C. The authors note that this was done to relieve residual stresses.[30–32] However, maintaining the pressure until the system is cooled to 1000°C may have retained a smaller pore size since 1000°C may be low enough temperature to prevent the surrounding matrix to creep under the pore pressure and swell to a lower density. This processing technique is used and discussed in a later section.

The optical properties of samples hot-pressed at different P_{max} are shown in Figure 2.15. The total and in-line transmission both initially increase to a maximum at 10MPa, then decrease with increasing P_{max}. Forward scattering, backward scattering, and absorption follow a reverse trend, where they initially decrease to a minimum at 10MPa, then increase with increasing P_{max}. Forward

scattering is the dominating mechanism of loss at all P_{max}. A considerable amount of light is also being lost due to absorption, and it reaches a minimum at 10 MPa, but this change in absorption is minimal compared to the changes observed in the other hot-pressing parameters. Backward scattering is also affected by differences in maximum pressure. Backward scattering is approximately 4% at 2.5MPa, decreases to a minimum of 0.7% at 10 MPa, then increases with increasing P_{max} to 8.3% at 80 MPa. As mentioned earlier, backward scattering is due to residual porosity,[7] so it follows that both too low and too high of maximum pressure is resulting in some amount of porosity. The densities of these samples confirm this, as shown in Table 2.2, though the differences in densities for samples hot-pressed at $P_{max} > 10$MPa may not be statistically significant.
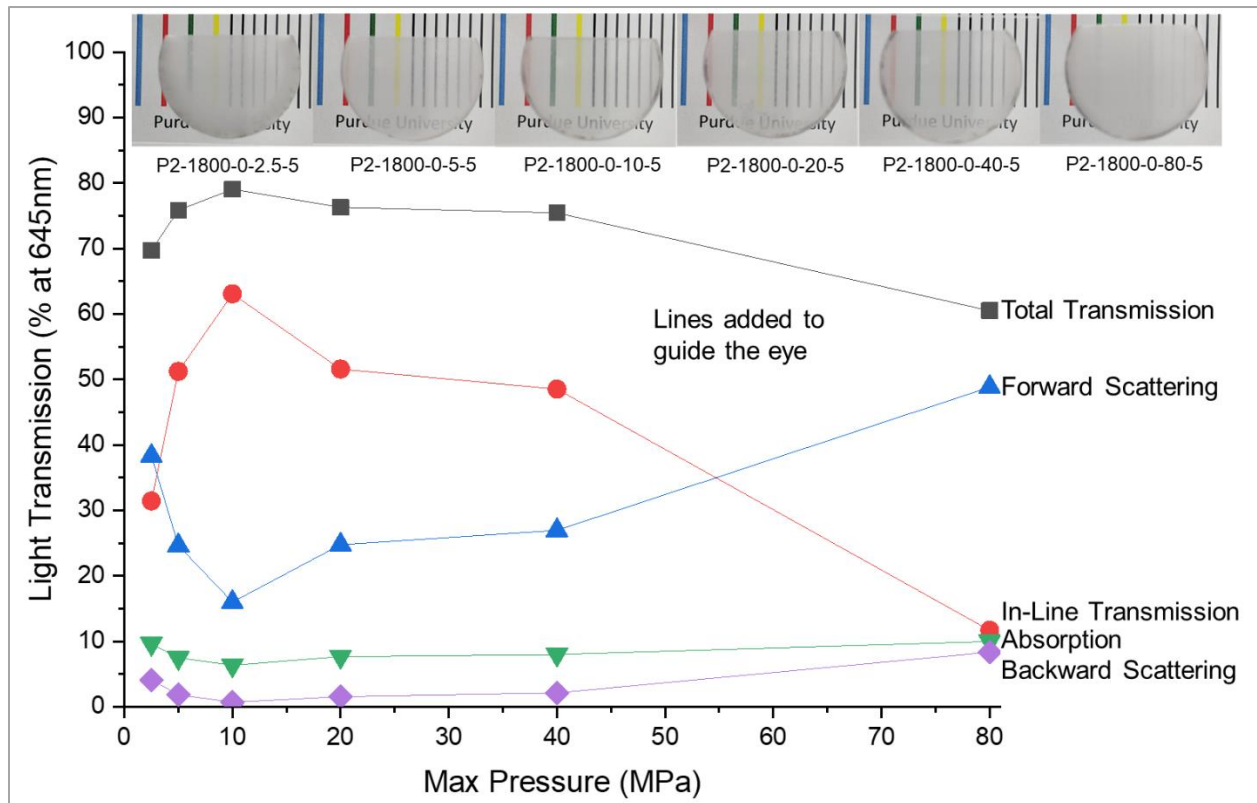
Figure 2.15. Light transmission as a function of maximum pressure, normalized to d = 0.8mm. Samples are placed 2cm above the colored lines, in order of increasing pressure.

It is notable that the best optical properties at 10 MPa corresponds with the transition to a constant shrinkage rate that was previously discussed. This further reinforces that the transition corresponds to a pressure that is high enough to ensure adequate pore removal yet is low enough to prevent the proposed pore swelling phenomenon. Adequate pore removal, as well as mitigated

pore swelling, decreases backward scattering and improves the in-line transmission. Therefore, it was determined that 10MPa is the optimal P_{max} for hot-pressing this platelet alumina to transparency.

2.4.4   Effect of Isothermal Hold Time

To ensure adequate density after P_{max} is applied during hot-pressing, an isothermal hold time (t_{iso}) is required.[44] However, it is important to determine the minimum amount of t_{iso} required to reach adequate densities, as a shorter time will result in smaller grain sizes.[55] Heuer et al. discussed how sinter-forged alumina samples must undergo a certain amount of t_{iso} after primary recrystallization to fully densify.[12–14,48] Their studies showed that at least 2 hours are required to achieve adequate densities for transparency. As shown in Table 2.2, the density of samples hot-pressed at different t_{iso} increases with increasing hold time, particularly between 3 and 5 hours, while the density increase from 1-3 hours and 5-7 hours may not be statistically significant. Figure 2.16 shows the microstructure of samples hot-pressed at t_{iso} ranging from 1 to 7 hours. After 1 hour, there is a noticeable amount of intragranular porosity (rectangles). After 3 hours, large white phases (circles) are seen at the triple junctions. This could be the result of remaining secondary phases (impurities) diffusing out along the grain boundaries during thermal etching. After 5 hours, only a few intergranular pores remain, and after 7 hours, the sample is virtually pore-free. This densification at higher t_{iso} occurs at the expense of increased grain growth, as shown in Table 2.2 and Figure 2.16.
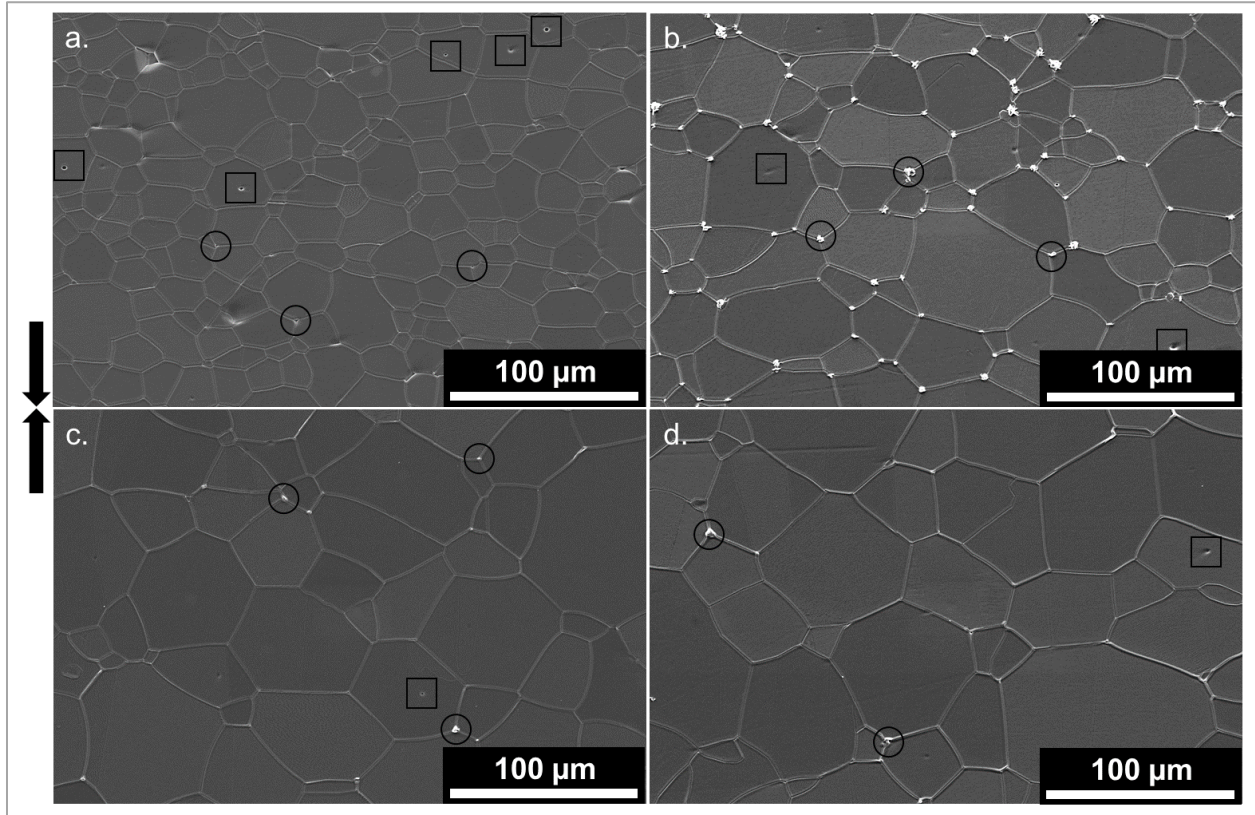
Figure 2.16. SEM micrographs of samples hot-pressed for 1 (a.), 3 (b.), 5 (c.), and 7 (d.) hours. Circles and squares indicate inter and intra-granular porosity, respectively. The arrows indicate the hot-pressing direction.

The optical properties of samples hot-pressed at different t_{iso} are shown in Figure 2.17. The total and in-line transmission both significantly increase with increasing t_{iso}. At least 5 hours are required to obtain best optical properties ($T_{ILT} > 60\%$). The in-line transmission increases from 1.6% at $t_{iso} = 1hr$ to 65.3% at $t_{iso} = 7hrs$. For all samples, forward scattering is the dominating mechanism of optical loss. Backward scattering is significant at shorter t_{iso}, but decreases with increasing t_{iso}, indicating that the samples have lower porosity at longer t_{iso}. This is confirmed by the increasing density of the samples with increasing t_{iso}, as shown in Table 2.2. Absorption is also steadily decreasing with increasing t_{iso}. This is not well understood, though it is possible that residual impurities in the sample are driven off during longer t_{iso}. From this data it was concluded that increasing t_{iso} increases the final transparency.
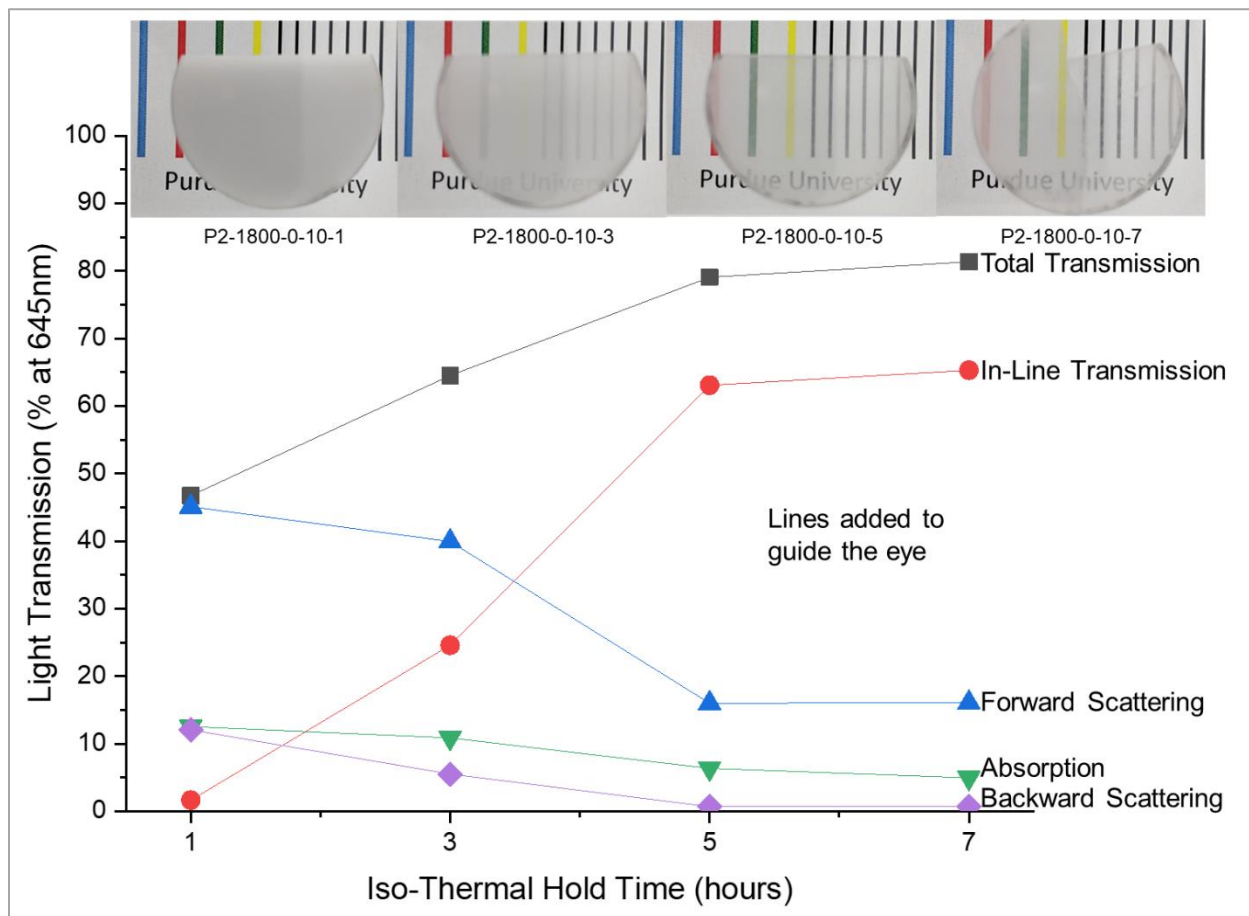
Figure 2.17. Light transmission as a function of isothermal hold time, normalized to d = 0.8mm. Samples are placed 2cm above the colored lines, in order of increasing time.

2.4.5 Comparison to Transparent Alumina using Equiaxed Morphology Powders

Figure 2.18 shows the in-line transmission as a function of wavelength for the best platelet-alumina sample produced in this study (P2-1800-0-10-7), a polished single-crystal sapphire standard, a commercially available transparent polycrystalline alumina sample (CeraNova's CeraLumina™), and a sample produced using equiaxed powder (E3-1825-0-40-5). The discontinuity between the visible and near-IR spectrums are due to the different detectors used. While the in-line transmission of the best platelet-alumina sample does not reach the theoretical maximum of sapphire, it is markedly higher than the equiaxed-alumina, and is much higher than the commercially available sample in the visible spectrum. However, the in-line transmission of the commercially available sample surpasses the transmission of the best platelet-alumina sample

in the near-IR wavelength range. The reason for this is not currently understood, though it could be that grain size dependency begins to take prevalence at these higher wavelengths.
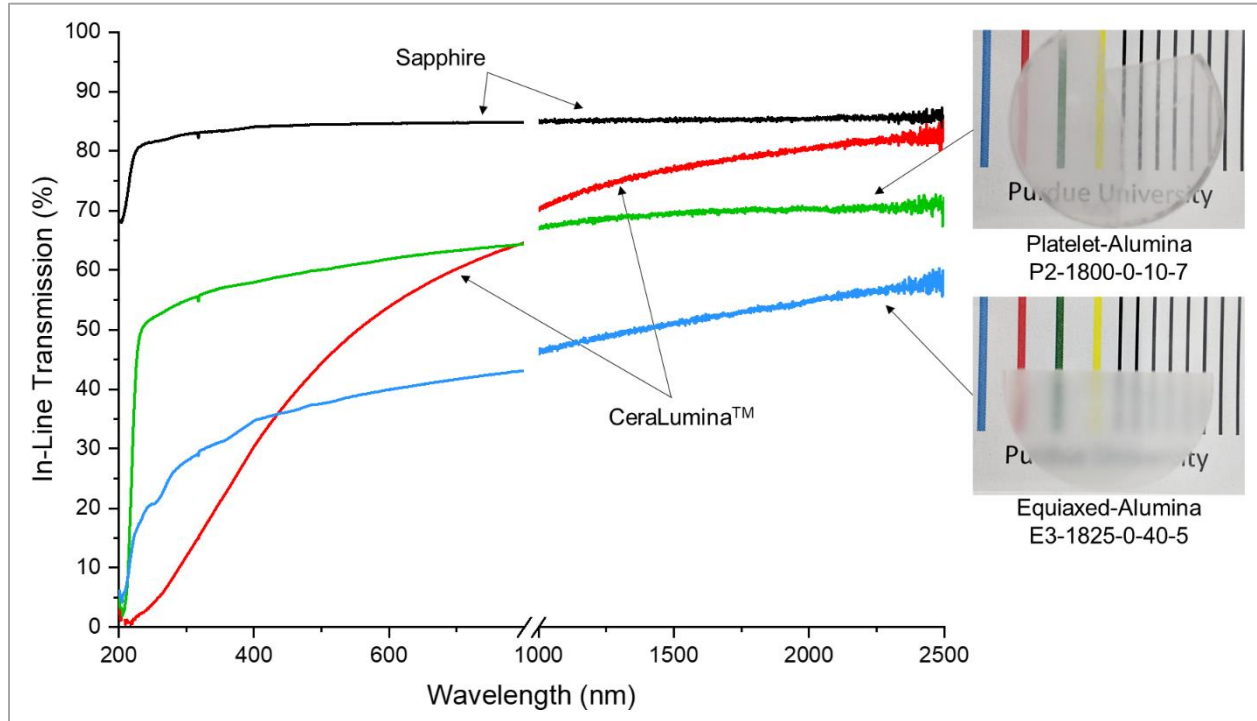
Figure 2.18. In-line transmission as a function of wavelength for a few comparative samples, normalized to d = 0.8mm. Samples are placed 2cm above the colored lines.

The best platelet-alumina sample in this study (P-1800-0-10-7) has an in-line transmission of 65.3% at 645nm. At the time of publication, and to the best knowledge of the authors, this is the 4th highest in-line transmission reported for transparent alumina.[5,7,9,11,15] It is noteworthy that this platelet-alumina sample was hot-pressed at lower pressures (10MPa) when compared to equiaxed-alumina samples from HIP or SPS at higher pressures (>200MPa).[7,9,11,33] This is particularly remarkable when the low intrinsic driving force for sintering of the large platelets (11µm in diameter) is considered.

Another noteworthy observation is that the in-line transmission of the platelet alumina sample is high despite its large grain size (>60µm, Table 2.2), as well as being relatively homogeneous across the entire optical spectrum (compared to the commercially available alumina sample) as shown in Figure 2.18. Both behaviors can be explained by the Rayleigh-Gans-Debye model,[7] which relates the in-line transmission of a birefringent polycrystalline ceramic to grain size (r_g), refractive index mismatch (Δn_g), sample thickness (d), and wavelength (λ_0), as shown in

Equation 1. This model shows that in-line transmission will increase with smaller grain sizes and lower refractive index mismatch, and will decrease at lower wavelengths.[7] However, refractive index mismatch has a much greater effect on the in-line transmission than grain size because it varies as Δn_g to the second power (compared to r_g to the first power). Additionally, as Δn_g gets sufficiently low, it begins to negate wavelength dependence entirely. Because the platelet alumina sample has such a large grain size, the high and relatively homogeneous in-line transmission must mean that the refractive index mismatch is low. A low refractive index mismatch is related to high crystallographic orientation,[5,7,15] which implies that the samples in the present study must have some degree of alignment.

XRD curves of a few representative samples are shown in Figure 2.19. It is apparent that the (006) and (0012) peaks, which are associated with the basal plane of sapphire, are very intense in the platelet alumina sample, while all peaks associated with the other crystallographic directions of alumina are nearly absent. Yi et. al.[15] observed similar trends in transparent alumina produced using a magnetic field to align equiaxed alumina prior to densification. They found that samples produced using a higher magnetic field resulted in higher in-line transmission, and XRD curves indicated that these samples had a high degree of crystallographic orientation. The crystallographic orientation in the present platelet alumina samples explains the high in-line transmission despite the large grain size. The crystallographic orientation minimizes birefringent scattering at the grain boundaries and reduces forward scattering losses. While the platelet alumina was not intentionally aligned prior to hot-pressing, it is reasonable to assume that a majority of the high aspect-ratio platelets will tend to lie flat when poured into the die and compacted by uniaxial pressure. Additionally, Heuer et al.[14] observed crystallographic orientation of their sinter-forged equiaxed alumina, so the present samples could be undergoing similar crystallographic orientation as a result of the hot-pressing parameters. The XRD curves of the equiaxed and CeraLumina[TM] samples are also shown in Figure 2.19, and the presence of peaks associated with all crystallographic directions indicates a lack of orientation, confirming that these samples have lower in-line transmissions due to birefringent scattering. Finally, while these 2θ XRD curves sufficiently indicate crystallographic orientation, they only provide a semi-quantitative analysis of the amount of orientation and does not include any information about the exact degree of mis-alignment of the grains.[56,57] A more effective analysis method, such as rocking curves or electron back-scatter detection (EBSD), will be used in future studies to study alignment of hot-pressed platelet alumina.
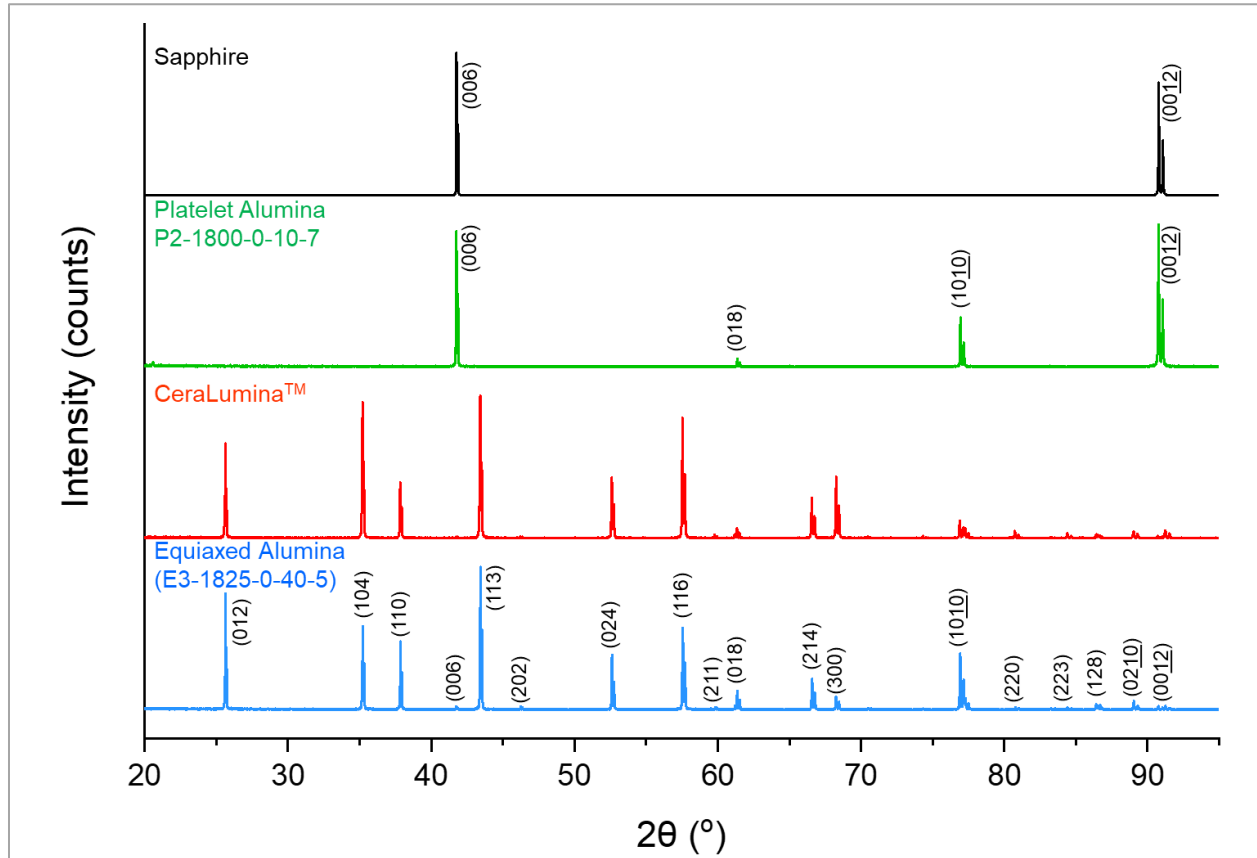
Figure 2.19. X-Ray Diffraction curves of a few representative samples, indicating differences in crystallographic orientation.

2.5 Summary and Conclusions

The effect of hot-pressing parameters on the densification and optical properties of platelet-morphology alumina was analyzed. Increasing the maximum temperature improves the optical properties, at the expense of increased grain growth. However, the samples have a distinct gray discoloration. Heat-treating the powder prior to hot-pressing and decreasing the pre-load pressure reduces the discoloration of hot-pressed samples, and hence reduces optical losses due to absorption. The heat-treatment likely removes impurities, and a lower pre-load pressure may allow residual volatiles to escape the powder bed during hot-pressing. A maximum pressure of 10 MPa yielded the highest in-line transmission. Pressures lower and higher than 10 MPa resulted in lower densities, which was confirmed by forward and backward scattering losses. Higher pressures resulting in lower densities is contrary to what is commonly observed in the literature and could be attributed to pore-swelling. It was found that >5 hours of isothermal hold time are required to

51

achieve sufficiently high densities as required for transparency; however, this led to an increase in grain growth. Optical losses at short isothermal hold times are mainly due to backward scattering, which is indicative of residual porosity. A sample fabricated by hot-pressing heat-treated platelet alumina powder with a pre-load of 0 MPa, a maximum temperature of 1800°C, a maximum pressure of 10MPa, and an isothermal hold time of 7hrs yielded an in-line transmission of 65.3% at 645nm, despite a large grain size of 65µm. The high and relatively homogeneous in-line transmission despite the large grain size is explained by decreased refractive index mismatch at the grain boundaries due to crystallographic orientation.

3. DENSITY GRADIENTS IN TRANSPARENT PRE-ALIGNED PLATELET ALUMINA PROCESSED VIA HOT-PRESSING

3.1 Contributions

The individuals listed below contributed the following tasks:

- Andrew Schlup: Powder preparation, hot-pressing, optical polishing and measurements, density measurements, scanning electron microscopy, and data analysis

- William Costakis: Development of pre-alignment methods and rocking curve measurements

3.2 Introduction

In this chapter, the densification behavior of pre-aligned platelet alumina is discussed. In a publication by Costakis et al,[58] a pre-aligned platelet alumina sample was hot-pressed using the optimal parameters determined in a previous publication by the present author,[25] and described in Section 2. While the sample displayed an increased in-line transmission ($T_{ILT, 645nm} = 70.0\%$) due to crystallographic orientation and reduced refractive index mismatch, a density gradient near the outer circumference of the sample was observed.[58] Such a gradient is not desirable, as the properties of a transparent window used for ballistic applications[1–3] must be homogenous across its entire surface.

The previous publication[25] (Section 2) identified maximum pressure as one of the key parameters for processing platelet alumina to transparency. Specifically, it was found that too low or too high of a maximum pressure would result in residual porosity. The density gradient observed by Costakis et al.[58] could be a result of using too low of a maximum pressure during hot-pressing pre-aligned platelet alumina. Therefore, this chapter will discuss the effect of maximum pressure on pre-aligned platelet alumina, investigating pressures ranging from 5 to 25 MPa, as well as how those samples compare to non-pre-aligned platelet alumina samples.

3.3   Experimental Methods

3.3.1   Powder Preparation

RonaFlair® White Sapphire (Merck KGaA, EMD Performance Materials) platelet alumina powder was used. It has a platelet morphology, with a diameter and thickness of approximately 11 and 0.5 µm, respectively, as shown in Figure 2.1. The platelet alumina powder was washed in high-purity de-ionized water by roller-milling overnight, followed by centrifuging and decanting the water. The powder was washed/centrifuged/decanted two more times, heated at 110°C overnight in air to evaporate remaining water, then sieved through a 250µm nylon mesh to break apart soft agglomerates. 6.0 grams of this powder was poured directly into the hot-press die to achieve non-pre-aligned (NPA) samples.

The warm-pressing procedure developed by Costakis et al.[58] was used to achieve pre-aligned (PA) samples. The raw platelet alumina powder (not water-washed) was compounded at 130°C in a thermoplastic polymer consisting of ethylene-ethyl-acrylate and plasticizers to form a 30 vol% solids loading blend. The blend was pressed into a 38 x 76 x 12.7mm brick, warm-pressed in a hydraulic press with heated platens (150°C) to a thickness of 0.5mm under a load of 4500kg, then slow-cooled to room temperature under the maintained load. Several 25.4mm-diameter discs were punched out of the pressed polymer/ceramic sheet, and these discs were stacked to form ~5mm tall stacks. These stacks were placed on an alumina crucible and heated to 500°C at 1.5°C/hr under flowing air to burn-off the fugitive polymer. Two of these stacks (approximately 6.0 grams of pre-aligned platelet alumina powder) were gently placed into the hot-press die to achieve each PA samples.

3.3.2   Hot-Pressing

The procedure described in Section 2.3.2 was used to hot-press the samples discussed in this chapter, with one minor exception: The maximum pressure (P_{max}) was maintained during cooling to 1000°C, released to a final pressure (P_f) of 1 MPa, then held for 10 minutes at 1000°C before cooling to room temperature. The only hot-pressing parameter that was varied during processing was the maximum pressure: P_{max} = 5 to 25 MPa. All other parameters remained constant and are illustrated in Figure 3.1.

NPA and PA samples were "quenched" in order to capture the microstructure at key points during the hot-press run. This was done by preparing additional samples in the same manner as a typical hot-press run and heating the hot-press up to temperature (1800°C), but the entire system was shut-down at two quench points; Quench #1: Immediately after reaching the maximum temperature of 1800°C but before any pressure is applied, and Quench #2: Immediately after a maximum pressure of 20 MPa was applied. For both key points, the furnace power was shut off, allowing un-controlled cooling to room temperature. For the second quench point, the maximum pressure was immediately removed at the moment of system shut-down. These two quench points are shown in Figure 3.1.
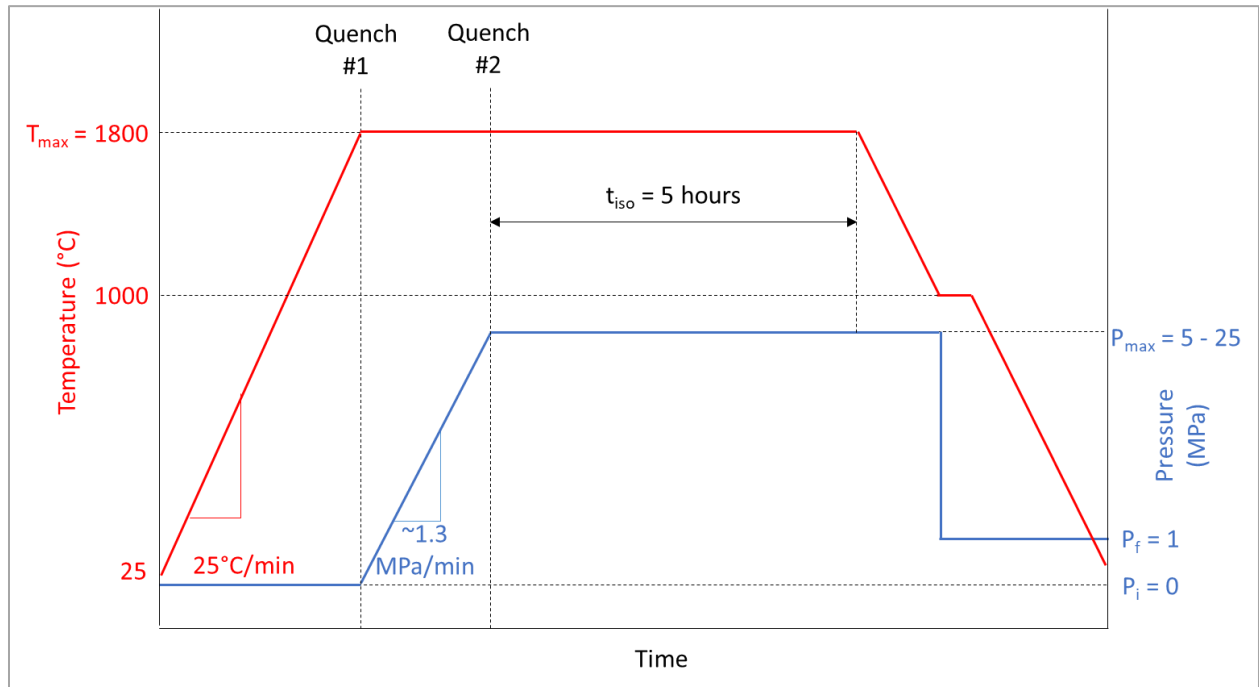
Figure 3.1. Schematic illustrating the hot-pressing parameters and quench points.

3.3.3 Optical Polishing and Measurements

The polishing procedure that is described in Section 2.3.3 was used to polish the samples discussed in this chapter. Additionally, the optical measurements that are described in Section 2.3.7 were used to measure the optical properties of the samples discussed in this chapter.

3.3.4   Density Measurements

The densities of the hot-pressed and 20MPa-quenched (Quench #2) samples were measured using the Archimedes method,[50] similar to what is discussed in Section 2.3.4. The geometric densities of the 0MPa-quenched (Quench #1) samples were measured by carefully machining the samples into a near-perfect cylindrical shape and measuring the dimensions and mass.

3.3.5   Characterization of Crystallographic Orientation via Rocking Curves

The crystallographic orientation of the hot-pressed samples were determined via rocking curve analysis on the (000$\underline{12}$) plane using a Panalytical Empyrean Diffractometer (Malvern Panalytical Ltd, Royston, UK). The exact methods and specifications are discussed elsewhere.[58] Briefly, an omega scan (rocking curve tilt) was performed on the Bragg's peak that corresponds to the (000$\underline{12}$) plane ($2\theta = 90.6°$). 3 separate rocking curves were performed on each side of each sample to obtain statistical data. An orientation parameter "r" was obtained from the curve fit of the March-Dollase equation.[58] A lower r corresponds to a higher degree of crystallographic orientation, and vice/versa.

3.3.6   Scanning Electron Microscopy

The cross sections of the hot-pressed and 20MPa-quenched (Quench #2) samples were prepared and characterized via SEM, similar to the methods described in Section 2.3.6. Energy dispersive spectroscopy (EDS) was used to identify impurities present in the cross sections after thermal etching. The 0MPa-quenched (Quench #1) samples were sectioned and dry "polished" by hand using progressively finer silicon-carbide paper, ending with 4000-grit. Residual powder was removed from the "polished" surface with compressed air, sputter-coated with Au-Pd, and the microstructures were observed using a Phenom SEM.

3.4   Results and Discussion

3.4.1   Crystallographic Texture

The orientation parameter "r" as a function of maximum pressure is shown in Figure 3.2. The first notable trend is that the pre-aligned (PA, open-shapes) samples have a lower r than the

non-pre-aligned (NPA, closed shapes) samples, indicating a higher degree of crystallographic orientation. Because the (00012) basal plane of alumina corresponds to the platelet morphology, it is evident that the alignment procedure is effective in preferentially aligning the platelets parallel to the direction of flow. For NPA samples hot-pressed for 5 hours (closed circles), there appears to be a slight decrease in r with increasing pressure, particularly between 10 to 25 MPa. This may be due to higher pressures resulting in more plastic deformation in the alumina sample. Heuer et al.[14] observed that a higher degree of plastic deformation results in more primary recrystallization, which in turn results in a higher degree of crystallographic alignment, so a similar phenomenon may be occurring here. For PA samples hot-pressed for 5 hours (open circles), there does not appear to be an effect on r with increasing maximum pressure. This is likely due to the alignment procedure having already aligned the platelets the maximum amount, and higher pressures do not result in additional crystallographic alignment.
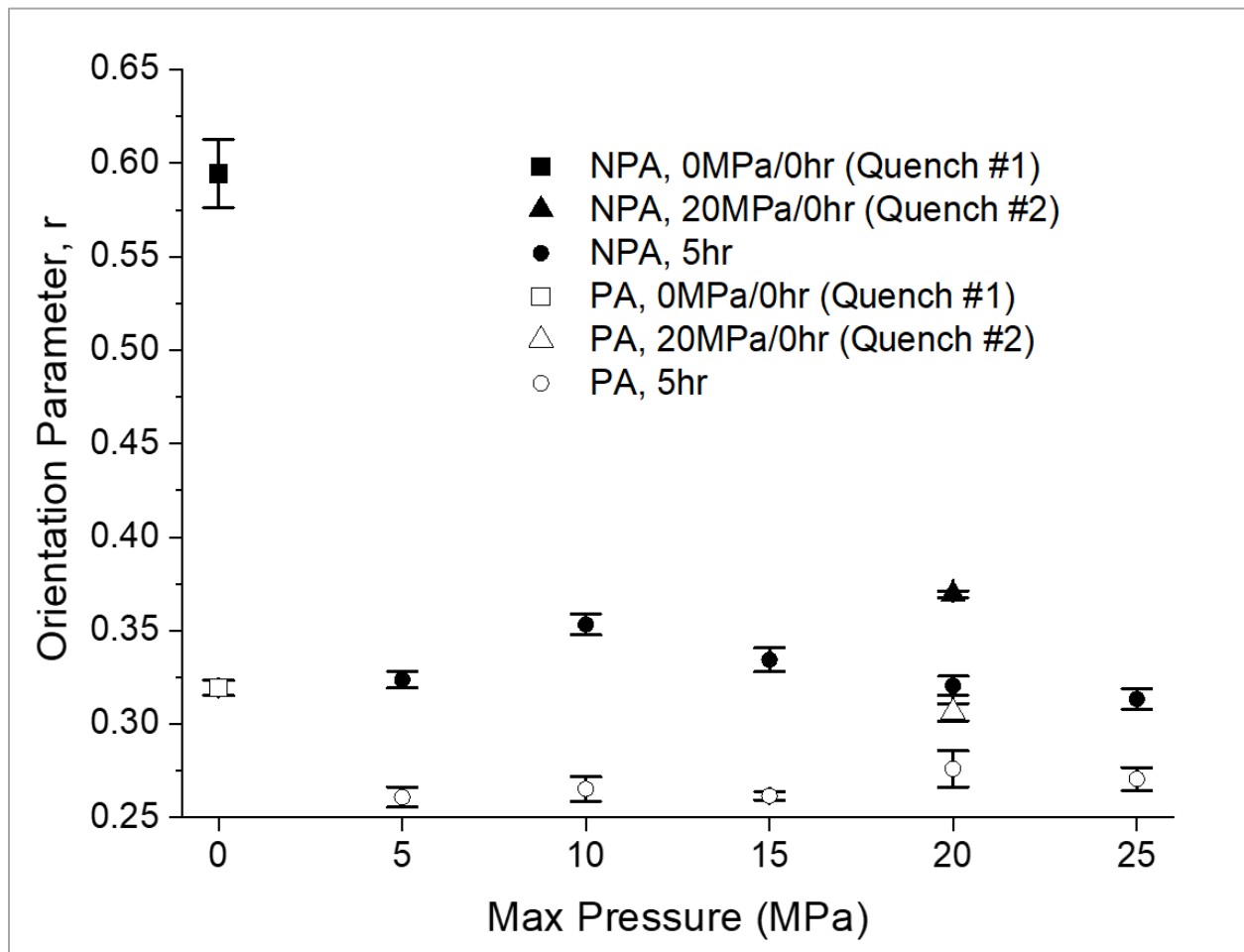
Figure 3.2. Orientation parameter "r" as a function of maximum pressure.

Figure 3.2 also shows the orientation parameter at the different quench points. The *r* of the NPA sample quenched before any pressure was applied (Quench #1, closed square) is very high, then it decreases significantly after a pressure of 20MPa is applied (Quench #2, closed triangle). This shows that simply pouring the platelet alumina powder directly into the hot-press die results in a very low degree of crystallographic alignment (high *r*), and the pressure-application step during hot-pressing run drastically increases the alignment (lower *r*). Furthermore, holding for an additional 5 hours (closed circle) results in a further decrease in *r*, meaning that even more crystallographic alignment is occurring during the isothermal hold at maximum temperature and pressure. A similar trend is observed for the PA samples (open square for Quench #1, and open triangle for Quench #2), though to a lesser degree. As previously mentioned, this is likely due to the alignment procedure aligning the platelets the maximum amount prior to hot-pressing.

3.4.2   Optical Properties

The optical properties of NPA and PA samples hot-pressed at different pressures are shown in Figure 3.3. There is no noticeable trend in the optical properties with an increase in pressure, nor is there a noticeable trend between NPA and PA samples. If anything, higher pressures (15-20MPa) result in samples with a minimally higher in-line transmission, and the PA samples may display a consistently higher in-line transmission, though these differences are likely not statistically significant. If the PA samples do, in fact, have a consistently higher in-line transmission, it would be due to their higher degree of crystallographic orientation, as discussed in Section 3.4.1.
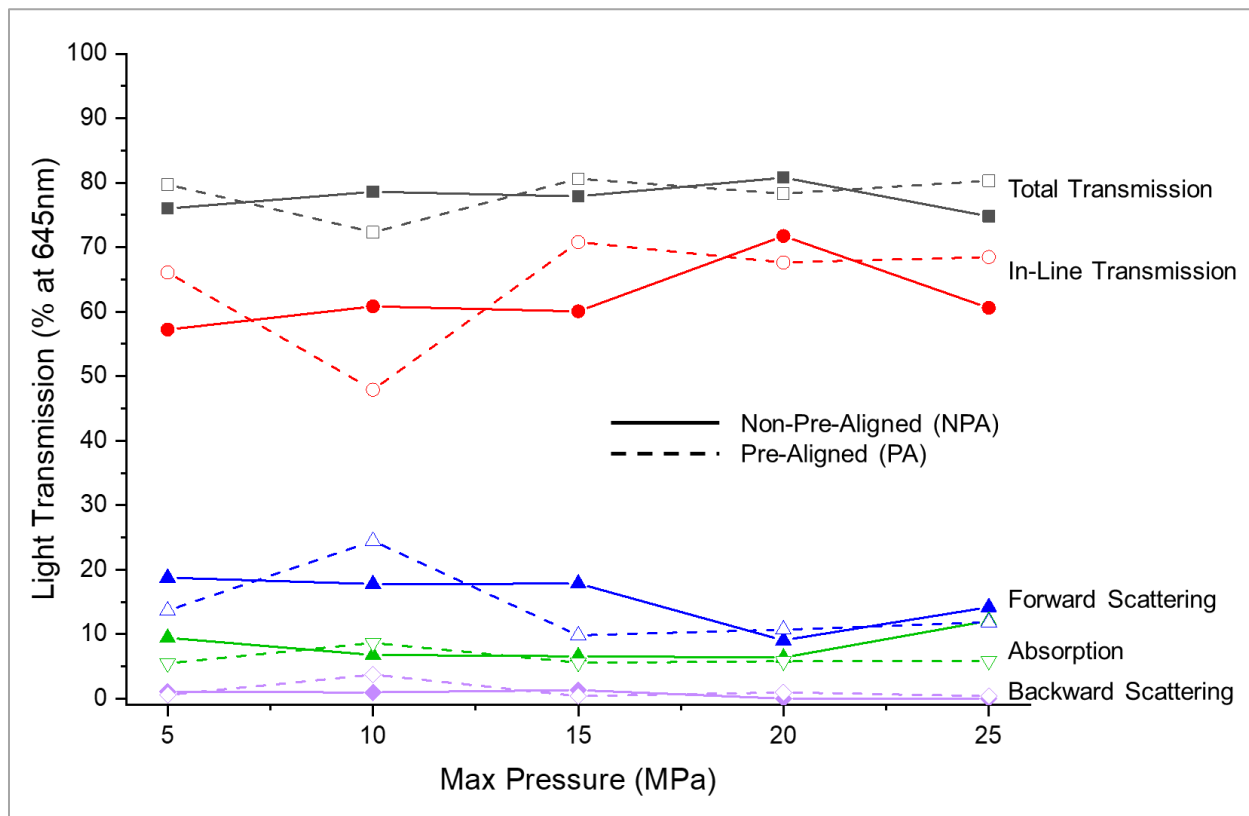
Figure 3.3. Light transmission as a function of maximum pressure for NPA and PA samples, normalized to d = 0.8mm.

The lack of a noticeable difference in pressure is contradictory to what has been observed in a previous publication,[25] (Section 2.4.3). This is likely due to the maximum pressure being maintained during cooling to 1000°C, as mentioned in Experimental Methods of this chapter, which was not the case in our previous publication.[25] As discussed in Section 2.4.3, removing the pressure prior to cooling may result in a pore swelling phenomenon, so maintaining the pressure until the system is cooled to 1000°C may be retaining a smaller pore size. This is because 1000°C may be a temperature that is low enough that the surrounding matrix is unable to creep under the pore pressure and swell to a lower density. Additionally, the in-line transmission is at least 60% for both types of powder at $P_{max} \geq 15MPa$, as shown in Figure 3.3. This was not the case in the previous publication[25] (Section 2.4.3), as the in-line transmission was less than 55% at $P_{max} \geq$ 20MPa, which further suggests that maintaining pressure during cooling is beneficial for improving transparency.

The NPA sample hot-pressed at P_{max} = 20MPa exhibited the highest in-line transmission of T_{ILT} = 71.7%. To the extent of the authors knowledge, this is the highest in-line transmission reported in the literature[5,7,9,11,15,25,58] at the time of writing this dissertation. The in-line transmission of the PA sample at the same P_{max} is T_{ILT} = 67.6%, which is only 4.1% lower. As shown in Figure 3.3, this is the least difference in T_{ILT} between the different sample types. It is possible that these differences are due to inherent variations in the processing methods. Regardless, P_{max} = 20MPa was chosen as the optimal pressure for future studies.

Figure 3.4 shows macro images of the hot-pressed samples. For all samples, an area of lower density can be seen in the form of a whitish color around the outer perimeters and is more prominent in the PA samples. This density gradient is similar to what was observed by Costakis et al.[58] Two different theories are presented to explain why this density gradient arises during hot-pressing NPA and PA platelet alumina samples: A difference in effective stresses during densification, and a difference in strain/recrystallization coupled with a temperature gradient during hot-pressing. These two theories are discussed in the following sections.
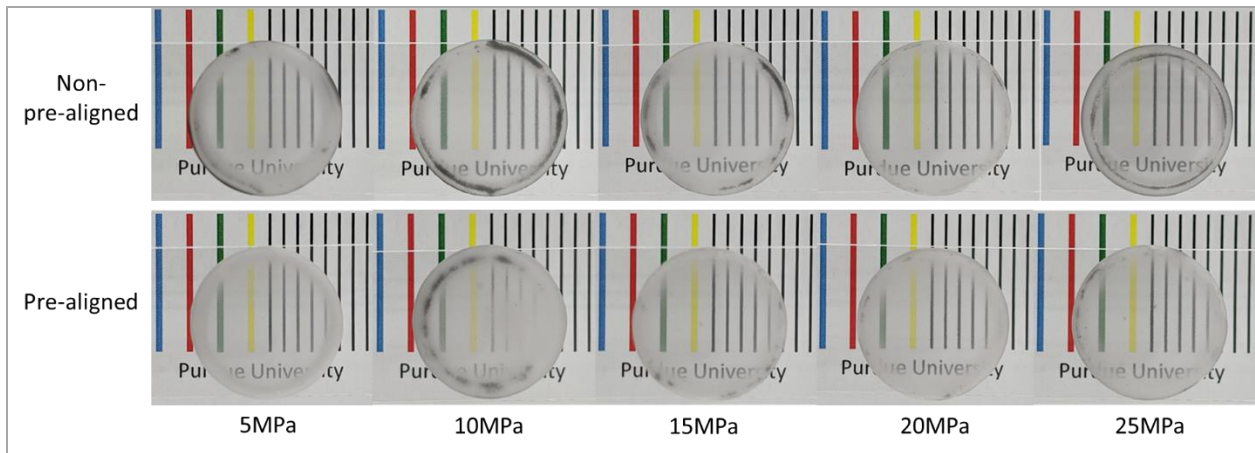
Figure 3.4. Macro images of NPA and PA sample hot-pressed at the different maximum pressures, illustrating transparency and the density gradients. Samples are placed 2cm above the colored lines.

3.4.3   Relative Density and Effective Stress Differences

A noticeable trend in Figure 3.3 is that the differences in forward scattering between the NPA and PA samples is minimal at P_{max} of 20 and 25MPa. Forward scattering losses are due to both porosity and crystallographic orientation (Section 1.2). The PA samples have a consistently lower r (higher degree of crystallographic orientation, Figure 3.2), but their forward scattering is

nearly the same as the NPA samples. This indicates that the PA samples at these higher pressures must have more porosity (lower relative density) than the NPA samples. This is confirmed in Figure 3.5, which displays the relative density of NPA and PA samples as a function of maximum pressure. The relative density slightly increases with maximum pressure for both powder types, which can be explained by a higher driving force for densification.[42] More importantly, the relative density of the NPA samples (closed circles) is higher than the PA samples (open circles) at all maximum pressures except for $P_{max} = 25MPa$. This result suggests that any optical improvements via a high degree of crystallographic orientation of the PA samples is negated by the presence of residual porosity, leading to the minimal difference in forward scattering. This is why high relative densities are so crucial for transparent ceramics.[4] Furthermore, this result suggests that the state of the platelet alumina powder prior to hot-pressing has a significant effect on the densification behavior.
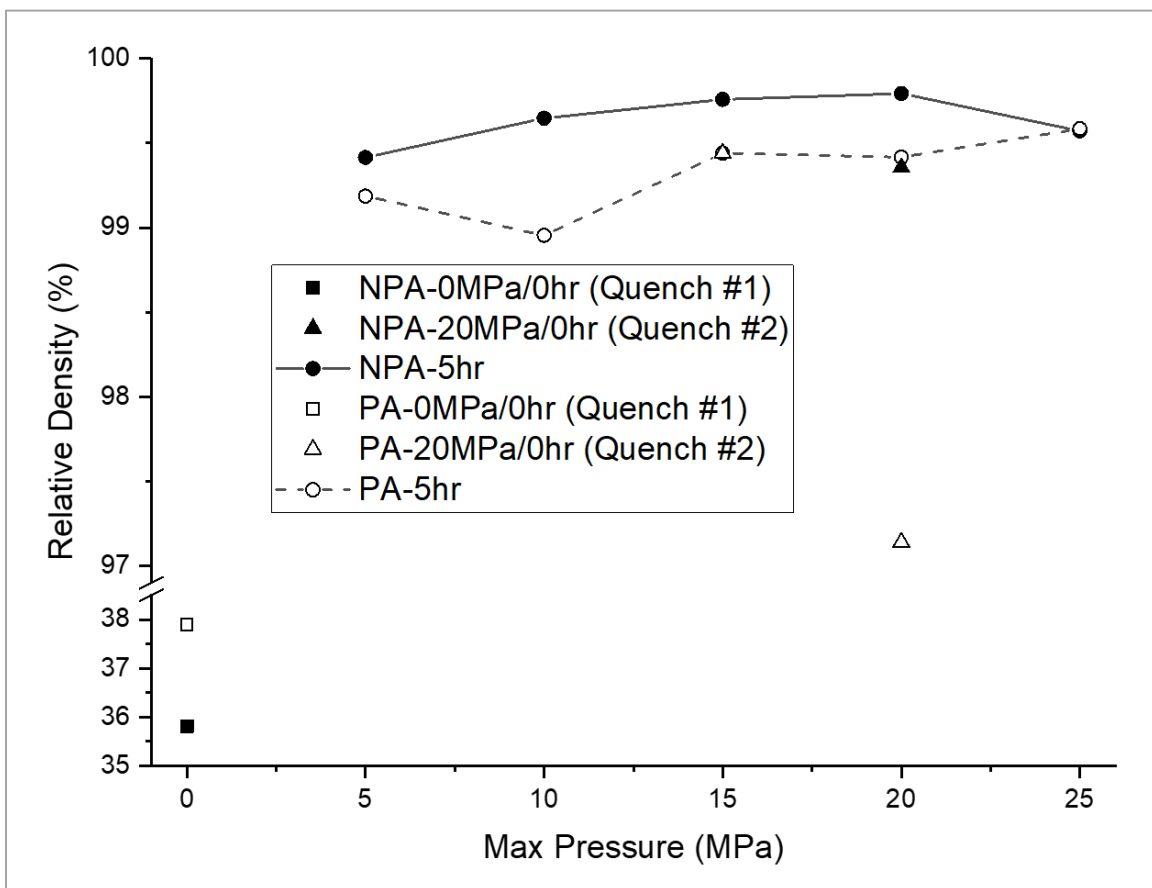
Figure 3.5. Relative density as a function of maximum pressure for the NPA and PA samples at key points during the hot-press run.

61

Figure 3.5 also shows the relative densities of NPA and PA samples quenched at 0MPa (Quench #1, closed and open squares) and 20MPa (Quench #2, closed and open triangles). The relative densities of the Quench #1 samples are less than 40%, which is significantly lower than the Quench #2 samples. This result is well understood: the platelets have a very large diameter (11µm), which yields very low driving forces for densification[25] (Section 2.2), and the application of pressure drastically increases the driving forces for densification,[25] resulting in the significant increase in density of the Quench #2 samples. However, notice that the relative density of the NPA-0MPa/0hr (Quench #1, closed square) is lower than the relative density of the PA-0MPa/0hr (Quench #1, open square). It is thought the NPA-0MPa/0hr sample (Quench #1) results in a lower relative density because the platelet powder is simply poured into the hot-press die, and the high aspect-ratio of the platelets prevents them from orienting in an efficient packing structure. Conversely, the high degree of crystallographic orientation of the PA-0MPa/0hr sample (Quench #1) results in a higher relative density because the high aspect-ratio platelets are forcibly arranged into a more efficient, brick-like packing structure due to the alignment procedure. Such a phenomenon is briefly discussed by Reed.[59]

Another important result in Figure 3.5 is that the relative densities of the NPA and PA Quench #1 samples flip after the maximum pressure of 20MPa is applied: the NPA-20MPa/0hr (Quench #2, closed triangle) sample is now at a higher relative density than the PA-20MPa/0hr (Quench #2, open triangle) sample. This may seem counter-intuitive, as a higher starting density will generally result in a higher final density. However, consider the influence of effective stresses during hot-pressing:[42] Lower relative densities result in an effective stress that is higher than the stress applied during hot-pressing (the maximum pressure, P_{max}). This is due to the localized stresses from the volume fraction of porosity and the pore morphology.[42] Effective stress, σ_e, is given by Equation 13:

$$\sigma_e = \frac{P_{max}}{D} \qquad\qquad 13$$

Where P_{max} is the maximum pressure applied during hot-pressing, and D is the fractional relative density of the sample during hot-pressing. The relative densities of the NPA and PA Quench #1 samples are 35.8% and 37.9%, respectively. With this, it can be calculated that the effective stress

of the NPA and PA samples during the initial stages of pressure application (P_{max} = 1MPa, for example) will be 2.79 and 2.64 MPa, respectively. The effective stress of the NPA sample is 5.5% higher than the effective stress of the PA sample, and it is thought that this higher effective stress results in the greater degree of densification that is observed in Figure 3.5.

To more clearly illustrate the changes in density at these different quench points, the relative density as a function of time for the PA and NPA samples are shown in Figure 3.6. This curve was created by mathematically relating the starting (Quench #1) and ending (Quench #2) relative densities to the recorded displacement during hot-pressing. This was done using a law of averages approach, as shown in Equation 14:

$$\rho_t = \rho_1(1 - \epsilon_t) + \rho_2 \varepsilon_t \qquad\qquad 14$$

Where ρ_t is the relative density at time t, ρ_1 is the relative density at Quench #1, and ρ_2 is the relative density at Quench #2. ε_t is the strain at time t, and is given by Equation 15:

$$\epsilon_t = \frac{d_f - d_t}{d_f} \qquad\qquad 15$$

Where d_t is the displacement at time t and d_f is the final displacement.

As previously shown, the NPA sample starts at a lower relative density than the PA sample. As pressure is applied, the relative density of the NPA sample surpasses the PA sample after approximately 5 minutes, and reaches 99.39% at the Quench #2 point, which is 2.25% higher than the PA sample. After an additional 5 hours, the NPA and PA samples further densify to 99.79% and 99.42%, respectively. As previously mentioned, the higher effective stress experienced in the NPA sample during the early stages of densification may allow it to reach a higher relative density after the P_{max} is applied. Then, the NPA sample only has to densify another 0.4% after 5 hours to reach its final density, while the PA sample has to densify another 2.28% to reach its final density, which is still not as high as the relative density of the NPA sample. This drastic difference suggests that a longer iso-thermal hold time is required to sufficiently densify the PA sample to a density that is similar to that of the NPA sample.
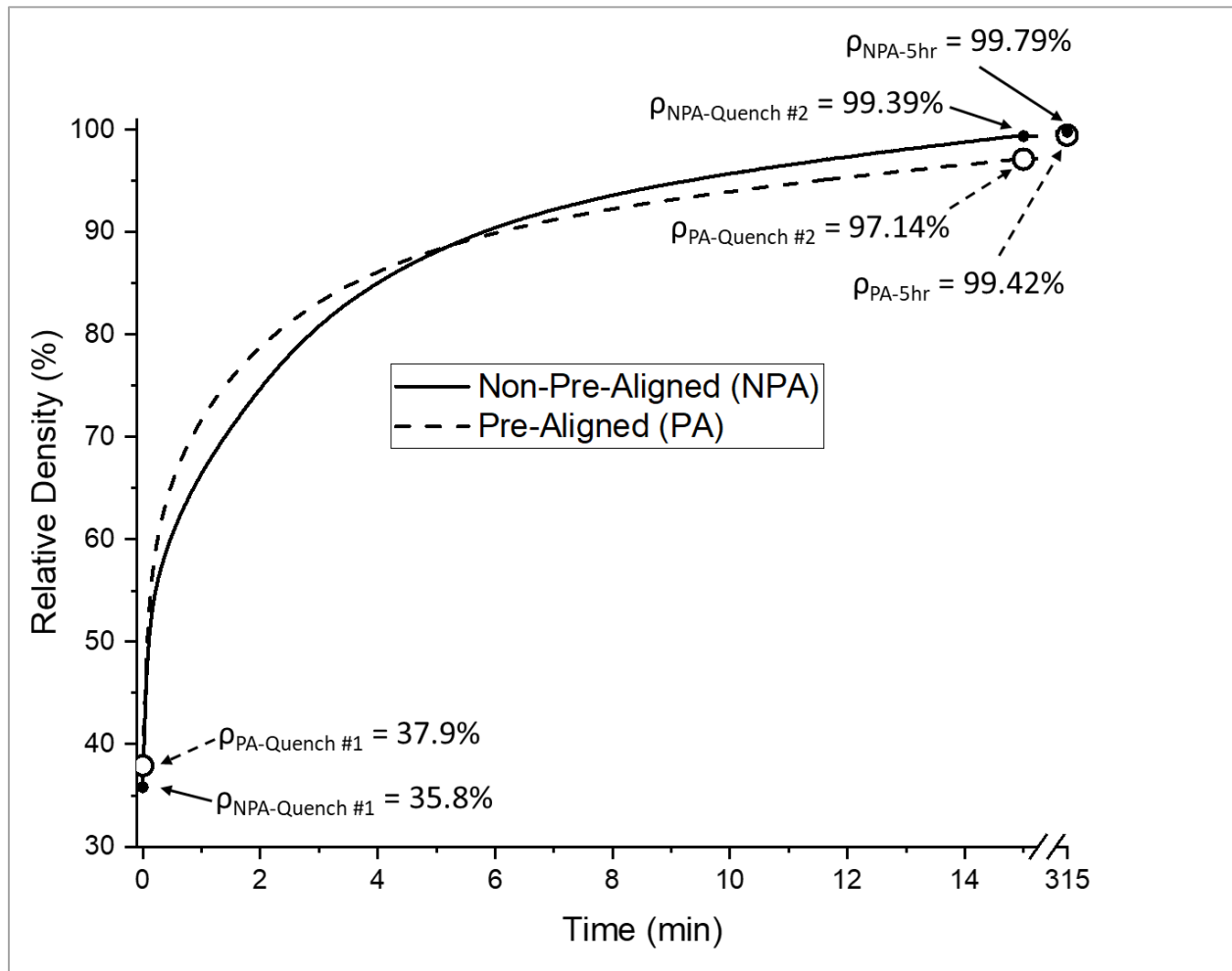
Figure 3.6. Relative density as a function of time for the NPA and PA samples at each of the key points during the hot-press run.

3.4.4 Microstructural Differences in the Center and Edges of Samples.

The microstructures of samples at the different quench points, as well as the fully dense samples, are shown in Figure 3.7 for the NPA samples and Figure 3.8 for the PA samples. For both powder types, the Quench #1 sample is very porous, as confirmed by the low relative density described in the previous section. Additionally, the diameter of the platelets is approximately 10μm, relatively unchanged from the original diameter of the raw platelets (Figure 2.1). However, the thickness of the platelets appears to have increased from ~0.1μm to ~2.0μm. The reason for this is unknown, though it is speculated that platelets that were initially in direct basal-plane contact with each other may have grown into each other, forming a single, thicker platelet. The most noticeable difference between the powder types at the Quench #1 point is the difference in

64

microstructural alignment. The NPA sample (Figure 3.7) appears to be mostly randomly oriented throughout, though there are regions of local alignment. This random orientation is confirmed by the high r in Figure 3.2. The PA sample (Figure 3.8), on the other hand, has a much greater degree of microstructural alignment throughout the entire sample. This high degree of alignment is similarly confirmed by the low r in Figure 3.2. This difference in alignment is expected due to the alignment procedure.
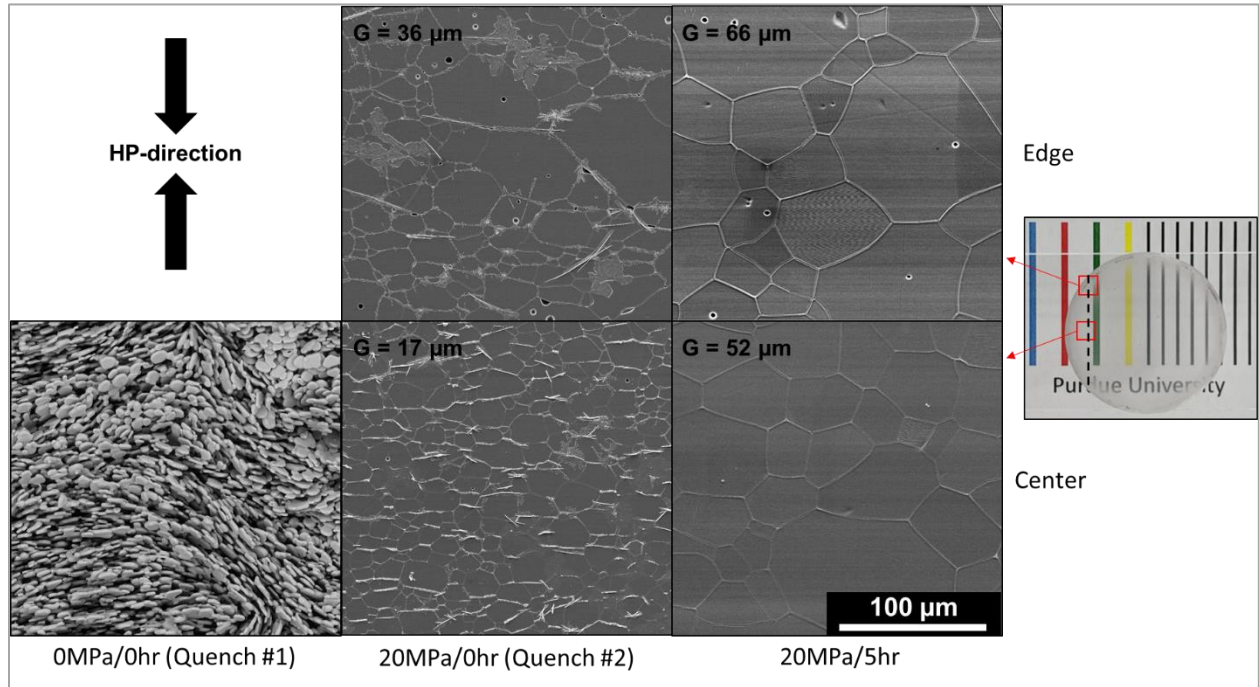
Figure 3.7. SEM micrographs of Non-Pre-Aligned (NPA) samples during various steps during the hot-press run. Macro image of sample is placed 2cm above the colored lines, and the dotted line indicates where the sample was sectioned.
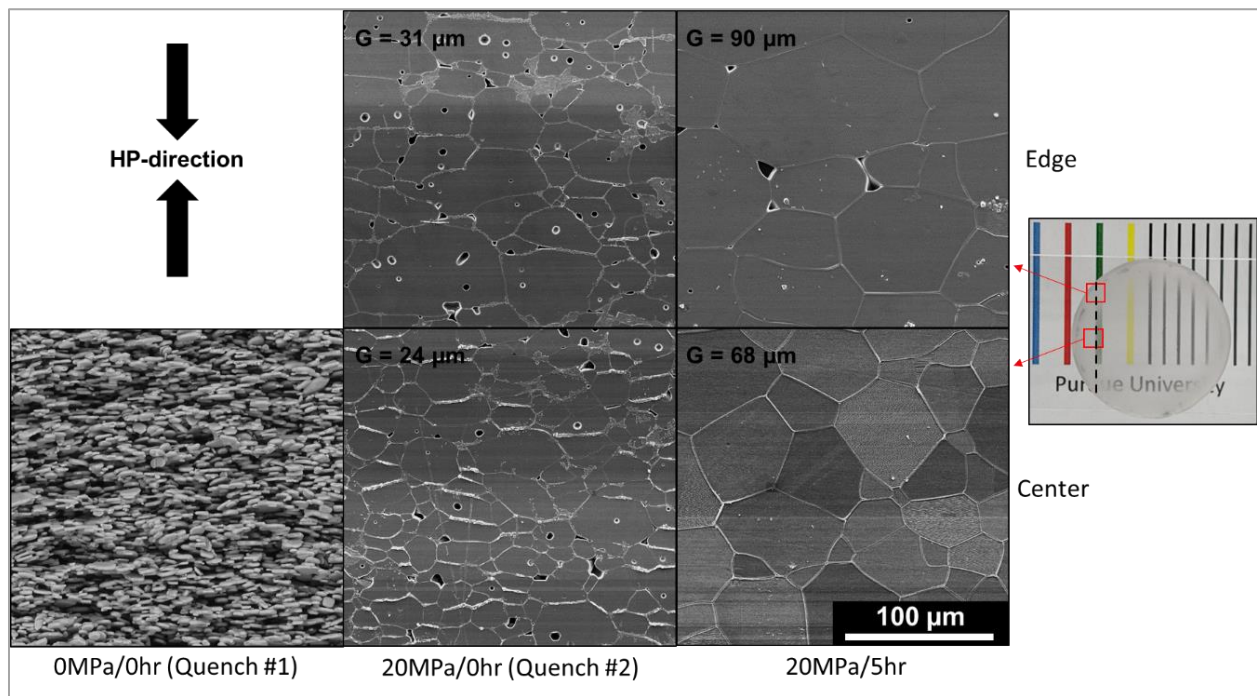
Figure 3.8. SEM micrographs of Pre-Aligned (PA) samples during various steps during the hot-press run. Macro image of sample is placed 2cm above the colored lines, and the dotted line indicates where the sample was sectioned.

A significantly different microstructure is observed at the Quench #2 point. For both powder types, the grain size increases and the microstructure still exhibits morphological texture, though at a much lower aspect ratio compared to the Quench #1 point. Additionally, there is a whitish phase at the grain boundaries. This whitish phase was confirmed to be calcium impurities by EDS, as shown in Figure 3.9. Impurity measurements (Section 2.3.1) indicated that approximately 0.012wt% of calcium impurities are present in the RonaFlair® platelet alumina powder. Though the supplier does not disclose the production method of the RonaFlair® platelets, it is known that a calcium oxide (CaO) and silicon oxide (SiO_2) glassy phase can promote anisotropic grain grown of alumina,[60] so it is possible that the supplier uses a similar composition to produce the high aspect-ratio platelets. If this is the case, this could be the source of the residual calcium impurities, except there is not enough of the calcium phase to continue to promote anisotropic grain growth during hot-pressing. Instead, the grain-growth begins to occur along the c-axis of the alumina platelets, resulting in a more equiaxed morphology.
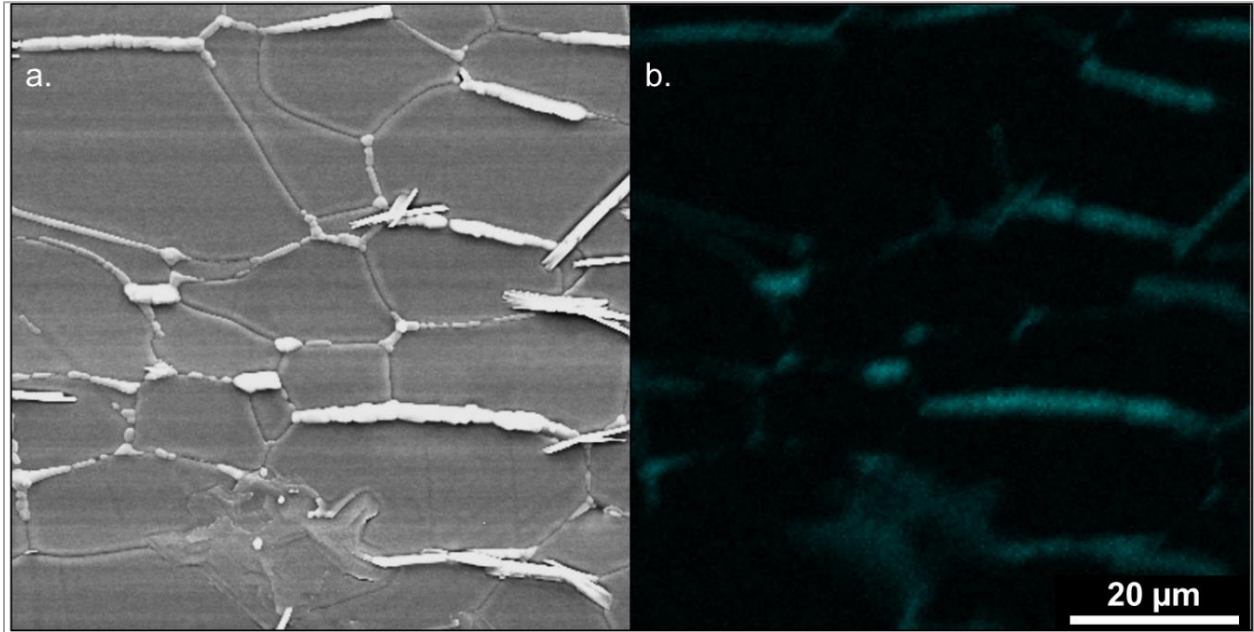
Figure 3.9. SEM micrograph of the NPA 20MPa-Quenched sample (a.) and corresponding EDS scan (b.) revealing calcium impurities at the grain boundaries.

A visible difference between the NPA and PA Quench #2 microstructures is the difference in porosity and grain growth. The center of the NPA Quench #2 sample (Figure 3.7) exhibits minimal grain growth compared to its previous state (Quench #1), as well as minimal porosity. The center of the PA Quench #2 sample (Figure 3.8), on the other hand, exhibits noticeable abnormal grain growth compared to its previous state (Quench #1), along with significant inter and intra-granular porosity. It is speculated that because the NPA sample is more randomly oriented (Figure 3.2) and at a lower density (Figure 3.5), than the PA samples, it is able to undergo more strain and subsequent primary recrystallization,[14] resulting in the smaller grain size and less porosity. Additionally, the abnormal grain growth of the PA sample will further contribute to the formation of intragranular porosity.[55]

Another possible explanation for the increased amount of porosity in the center of the PA Quench #2 sample is the location of pores due to the pre-aligned platelet particles. It is speculated that because the platelets are very highly aligned for the PA sample, the basal planes will come into intimate contact upon the application of pressure, and any residual porosity will be near the outer perimeter of the individual platelets. There is some evidence of this, as shown in Figure 3.8,

where the intragranular porosity appears to preferentially occur at vertical grain boundaries instead of horizontal grain boundaries.

The edges of the NPA and PA Quench #2 samples both exhibit significant abnormal grain growth and intragranular porosity compared to their centers, as shown in Figure 3.7 and Figure 3.8, respectively. However, the intragranular porosity is much less severe at the edge of the NPA sample compared to the edge of the PA sample. A similar increase in grain size and porosity towards the outer edges of the sample was observed by Heuer et. al.[14] They attributed this to a radially-changing strain-gradient from the center to the edge of the sample during forging, coupled with a temperature gradient between the center and edge of the sample, where the edges of the sample are at a higher temperature than the center due to the furnace system. The hot-pressing parameters in the current study are similar to those used by Heuer et. al,[14] suggesting that a similar mechanism could be occurring in the current samples. It is speculated that there is more recrystallization occurring at the edges of both samples because there is a higher degree of radial strain occurring at the edges of the sample during the application of pressure. This higher degree of recrystallization near the edges should result in increased densification. However, because there is a temperature gradient, the edges will be at a higher temperature and could be undergoing significant abnormal grain growth, resulting in the trapped inter-granular porosity despite the increased recrystallization. Furthermore, the starting density of the NPA sample is lower than the PA sample, which means that the NPA sample will undergo more strain and recrystallization than the PA sample across the entire sample. The greater amount of strain and subsequent recrystallization of the NPA sample could be sufficient to undergo better densification near the edges despite the temperature gradient. It is speculated that this is not the case for the PA sample, which did not undergo sufficient strain and recrystallization to overcome the abnormal grain growth caused by the temperature gradient. Further investigation is required to measure the severity of the temperature gradient and determine if it is enough to cause the observed increase in grain growth at the edge of the samples.

After hot-pressing at maximum temperature (1800°C) and pressure (20MPa) for an additional 5 hours, the centers of the NPA and PA samples (20MPA/5hr) undergo further change, as shown in Figure 3.7 and Figure 3.8, respectively. First, there is virtually no porosity and the grain size drastically increases, which is to be expected at this temperature for this amount of time.[61] Second, the grains appear to be even more equiaxed than their respective Quench #2

microstructures. Finally, the whitish phase (calcium impurities) is no longer present. The lack of the impurities in the 20MPa/5hr samples is likely due to the impurities diffusing out of the sample during the long isothermal hold time. This is similar to the trend observed in a previous publication[25] (Section 2.4.4), where longer isothermal hold times resulted in a reduction of the whitish phase in the microstructure, as well as a decrease in absorption losses.

After 5hrs, the edges of the NPA and PA samples also undergo significant change compared to the edges of their respective Quench #2 samples. A similar equiaxed morphology and decrease in impurities is observed in both samples. However, the grain size of the NPA sample does not increase as much as the PA sample does. Additionally, both samples have only a few small intragranular pores, but the PA sample has a few very large intragranular pores. It is thought that because the NPA sample underwent sufficient strain and primary recrystallization, the edge was able to fully densify within the 5hr isothermal hold time. Conversely, the PA sample underwent a lesser amount of strain and primary recrystallization, leading to increased abnormal grain growth and trapped porosity from the previously mentioned temperature gradient, so the edge was not able to fully densify within the 5hr isothermal hold time. Notice that the morphology of the intragranular pores are concave, which means that the pores are still able to shrink and further densify.[55] This suggests that a longer isothermal hold time would result in further densification. The PA sample produced by Costakis et al[58] was hot-pressed for 7 hours, instead of the 5 hours used in the current study, and resulted in an in-line transmission of $T_{ILT} = 70\%$. This is 2.4% higher than the best PA sample produced in the current study. This further suggests that a longer isothermal hold time is critical to fully densify a sample prepared via hot-pressing pre-aligned platelet alumina.

3.5   Summary and Conclusions

Transparent alumina samples were produced using non-pre-aligned (NPA) and pre-aligned (PA) platelet alumina powder and hot-pressing at 1800°C for 5 hours at maximum pressures ranging from 5 to 25 MPa. The PA samples exhibited higher crystallographic orientation at all stages of hot-pressing, confirming that the warm-pressing pre-alignment method is effective. In-line transmissions in excess of 70% are reported, though minimal changes in the optical properties were observed with changing maximum pressure. A significant density gradient from the center

to the edges was observed for both sample types, though it was much more substantial for the PA samples. Two mechanisms for this were suggested. First, the higher starting density of the PA sample may have resulted in a lower effective stress and a lesser degree of densification than the NPA sample. Second, the higher starting density of the PA sample resulted in a lesser amount of strain and primary recrystallization, which was insufficient to overcome abnormal grain growth in the edge of the sample due to a possible temperature gradient. Both of these mechanisms suggest that longer iso-thermal hold times are critical to hot-press pre-aligned platelet alumina to the densities required for transparency.

4. MECHANICAL PROPERTIES OF TRANSPARENT ALUMINA PRODUCED VIA HOT-PRESSING PRE-ALIGNED PLATELET ALUMINA

4.1 Contributions

The individuals listed below contributed the following tasks:

- Andrew Schlup: Powder preparation, hot-pressing, flexure specimen preparation, mechanical testing, scanning electron microscopy, and data analysis

- William Costakis: Development of pre-alignment methods, rocking curve measurements

- Erich Weaver: Assistance with mechanical testing

- Monica Viers: CAD of the rectangular graphite hot-press die

4.2 Introduction

In this chapter, the mechanical properties of transparent platelet alumina are discussed. When producing ceramics for ballistic applications, it is important to characterize their mechanical properties. High strength and hardness is desirable for these appliations,[8,9] and is greatly dependent upon the microstructure, including grain size, morphology, and crystallographic texture. In this study, three different alumina powder types were hot-pressed to transparency and their mechanical properties were characterized. The powder types include non-pre-aligned platelet-morphology alumina, pre-aligned platelet-morphology alumina, and equiaxed-morphology alumina. Mechanical testing included 4-point flexure and Vickers Hardness. The mechanical properties were then compared to their microstructures.

4.3 Experimental Methods

4.3.1 Powder Preparation

RonaFlair® White Sapphire (Merck KGaA, EMD Performance Materials) platelet alumina powder was used. The platelet alumina powder was washed in high-purity de-ionized water and sieved through a 250µm nylon mesh, as described in Section 3.3.1. 28.0 grams of this powder was poured directly into the hot-press die to achieve non-pre-aligned (NPA) billets. An alumina powder

with an equiaxed morphology (AA03, Sumitomo, 0.3-µm diameter, not washed in water) was also sieved through a 250µm nylon mesh, then 28.0 grams of this powder were poured into the hot-press die to achieve equiaxed (E) billets.

The warm-pressing procedure described in Section 3.3.1 was used to achieve pre-aligned (PA) samples. For this study, the pressed polymer/ceramic sheets were cut into several 30 x 46.5mm rectangular sheets, which were stacked to form ~10mm tall stacks. The fugitive polymer was removed using the previously described burnout procedure. Two of these stacks (approximately 28.0 grams of pre-aligned platelet alumina powder) were gently placed into the hot-press die to achieve PA billets.

4.3.2   Hot-Pressing

The NPA, PA, and E powder types were hot-pressed separately using a 30x46.5mm rectangular graphite hot-press die. The hot-pressing parameters are the same as those described in Section 3.3.2, except the maximum pressure was 20 MPa for all billets. Three or 4 billets were hot-pressed for each powder type in order to obtain a sufficient number of flexure bars.

4.3.3   Flexure Specimen Preparation

The standard procedures for surface grinding, as described in ASTM C1161-18,[62] were used to machine "b" bars for flexure testing. A customary polishing procedure was used during the machining process, as will be described below.

The hot-pressed billets were hand-ground using 60-grit SiC paper and water lubricant to remove residual graphoil and Mo-foil, as well as smooth the rough edges and faces. The billets were then mounted to a magnetic metal plate using a thermoplastic polymer (Crystalbond[TM], 509-3) for machining with resin-bonded diamond wheels and copious amounts of water lubricant. All grinding and cutting steps were performed parallel to the 45mm-length of the billets. A 150-grit wheel was used to machine equal amounts of material from each side of the billets. 320 and 600-grit wheels were then used to machine one of the faces of the billets.

The billets were then mounted to custom-made aluminum polishing mounts such that the previously 600-grit machined face could be polished on an auto-polisher using the following diamond suspensions: 15-µm (30 min.), 9-µm (1 hr.), and 6-µm (6 hrs.). This polished face of the

billets would eventually become the tensile surface of the flexure bars. The platelet-alumina billets (NPA and PA) suffer from severe grain-pullout during polishing, so very long polishing times were required to machine past the pull-out. As such, this customary polishing procedure was found to be the only logistical way to produce bars with an acceptable tensile surface finish, as hand-polishing each individual flexure bar would have been very time-consuming.

After the customary polishing procedure, the opposite face of the billets were machined to the final height dimension (d=4.0±0.13mm) using 320 and 600-grit wheels. A 100-grit cut-off wheel was used to cut four ~6.35mm wide bars from each billet. The bars were rotated such that each of the cut faces of the bars could be machined to the final width dimension (b=3.0±0.13mm) using 320 and 600-grit wheels. The d and b dimensions were both machined to be within parallelism tolerances (<0.015mm). The edges of the tensile faces were machined to a 45° and 0.12mm-deep chamfer using a 600-grit wheel. The edges of the compression face were not chamfered. Finally, the tensile face of each specimen was hand-polished with a 3-μm diamond suspension for 1 minute, with the wheel rotating parallel along the length of the specimen, then rotated 180° and polished for an additional minute. The densities of each bar were measured via Archimedes density, as described in Section 2.3.4.

4.3.4   Mechanical Testing: Flexure Stress and Vickers Hardness

The flexure stress of the specimens was measure in accordance to ASTM C1161-18,[62] using a semi-articulating 4-point fixture. A crosshead rate of 0.5 mm/min was used, and all specimens were tested in a laboratory with relative humidity of 28%RH and a temperature of 21.8°C. Of all specimens tested, only 9 of each powder type resulted in successful fractures (failing within the inner gauges), and 3 of the 9 PA specimens were removed due to density gradients (discussed in a later section).

The Vickers hardness of a few representative broken flexure bars was measured in accordance to ASTM C1327-15.[63] The ends of the broken flexure bars were mounted in a 2-part epoxy (PELCO 2-Hour Epoxy) such that the faces that were parallel ($HV_\parallel$, also the tensile face during flexure testing) and perpendicular ($HV_\perp$) to the hot-pressing direction could be polished for indentation. The polishing procedure described in Table 2.1 was used, resulting in a 1-micron diamond finish. Commercially available single-crystal sapphire samples were similarly mounted

and polished such that hardness could be determined on the c-plane and a-plane. 10 indentations were performed for each specimen, with an indentation load of 1kgf for 15 seconds, also in a laboratory with a relative humidity of 28%RH and a temperature of 21.8°C. The orientation of the parallel ($HV_{\parallel}$) and perpendicular ($HV_{\perp}$) indentation directions on a flexure bar are illustrated in Figure 4.1.
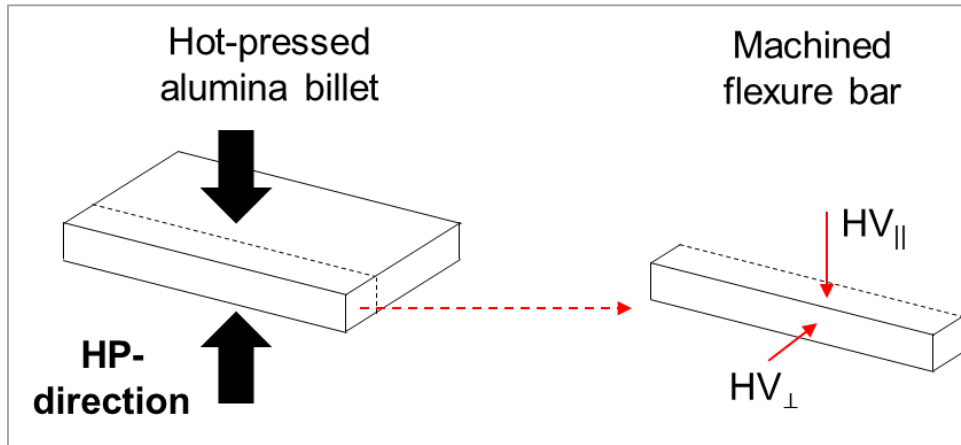
Figure 4.1. Schematic illustrating the hot-pressing direction of the billets, and the corresponding indentation directions on a flexure specimen.

4.3.5 Microstructural and Texture Characterization

The microstructure and fracture surfaces of a few representative broken flexure bars were characterized via SEM, similar to the methods described in Section 2.3.6. A working distance of 10mm was used for the bulk micrographs, while a working distance of 30mm was used for the fracture surfaces. The crystallographic texture of similarly hot-pressed 25.4mm diameter samples were measured via rocking curves, as described in Section 3.3.5.

4.4   Results and Discussion

4.4.1   Flexure Stress

The flexure stress of the different powder types of hot-pressed transparent alumina are shown in Table 4.1. The flexure stress is very low for all three powder types compared to what is reported for alumina in the literature.[64] This is due to the large grain size (>40µm) of the present samples, as shown in Table 4.1 and Figure 4.2. It is well known that both the Petch relationship[65] and the Griffith criterion[66] dictate that the flexure stress of a brittle material will decrease with increasing

74

grain size. Fracture will occur at the largest flaw, and in the absence of flaws, the largest flaw will correspond to the grain size of the material. The large grain size in the current samples is a result of the hot-pressing parameters; 1800°C for 5 hours is more than enough thermal energy to promote substantial grain growth. Heuer et al.[67] used similar hot-pressing parameters to produce transparent alumina with a similar grain size, resulting in flexure stresses in the 200MPa range. Other methods to process transparent alumina, such as isostatic hot-pressing (HIP), result in flexure stresses in the 600MPa[9] and 800MPa[68] range. This is because the lower temperatures (1200°C) and high pressures (200MPa) used during HIP'ing facilitate in high densification and low grain growth, producing samples with a submicron grain size, resulting in much higher flexure stresses.

Table 4.1. Mechanical and microstructural properties of hot-pressed transparent alumina.

Powder type	# of Specimens used	Flexure Stress (MPa)	Parallel Hardness $(HV_\parallel, GPa)$	Perpendicular Hardness $(HV_\perp, GPa)$	Relative Density (%)	Grain size (µm)	Orientation parameter, r
NPA	9	176 ± 7.50	14.8 ± 1.3	17.3 ± 1.3	99.69 ± 0.07	40.1 ± 4.5	[a]0.32
PA	6	176 ± 18.6	15.6 ± 0.8	17.8 ± 0.8	99.16 ± 0.20	62.8 ± 13.3	[a]0.27
E	9	174 ± 50.6	17.8 ± 0.6	17.6 ± 1.6	99.71 ± 0.08	63.7 ± 13.9	N/A
[b]Sapphire	N/A	N/A	15.6 ± 0.8	17.8 ± 0.5	100	N/A	0.0

Note:
NPA: Non-Pre-Aligned
PA: Pre-Aligned
E: Equiaxed
[a]Data gathered from 25.4mm diameter hot-pressed samples
[b]MTI Corporation
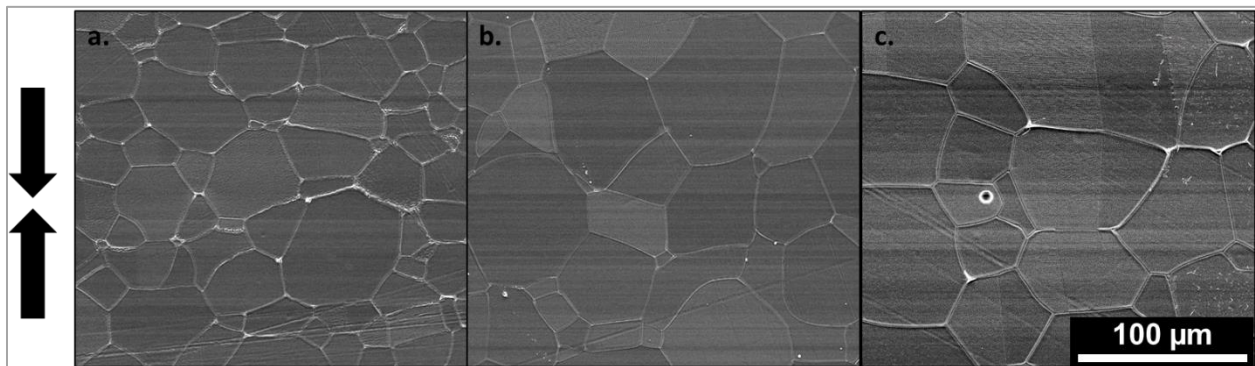
Figure 4.2. SEM micrographs of Non-Pre-Aligned (a.), Pre-Aligned (b.), and Equiaxed (c.) samples. The arrows indicate the hot-pressing direction.

There is a minimal difference in the flexure stress between the different powder types, as shown in Table 4.1, and any differences are likely not statistically significant. It was theorized that crack-deflection behavior would be observed in the PA samples due to anisotropic grain morphology.[69] That was not the case, as shown in Figure 4.3. This is because despite using a high aspect-ratio platelet morphology powder which yields a high degree of crystallographic orientation (low r, as shown in Table 4.1 and discussed in Section 3.4.1), the platelets undergo grain growth along the c-axis, resulting in an equiaxed grain morphology, as shown in Figure 4.2 and discussed in Section 3.4.4. Additionally, the samples underwent inter-granular fracture, as shown in the forward-view of the fracture surfaces in Figure 4.4.
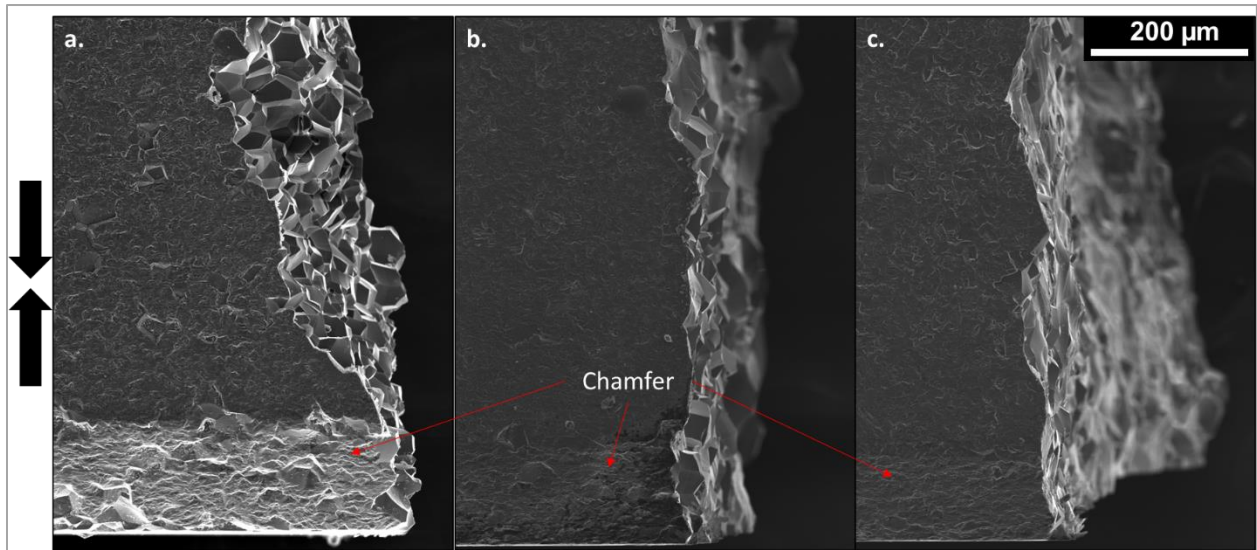
Figure 4.3. Side-view of the fracture surfaces for the Non-Pre-Aligned (a.), Pre-Aligned (b.), and Equiaxed (c.) samples. The arrows indicate the hot-pressing direction.
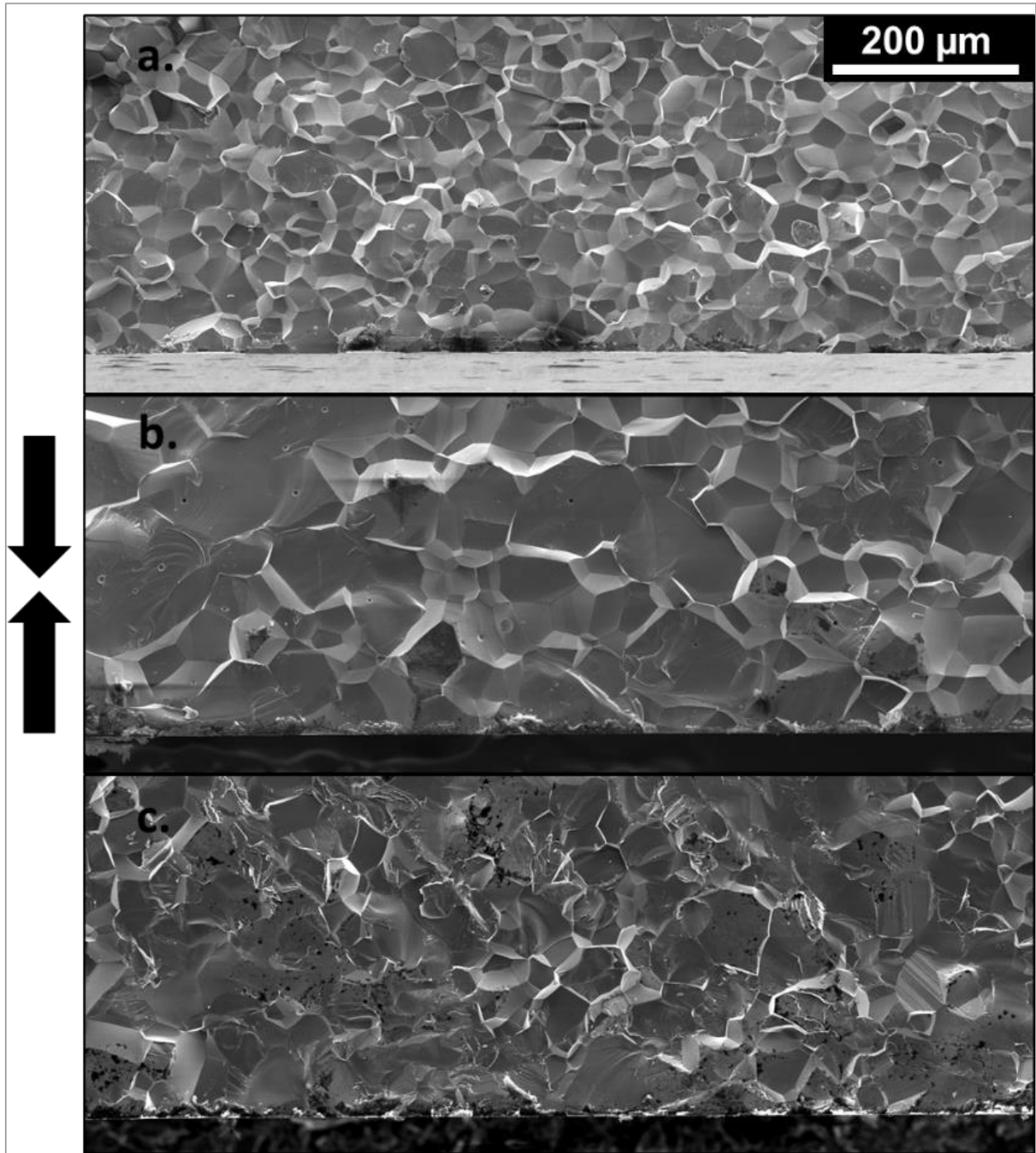
Figure 4.4. Forward-view of the fracture surfaces for the Non-Pre-Aligned (a.), Pre-Aligned (b.), and Equiaxed (c.) samples. The arrows indicate the hot-pressing direction.

During specimen preparation, it was observed that the density of the NPA and E billets were quite uniform across the entire billet, while the PA billets had significant density gradients around the outer perimeter of the billet, as shown in Figure 4.5. This density gradient is thought to be due to differences in effective stress, and differences in strain/recrystallization coupled with a temperature gradient during hot-pressing, as discussed in Section 3. Three of the nine successful PA flexure bars were produced from this outer edge of the billets, resulting in lower relative densities than the center: ρ_e = 98.31 to 98.58%, and ρ_c = 98.92 to 99.41%. The flexure stress of these lower density edge bars resulted in a noticeably lower flexure stress than the center bars: σ_e = 100 to 116MPa, and σ_c = 154 to 201MPa. Because of this significant difference, these three flexure bars were removed from the sample pool, resulting in the six flexure bars used to calculate the average flexure stress of the PA samples, as shown in Table 4.1.
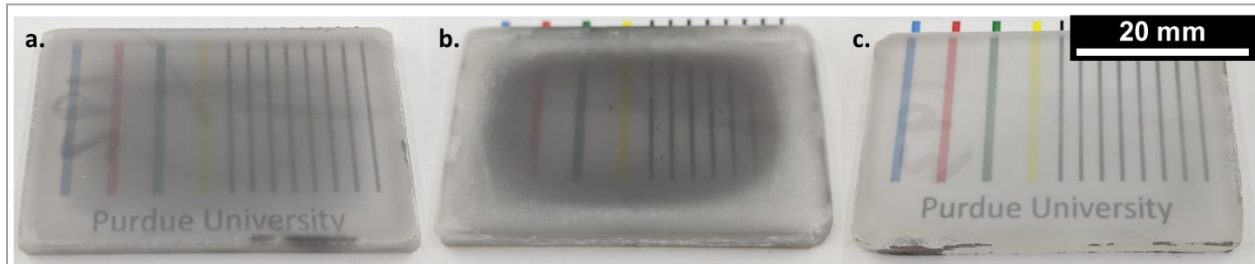
Figure 4.5. Macro images of the Non-Pre-Aligned (a.), Pre-Aligned (b.), and Equiaxed (c.) billets lying flat on paper. The billets are shown before the cutting step at a thickness of d=4.0±0.13mm.

4.4.2 Vickers Hardness

The Vickers hardness of these samples are shown in Table 4.1. For all samples, the hardness is in the 17GPa range. This is lower than the hardness of other transparent alumina found in the literature, which is in the 20GPa range.[8,9] Additionally, those authors reported hardness using a higher indentation load of 10kgf, which results in a lower reported hardness value.[66] The low hardness of the current alumina samples is contributed to their large grain size, as hardness of alumina is known to decrease with increasing grains size.[8]

Table 4.1 also shows the hardness of the alumina samples for both the parallel ($HV_\parallel$) and perpendicular ($HV_\perp$) indentation directions, and this data is plotted as a function of orientation parameter in Figure 4.6. The NPA sample displays the lowest hardness in both directions, while the PA sample has the highest hardness in the ⊥-direction, and the E sample has the highest hardness in the ∥-direction. Additionally, both the NPA and PA samples display a lower hardness

78

in the ‖-direction than the ⊥-direction, while the hardness of the E sample is essentially the same in both directions. When compared to the sapphire sample, it can be seen that the hardness of the NPA and PA samples in their ‖ and ⊥-directions trend similarly with the hardness of sapphire in the corresponding crystallographic directions. Specifically, the hardness of the PA sample is nearly identical to the hardness of sapphire in both directions. This is because the PA sample is very highly crystallographically oriented (low r). Because of this, testing the hardness of the ‖-direction corresponds to the c-axis of alumina crystal structure, while testing the ⊥-direction corresponds to the a-axis of the alumina crystal structure.[17] A similar trend was observed in textured alumina using templated-grain-growth techniques.[70] These trends agree with the hardness of sapphire along its different crystallographic directions.[71]
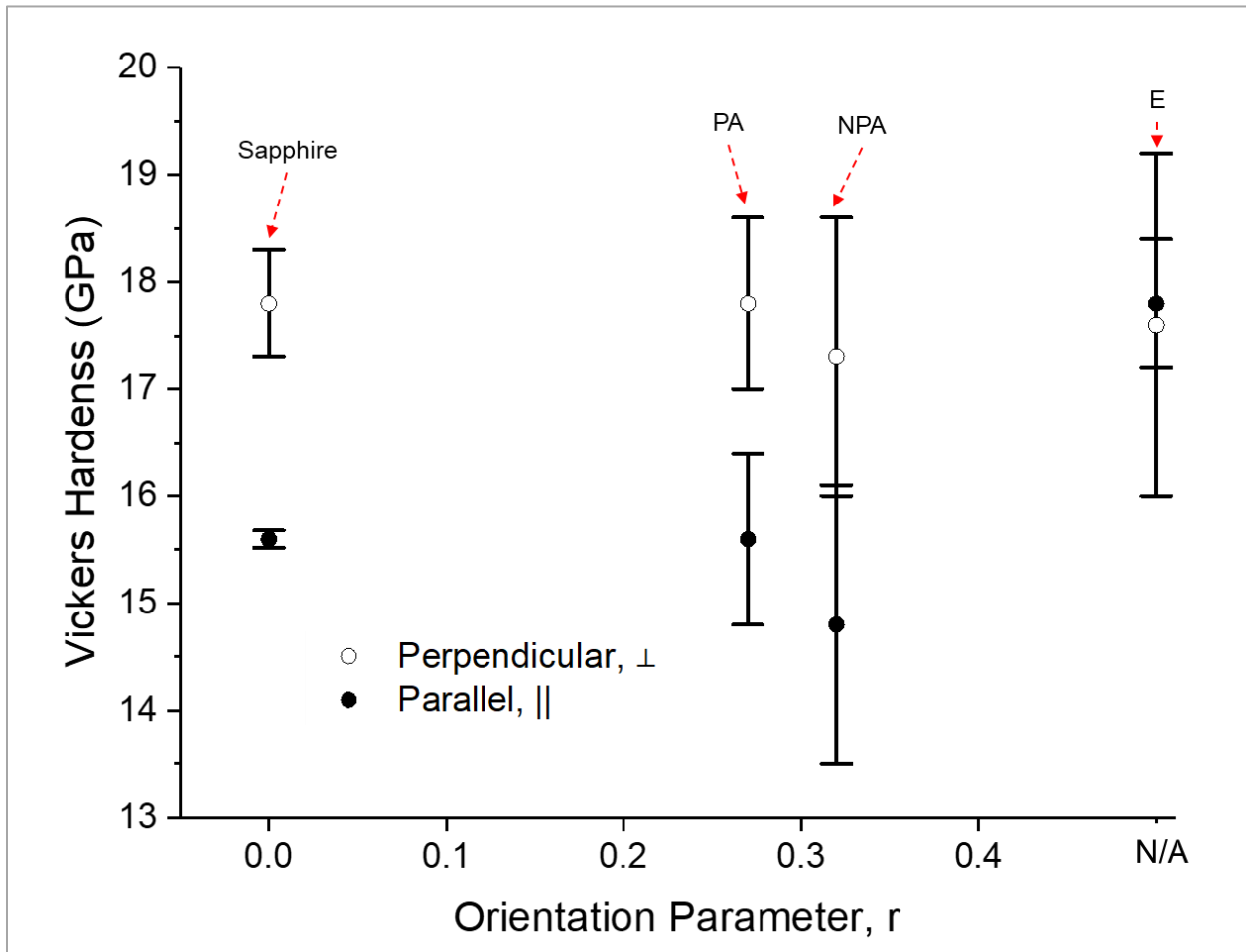
Figure 4.6. Vickers Hardness as a function of orientation parameter, for samples indented parallel and perpendicular to the hot-pressing direction.

4.5 Summary and Conclusions

The flexure stress and hardness of three different powder types of transparent alumina where characterized. All samples exhibited low fracture stresses (~175MPa) and low Vickers hardness (~17GPa), due to their large grain sizes (>60µm). The hot-pressing parameters that are required to achieve transparency (1800°C for 5 hours) are sufficient to result in such a large grain size. Minimal differences in fracture stress were observed among the different powder types, and no crack deflection was observed. Noticeable differences in Vickers hardness were observed among the different powder types, as well as differences in hot-pressing direction. The pre-aligned platelet alumina sample exhibited hardness values nearly identical to sapphire in the corresponding crystallographic directions. This is due to the pre-alignment procedure resulting in significant crystallographic orientation.

5. MODIFICATIONS TO THE RAYLEIGH-GANS-DEBYE MODEL

5.1 Contributions

The individuals listed below contributed the following tasks:

- Andrew Schlup: Sample preparation, optical measurements, mathematical modifications, and data analysis

- William Costakis: Rocking curve measurements and observation that the misalignment angle, and subsequent refractive index mismatch, can be calculated from rocking curves

- Prof. Jeffrey Youngblood: Expertise on optical properties

5.2 Introduction

As previously discussed, Apetz et. al developed a model based on Rayleigh-Gans-Debye light-scattering theory to describe the in-line transmission of fine-grained transparent polycrystalline alumina as a function of wavelength.[7] This has been termed the "Rayleigh-Gans-Debye (RGD) model" in this dissertation, and is given in Section 1.1 as Equation 1. For completeness, Equation 1 has been listed again in this section as Equation 16:

$$T_{ILT} = (1 - R_S)exp\left(-\frac{3\pi^2 r_g \Delta n_g^2 d}{\lambda_0}\right) \qquad 16$$

Where T_{ILT} is the in-line transmission, R_S is the surface reflection, r_g is the grain radius (grain size, $G = 2r_g$), Δn_g is the refractive index mismatch between adjacent grains, d is the sample thickness, and λ_0 is the wavelength. The primary function of this model is to explain why smaller grain sizes result in higher in-line transmission. When the grain size is decreased, the scattering cross section of an individual grain also decreases. This reduces the scattering intensity, resulting in less light to be that scattered at wide angles relative to the incident beam and a higher in-line transmission.[7] When compared to the experimental data of samples produced via low-temperature (~1200°C) HIP'ing of equiaxed alumina powder, the RGD model matches quite well.[7] However, when transparent samples produced via high-temperature (1800°C) hot-pressing of platelet alumina powder are plotted using this model, the curve does not match the experimental data. This is shown

in Figure 5.1, where the experimentally-obtained in-line transmission vs. wavelength of one of the best samples produced in this study (PA, $T_{max} = 1800°C$, $P_i = 0MPa$, $P_{max} = 10MPa$, $t_{iso} = 7hrs$), along with a curve that the same sample should be given the RGD equation. This assumes a grain-size of $G = 2r_g = 68\mu m$ and a refractive index mismatch of $\Delta n_g = 0.005$. The in-line transmission goes to zero because the grain-size is so large. This model does not work well for this sample because the RGD equation does not account for crystallographic orientation. In terms of the RGD equation, a $\Delta n_g = 0.005$ is simply not correct for this sample. Therefore, there is motivation to modify the RGD equation to account for crystallographic orientation and input a refractive index mismatch value that more accurately represents the actual sample.
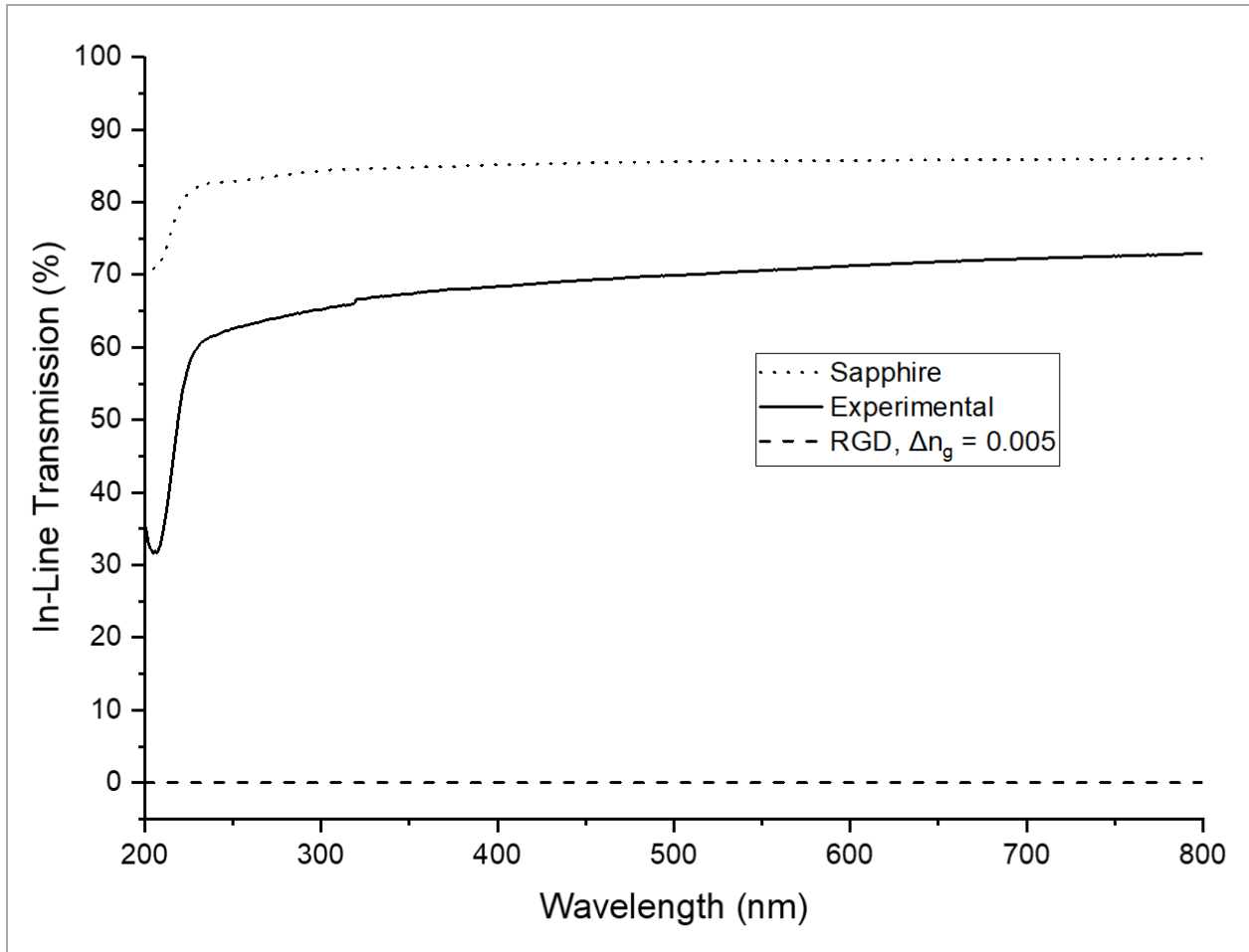
Figure 5.1. In-line transmission as a function of wavelength, showing the experimental data of a hot-pressed pre-aligned platelet alumina sample, along with the same data plotted using the RGD model. This assumes a grain size of $G = 68\mu m$ and a sample thickness of $d = 0.8mm$.

82

Figure 5.2 shows how the in-line transmission curve would shift if the RGD model is used with different Δn_g values. A lower Δn_g effectively raises the curve to be closer to the experimental data. However, the overall shape of the curve still does not match that of the experimental data. Specifically, the sudden shift at ~225nm does not occur. This is because the RGD model does not account for the wavelength dependency of a few key variables: refractive index mismatch, absorption, and porosity. Instead, the RGD model either neglects these variables, or assumes that these variables are independent of wavelength. In this chapter, the RGD model will be modified such that crystallographic orientation is accounted for, as well as wavelength dependency.
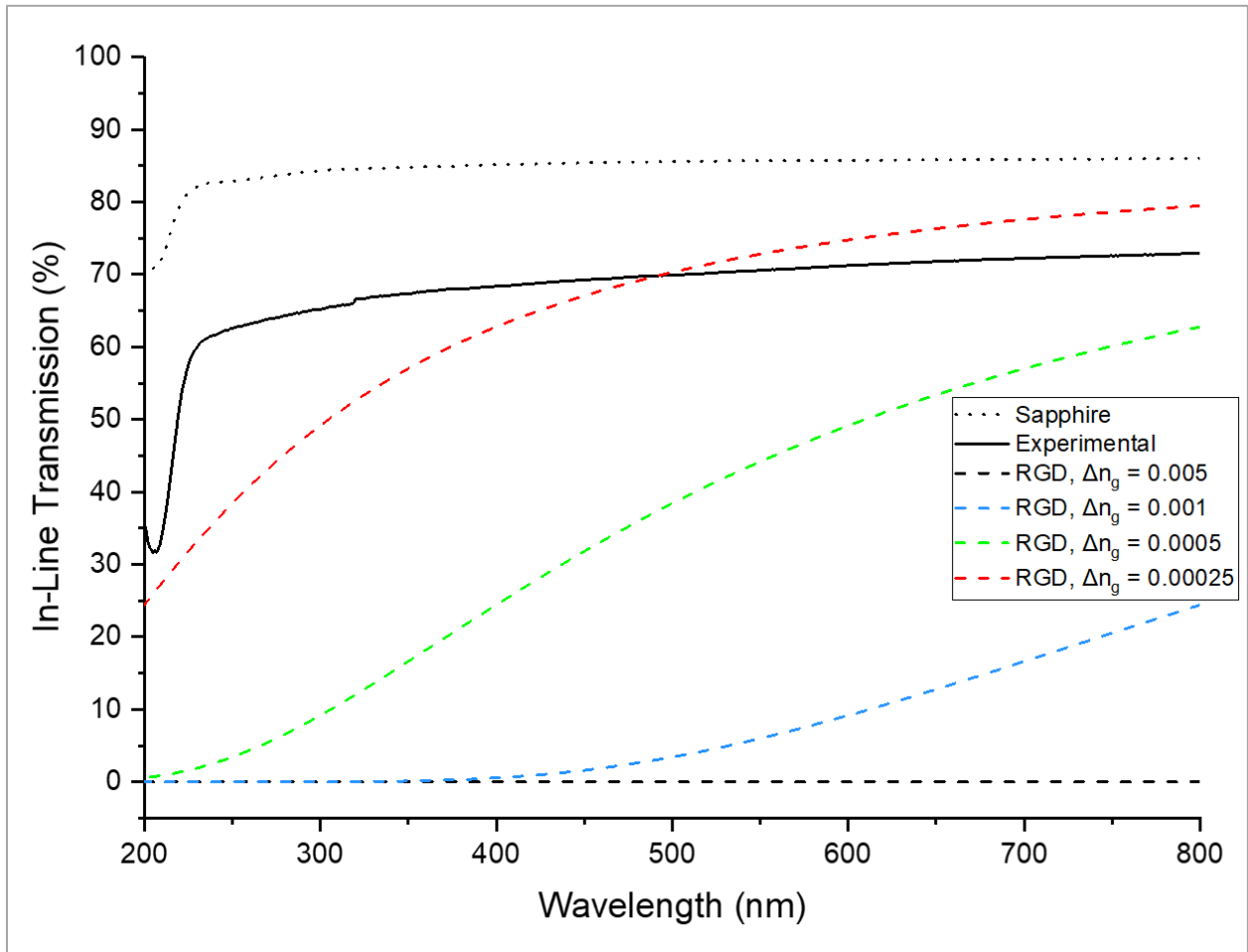
Figure 5.2. In-line transmission as a function of wavelength, showing how changing Δn_g shifts the RGD model curve. This assumes a grain size of G = 68µm and a sample thickness of d = 0.8mm.

5.3 Mathematical Modifications to the Rayleigh-Gans-Debye Model

5.3.1 Accounting for Crystallographic Orientation via Wavelength and Misorientation-Angle Dependent Refractive Index Mismatch

This section discusses modifying the RGD model to account for crystallographic orientation. It is trivial to observe that a sample with a high degree of crystallographic orientation will have a small refractive index mismatch between adjacent grains, Δn_g. The Δn_g portion of Equation 16 can be further defined by Equation 17:

$$\Delta n_g = |n_1 - n_2| \qquad\qquad 17$$

Where n_1 and n_2 are the refractive indices of two adjacent grains. If n_1 and n_2 are very dissimilar (random crystallographic orientation), Δn_g will be large. However, if n_1 and n_2 are very similar (very high crystallographic orientation), Δn_g will be small, and Δn_g will in fact go to zero when $n_1 = n_2$. Therefore, the crystallographic orientation can be accounted for by calculating a precise Δn_g value.

Sections 2.4.5 and 3.4.1 have established that the warm-pressing and hot-pressing processing methods result in samples with significant crystallographic orientation. Additionally, the rocking curve method described in Section 3.3.5 is a reliable way to measure the exact degree of crystallographic misorientation in a sample. Specifically, rocking curves give a distribution of misorientation angles, φ, and the frequency at which those misorientation angles are present within a sample. Figure 5.3 illustrates what is meant by the misorientation angle. In an actual pre-aligned platelet alumina sample, the crystallographic misorientation between two adjacent grains will be much lower than this.
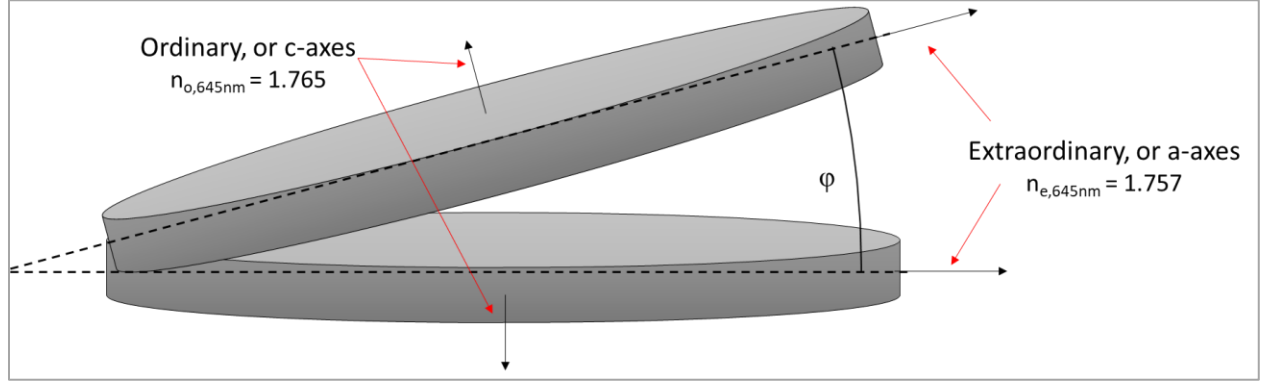
Figure 5.3. Schematic illustrating the misorientation angle between two adjacent alumina platelets.

With this in mind, the equation given by Harris et al.[17] can be used, which describes the refractive index of a light ray that is traveling at an angle φ with respect to the c-axis:

$$n_\varphi = \frac{n_{o,\lambda_0} \cdot n_{e,\lambda_0}}{\sqrt{{n_{e,\lambda_0}}^2 cos^2\varphi + {n_{o,\lambda_0}}^2 sin^2\varphi}}$$

18

Where n_{o,λ_0} and n_{e,λ_0} are the Sellmeier dispersion equations for the ordinary and extraordinary axis of sapphire, and are given in Equations 19 and 20, respectively:[17]

$$n_{o,\lambda_0} = \sqrt{1 + \frac{1.431349\lambda_0^2}{\lambda_0^2 - 0.0726631^2} + \frac{0.65054713\lambda_0^2}{\lambda_0^2 - 0.1193242^2} + \frac{5.3414021\lambda_0^2}{\lambda_0^2 - 18.028251^2}}$$

19

$$n_{e,\lambda_0} = \sqrt{1 + \frac{1.5039759\lambda_0^2}{\lambda_0^2 - 0.0740288^2} + \frac{0.55069141\lambda_0^2}{\lambda_0^2 - 0.1216529^2} + \frac{6.5927379\lambda_0^2}{\lambda_0^2 - 20.072248^2}}$$

20

The "n_1" portion of Equation 17 can be replaced with Equation 19, and the "n_2" portion can be replaced with Equation 18, giving an equation that describes the wavelength and misorientation-angle dependent refractive index mismatch between adjacent grains:

$$\Delta n_{g,\lambda_0,\varphi} = \left| n_{o,\lambda_0} - \frac{n_{o,\lambda_0} \cdot n_{e,\lambda_0}}{\sqrt{n_{e,\lambda_0}{}^2 cos^2\varphi + n_{o,\lambda_0}{}^2 sin^2\varphi}} \right| \qquad 21$$

In order to calculate the misorientation angle, φ, the data given from rocking curve analysis is considered. Figure 5.4 shows the rocking curve for the sample discussed in Figure 5.1. The rocking curve data is a normal distribution of misalignment angles (more specifically measurement angle omega, Ω, but it will be referred to as φ for now) from 0 to 40°. This is illustrated by the platelets inset in the plot, showing how misalignment angle between adjacent grains changes, as well as how the refractive index mismatch will increase with increasing misalignment angle.
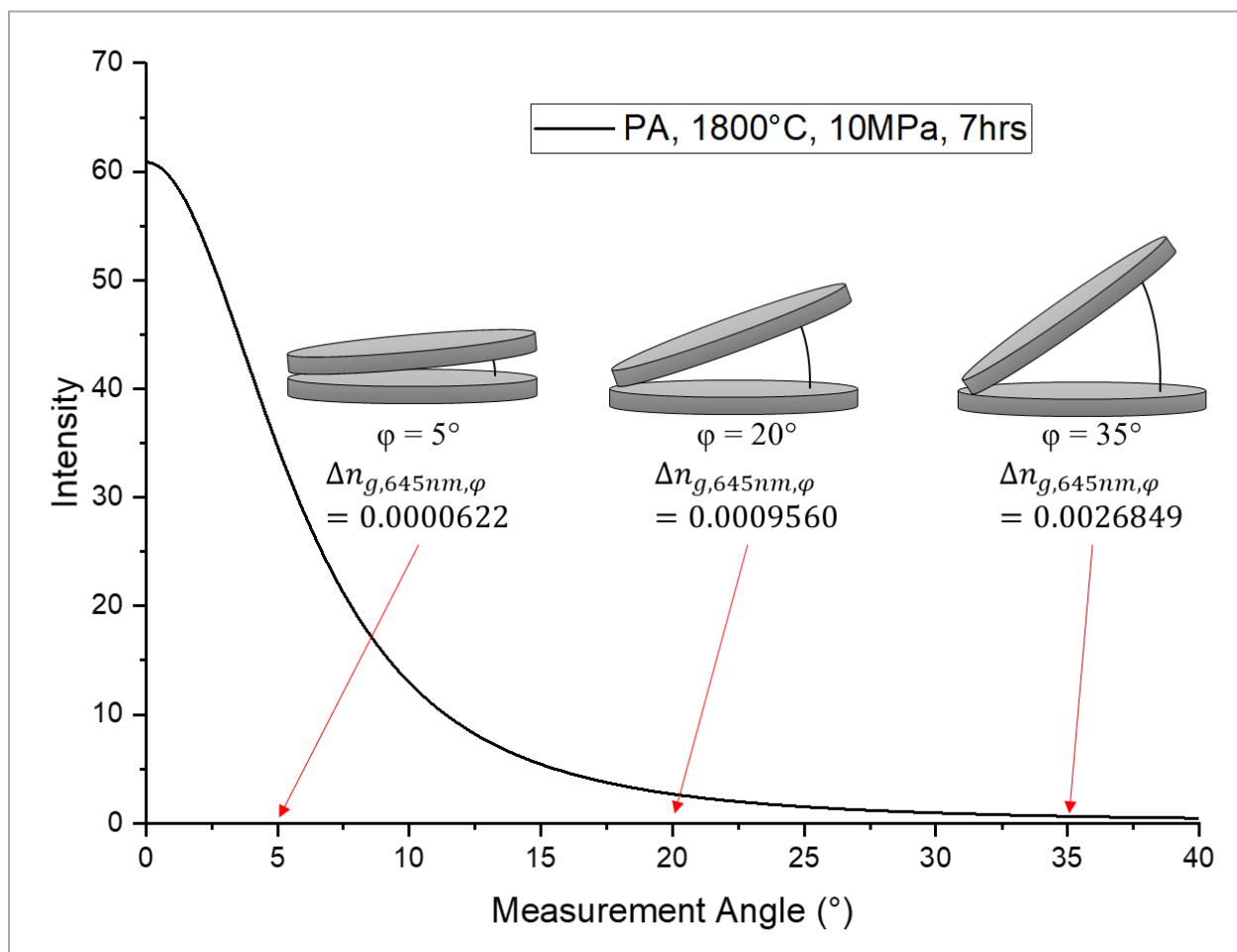
Figure 5.4. Rocking curve of a Pre-Aligned (PA) platelet alumina sample. The inset images illustrate the misorientation angle between two adjacent platelets, and the resulting refractive index mismatch.

For this particular sample, the rocking curve data indicates that the majority of the grains have a misalignment angle that is less than ~5°. Specifically, the full-width at half-max (FWHM) of this sample is 11.37° (this is considering both sides of the rocking curve, only one side is shown in Figure 5.4 for convenience). The standard deviation angle of the FWHM is first calculated, as shown in Equation 22:

$$Std. Dev. (°) = \frac{FWHM}{2\sqrt{2 \ln 2}}$$

22

This standard deviation angle is then used to establish a Z-score distribution function, and resulting probability, P. This calculation was performed using Microsoft Excel® (365 MSO) functions, as shown in Table 5.1. This probability describes the frequency at which each misorientation angle (φ) occurs within the sample. A sample with a very high degree of crystallographic alignment is shown in Table 5.1, so the frequency at which high misorientation angles (>40°) occur is very low (P = ~0.0), while the frequency at which low misorientation angles (<5°) occur is very high (P = ~0.14). Because this is a distribution, the sum of all these probabilities will be equal to 1.

Table 5.1. Z-score distribution function calculations.

FWHM:	11.37		
Std. Dev. (°):	4.83		
Mean (°):	0		
Angle, φ (°)	Z-score, Z-s	Z-score Probability (Cumulative), Z-s P	Probability, P
45	$= \frac{(\varphi - \text{Mean})}{Std.Dev.}$	$= NORM.S.DIST(\text{Z-s}, TRUE) - 0.5$	$= 2(\text{Z-s } P_{\varphi=45} - \text{Z-s } P_{\varphi=44})$
44	9.113	0.500	0
43	8.906	0.500	0
42	8.699	0.500	0
-	-	-	-
-	-	-	-
-	-	-	-
3	0.621	0.233	0.144
2	0.414	0.161	0.157
1	0.207	0.082	0.164

Next, these probabilities are applied to the refractive index mismatch (Equation 21) in the following manner:

$$\Delta n_{g,\lambda_0,\varphi,P} = P \cdot \left| n_{o,\lambda_0} - \frac{n_{o,\lambda_0} \cdot n_{e,\lambda_0}}{\sqrt{n_{e,\lambda_0}^2 \cos^2\varphi + n_{o,\lambda_0}^2 \sin^2\varphi}} \right| \qquad 23$$

This means that at a particular misorientation angle, there is a finite probability that the resulting refractive index mismatch actually occurs within the sample. Then, the refractive index mismatch is summed for each misorientation angle, resulting in a final refractive index mismatch at a particular wavelength, as shown in Equation 24. It is important to note that the misorientation angle, φ, must first be converted to radians. This probability calculation and resulting summation is illustrated in Table 5.2.

$$\sum \Delta n_{g,\lambda_0,\varphi,P} = \sum_{\varphi=1°}^{45°} P \cdot \left| n_{o,\lambda_0} - \frac{n_{o,\lambda_0} \cdot n_{e,\lambda_0}}{\sqrt{n_{e,\lambda_0}^2 \cos^2\varphi + n_{o,\lambda_0}^2 \sin^2\varphi}} \right| \qquad 24$$

Combining Equations 16 and 24 gives the first modification to the RGD model, accounting for crystallographic orientation:

$$T_{ILT} = (1 - R_S)exp\left(-\frac{3\pi^2 r_g \sum \Delta n_{g,\lambda_0,\varphi,P}^2 d}{\lambda_0} \right) \qquad 25$$

Table 5.2. Probability calculation and summation of wavelength-dependent refractive index-mismatch.

Wavelength (nm)	Ordinary refractive index, n_{o,λ_0} (Equation 19)	Extraordinary refractive index, n_{e,λ_0} (Equation 20)	Angle, φ							$\sum \Delta n_{g,\lambda_0,\varphi,P}$ (Equation 24)
			Degrees	1	2	-	-	44	45	
			Radians	0.017	0.035	-	-	0.750	0.768	
			Probability, P (from Table 5.1)							
				0.164	0.157	-	-	0.000	0.000	
			$\Delta n_{g,\lambda_0,\varphi,P}$ (Equation 23)							
800	1.76013	1.75205		4.06847E-07	1.55881E-06	-	-	0	0	6.77065E-05
799	1.76016	1.75207		4.06849E-07	1.55882E-06	-	-	0	0	6.77068E-05
798	1.76019	1.75210		4.06850E-07	1.55883E-06	-	-	0	0	6.77071E-05
797	1.76021	1.75213		4.06852E-07	1.55883E-06	-	-	0	0	6.77074E-05
-	-	-		-	-	-	-	-	-	-
-	-	-		-	-	-	-	-	-	-
203	1.906566	1.895585		5.53562E-07	2.12094E-06	-	-	0	0	9.2119E-05
202	1.908569	1.897551		5.55412E-07	2.12803E-06	-	-	0	0	9.2427E-05
201	1.910616	1.899562		5.57285E-07	2.13520E-06	-	-	0	0	9.2738E-05
200	1.912709	1.901617		5.59182E-07	2.14247E-06	-	-	0	0	9.3054E-05

Figure 5.5 shows how accounting for crystallographic orientation using Equation 25 shifts the in-line transmission curve. In this case, the modified RGD yields an in-line transmission that is far higher than the experimental data and is in fact nearly identical to single crystal sapphire. This is clearly not correct and indicates that further modifications must be made. However, the fact that the in-line transmission is no longer equal to zero suggests that this modification might, so far, be valid.
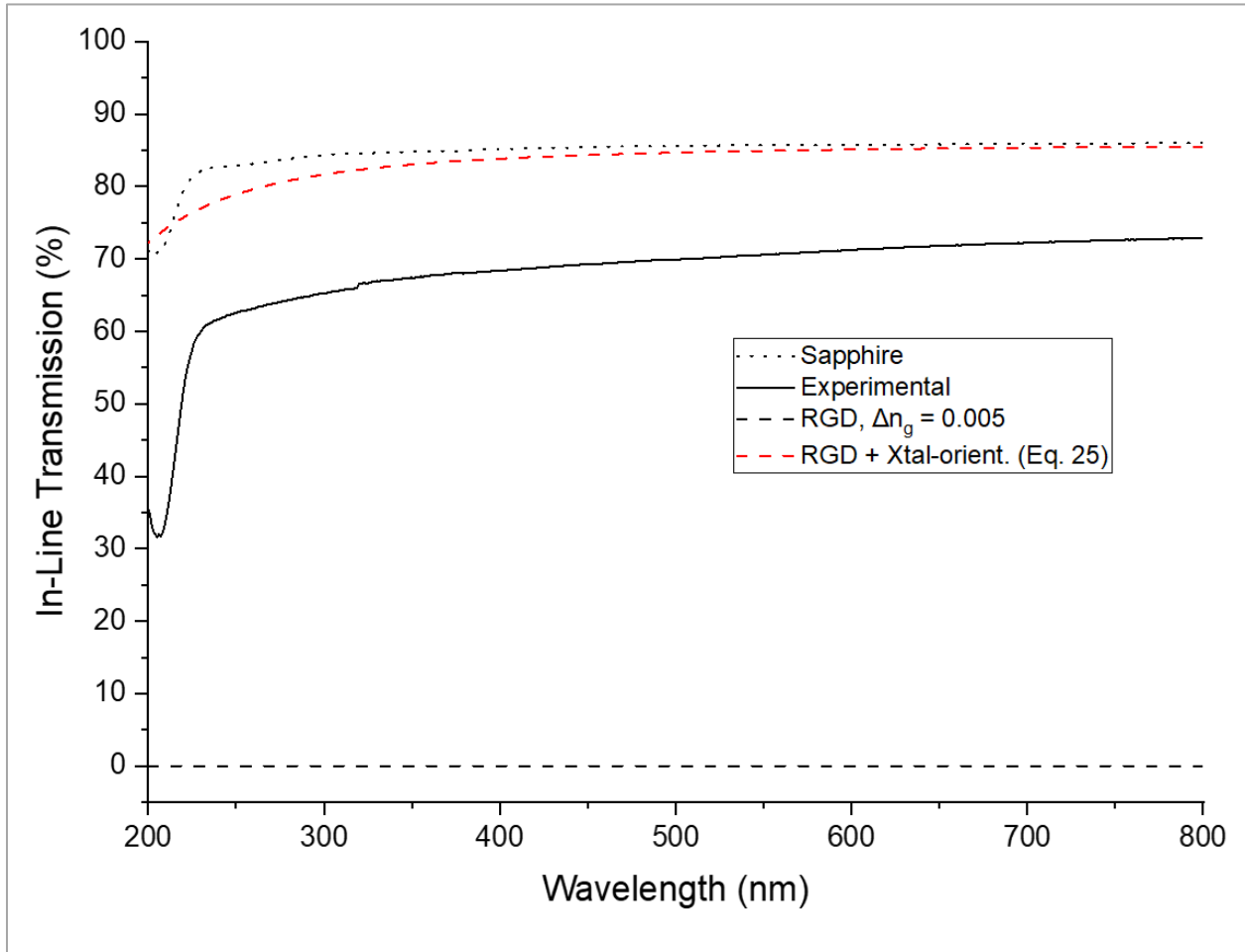
Figure 5.5. In-line transmission as a function of wavelength, illustrating how the curve shifts when crystallographic orientation is accounted for. This assumes a sample thickness of d = 0.8mm, a grain size of G = 68µm, and a FWHM = 11.37°.

5.3.2   Accounting for Wavelength-Dependent Absorption

As discussed in Section 2.4.2, the platelet alumina samples produced in this research have some amount of optical losses due to absorption, which qualitatively manifests as a discoloration in the samples. While this absorption has been minimized by optimizing the processing parameters,

it is still important to account for it in the modified RGD model. Apetz' paper assumes zero absorption in their samples, so their model disregards absorption entirely. While it may be possible to mathematically account for absorption using Beer's Law, or even considering the band-gap absorption losses in sapphire using Urbach's formula,[72] initial attempts at deriving such mathematical solutions proved to be difficult. Therefore, a simpler approach will be taken, in which experimentally measured absorption data is incorporated into the modified RGD equation.

Consider Equation 2, which can be rearranged as follows:

$$T = 100\% - R - A \qquad\qquad 26$$

In this, the "100% - R" is equivalent to the "1 - R_S" portion of Equation 25, where "100%" is simply a percentage, and "1" is simply a fraction. Additionally, it can be seen that this is where Apetz' model disregards absorption. Therefore, the "1 - R_S" portion of Equation 25, can be replaced with Equation 26, yielding the following:

$$T_{ILT} = (1 - R_S - A)exp\left(-\frac{3\pi^2 r_g \sum \Delta n_{g,\lambda_0,\varphi,P}^2 \, d}{\lambda_0}\right) \qquad\qquad 27$$

There is now a variable in the modified RDG model that accounts for absorption. This variable will be inserted as an experimentally measured absorption, A_{exp}, as discussed in Section 2.3.7 and Equation 5. Because this absorption measurement method is performed across the entire optical spectrum, it inherently accounts for wavelength dependency. For the sake of completeness, the equation for absorption will be listed in this section as Equation 28:

$$A_{exp,\lambda_0} = \frac{I - I_{raw}}{2} \qquad\qquad 28$$

Experimentally measured absorption as a function of wavelength for the sample shown in Figure 5.1, as well as a sapphire sample, is shown in Figure 5.6. At the higher wavelengths (400-800nm), absorption is mostly wavelength-independent for both samples. However, at the lower wavelengths (<300nm), there is a sudden decrease then increase in absorption. The gradual

decrease between 225 and 300 nm is not understood, though it is speculated that it is an artifact of the measurement technique. The sudden increase at 225nm, however, is known to be an artifact of the absorption band-gap of sapphire.[73] This is important, as it will further account for the overall shape of the in-line transmission curve, specifically the shift at 225nm, as seen in Figure 5.1.
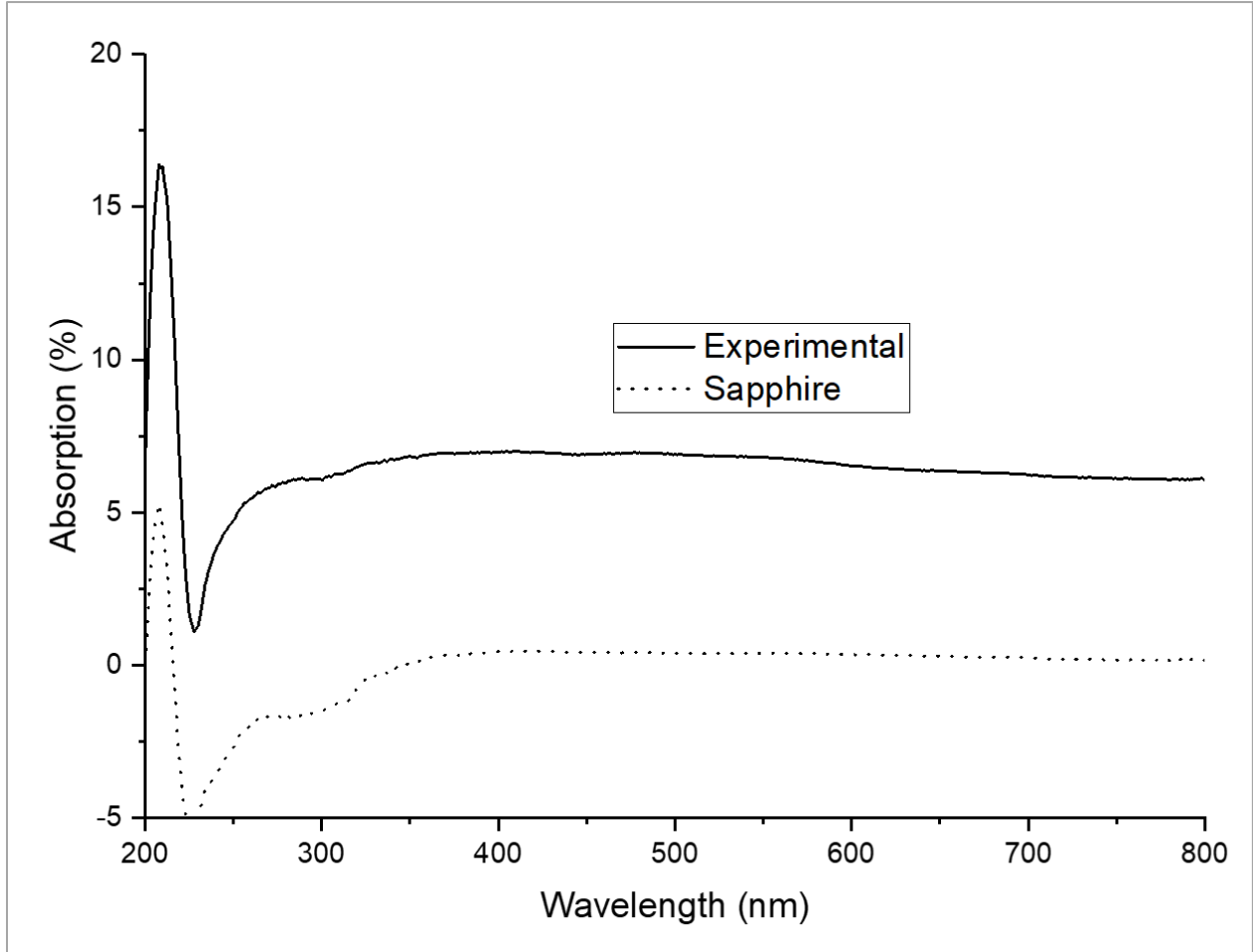
Figure 5.6. Experimentally measured absorption as a function of wavelength, illustrating the importance of accounting for wavelength-dependency.

Combining Equations 27 and 28 gives the next modification to the RGD model:

$$T_{ILT} = \left(1 - R_S - A_{exp,\lambda_0}\right) exp \left(- \frac{3\pi^2 r_g \sum \Delta n_{g,\lambda_0,\varphi,P}{}^2 d}{\lambda_0}\right)$$ 29

Figure 5.7 shows how accounting for wavelength-dependent absorption in Equation 29 shifts the in-line transmission curve. This effectively shifts the curve closer to the experimental data. Additionally, the sudden shift at ~225nm is now being accounted for. The overall curve is still not as low as the experimental data, so further modifications are necessary.
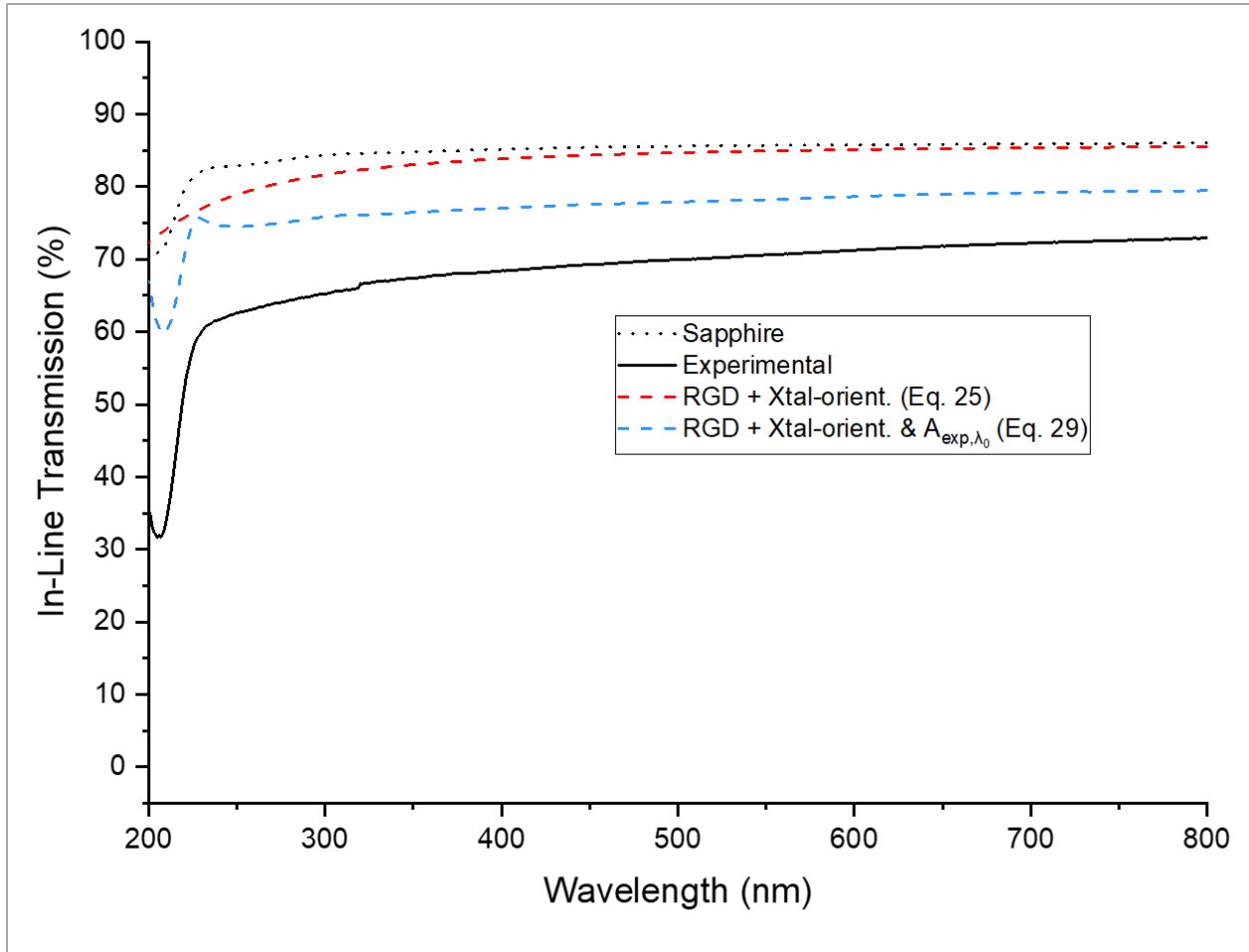
Figure 5.7. In-line transmission as a function of wavelength, illustrating how the curve shifts when wavelength-dependent absorption is accounted for. This assumes a sample thickness of d = 0.8mm, a grain size of G = 68μm, and a FWHM = 11.37°.

5.3.3 Accounting for Wavelength-Dependent Porosity

In Apetz' paper, the transparent alumina samples used were assumed to have zero porosity, and therefore porosity was neglected in the RGD model. While the porosity of the samples produced in this research has been minimized by optimizing the processing parameters, it is still important to account for porosity in the modified RGD model. And as has been the theme of these modifications thus far, it is important to account for the wavelength dependency of porosity.

In Apetz' derivation, in-line transmission was first defined as the following:[7]

$$T_{ILT} = (1 - R_S)exp(-\gamma d) \tag{30}$$

Where γ is the total scattering coefficient. This total scattering coefficient is the sum of the grain-boundary (γ_{gb}) and pore-scattering (γ_p) components:[7]

$$\gamma = \gamma_{gb} + \gamma_p \tag{31}$$

It is here where Apetz neglected the pore-scattering component by setting it equal to zero.[7] Instead, the pore-scattering component will be included. First, the grain boundary scattering component is defined by the following equation:[7]

$$\gamma_{gb} = N_g C_{sca,g} \tag{32}$$

Where N_g is the density (#/volume) of spherical grains in a sample, and $C_{sca,g}$ is the scattering cross section of a spherical grain. Apetz assumed that this volume fraction of spherical grains is equal to ½, giving the following equation:[7]

$$N_g = \frac{1}{2}\frac{1}{\frac{4}{3}\pi r_g^3} \tag{33}$$

Where r_g is the average radius of the grains in the polycrystalline alumina sample. Combining Equations 32 and 33 give the following equation:[7]

$$\gamma_{gb} = \frac{1}{\frac{8}{3}\pi r_g^3} C_{sca,g} \tag{34}$$

Next, the pore-scattering component is defined by the following equation:[7]

$$\gamma_p = N_p C_{sca,p} \qquad 35$$

Where N_p is the density (#/volume) of spherical pores in a sample, and $C_{sca,p}$ is the scattering cross section of a spherical pore. N_p is the same as Equation 33, except the volume fraction of pores can be expressed in terms of a percentage of porosity, p:

$$N_p = p \frac{1}{\frac{4}{3}\pi r_p^3} \qquad 36$$

Where r_p is the average radius of the pores in the polycrystalline alumina sample, and the percentage of porosity, p, is expressed as a fraction, meaning that a value of $p = 0.001$ is equivalent to a relative density of $\rho = 99.9\%$. Combining Equations 35 and 36 give the following equation:[7]

$$\gamma_p = \frac{p}{\frac{4}{3}\pi r_p^3} C_{sca,p} \qquad 37$$

This equation assumes that all pores have the same radius, and only single scattering occurs.

Next, it is assumed that the equation Apetz used for the scattering cross section of a spherical grain can also be used for the scattering cross section of a spherical pore:[7]

$$C_{sca,g} = \frac{8\pi^3 r_g^4}{\lambda_m^2}\left(\frac{\Delta n_g}{n}\right)^2 \qquad 38$$

$$C_{sca,p} = \frac{8\pi^3 r_p^4}{\lambda_m^2}\left(\frac{\Delta n_p}{n}\right)^2 \qquad 39$$

Where n is the average refractive index of polycrystalline alumina (n = 1.76) and λ_m is the wavelength of incident light in the medium, which is defined by the following:

$$\lambda_m = \frac{\lambda_0}{n} \qquad 40$$

Δn_p in Equation 39 is the refractive index mismatch between the surrounding polycrystalline alumina matrix and a pore. This is where wavelength-dependency can begin to be incorporated, as shown in Equation 41:

$$\Delta n_{p,\lambda_0} = \left| n_{o,\lambda_0} - n_p \right| \tag{41}$$

Where n_{o,λ_0} is the wavelength-dependent refractive index of the ordinary axis of sapphire, as shown in Equation 19, and n_p is the refractive index of the gas within the pore. Attempts were made to account for the wavelength-dependency of the refractive index of the gas within the pore, as well as determine if there were significant differences when different types of gasses were used. While the Sellmeier dispersion equations for nitrogen,[74] argon,[75] air,[76] and oxygen[77] do establish wavelength dependency, there is virtually zero change across the optical spectrum. Additionally, the differences in the average refractive index between these gasses are so small and so similar to the refractive index of a vacuum (n = 1), that the refractive index of a vacuum can be assumed for the sake of simplicity. Therefore, $n_p = 1$.

Combining Equations 32, 38, and 40 gives the complete grain boundary scattering component:[7]

$$\gamma_g = \frac{3\pi^2 r_g \Delta n_g^2}{\lambda_0^2} \tag{42}$$

Combining Equations 37, 39, 40, and 41 gives the complete pore-scattering component:[7]

$$\gamma_p = \frac{6p\pi^2 r_p \Delta n_{p,\lambda_0}^{\ 2}}{\lambda_0^2} \tag{43}$$

Moreover, combining Equations 31, 42, and 43 gives the total scattering coefficient:

$$\gamma = \frac{3\pi^2 \left(r_g \Delta n_g^{\ 2} + 2p r_p \Delta n_{p,\lambda_0}^{\ 2} \right)}{\lambda_0^2} \tag{44}$$

Combining Equations 30 and 44 gives the following:

$$T_{ILT} = (1 - R_S)exp\left(\frac{-3d\pi^2\left(r_g\Delta n_g{}^2 + 2pr_p\Delta n_{p,\lambda_0}{}^2\right)}{\lambda_0^2}\right) \qquad 45$$

Finally, combining Equation 45 with what has been derived so far in Equation 29 gives the modified RGD model that accounts for wavelength-dependent porosity:

$$T_{ILT} = \left(1 - R_S - A_{exp,\lambda_0}\right)exp\left(\frac{-3d\pi^2\left(r_g\sum\Delta n_{g,\lambda_0,\varphi,P}{}^2 + 2pr_p\Delta n_{p,\lambda_0}{}^2\right)}{\lambda_0^2}\right) \qquad 46$$

Figure 5.8 shows the in-line transmission as a function of wavelength using Equation 46, accounting for wavelength-dependent porosity. This effectively shifts the in-line transmission curve closer to the experimental data and is a much better fit than the original RGD model.
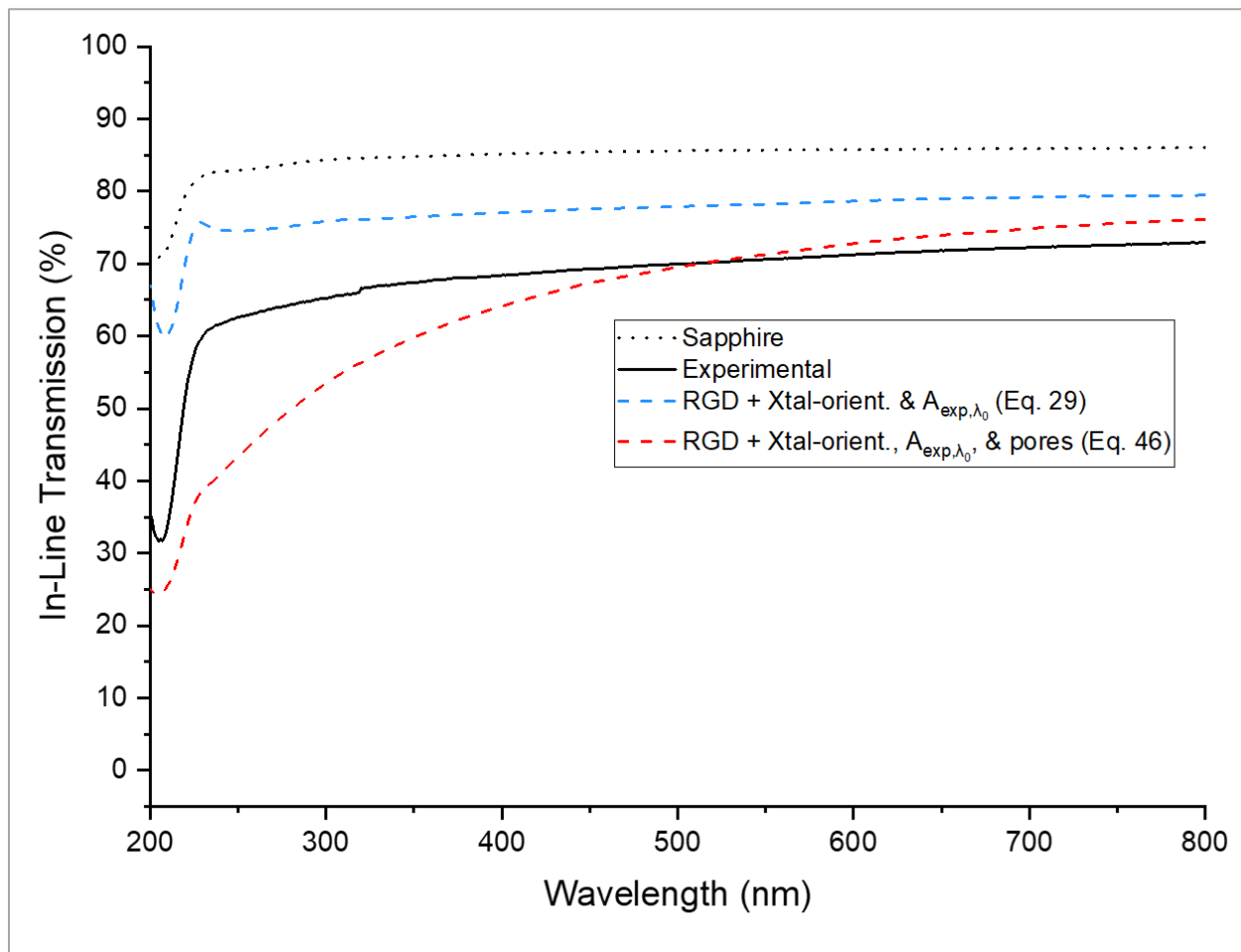
Figure 5.8. In-line transmission as a function of wavelength, illustrating how the curve shifts when wavelength-dependent porosity is accounted for. This assumes a sample thickness of d = 0.8mm, a grain size of G = 68µm, a porosity of p = 0.0001 (0.01%), a pore radius of r_p = 10nm, and a FWHM = 11.37°.

5.4   Discussion

Figure 5.9 shows the in-line transmission as a function of wavelength, comparing the modified RGD model (Equation 46) to the experimental data of two separate samples with differing amounts of crystallographic orientation, as reported by Costakis et al.[58] The model curves assume that wavelength-dependent crystallographic orientation is accounted for, with a FWHM of 11.38° and 13.4° for the pre-aligned (PA) and non-pre-aligned (NPA) samples, respectively. Additionally, this assumes that all other variables are constant between the two samples: thickness of d = 0.8mm, grain size of G = 68µm, porosity of p = 0.0001 (0.01%), and pore radius of r_p = 10nm. While the overall shape of the modified RGD model better fits the experimental data, it

does not accurately represent the differences between these two samples. In particular, notice how the in-line transmission of the NPA model surpasses the PA model at higher wavelengths. This should not be the case, as the NPA sample has a lower degree of crystallographic orientation, and should remain lower than the PA sample across all wavelengths.
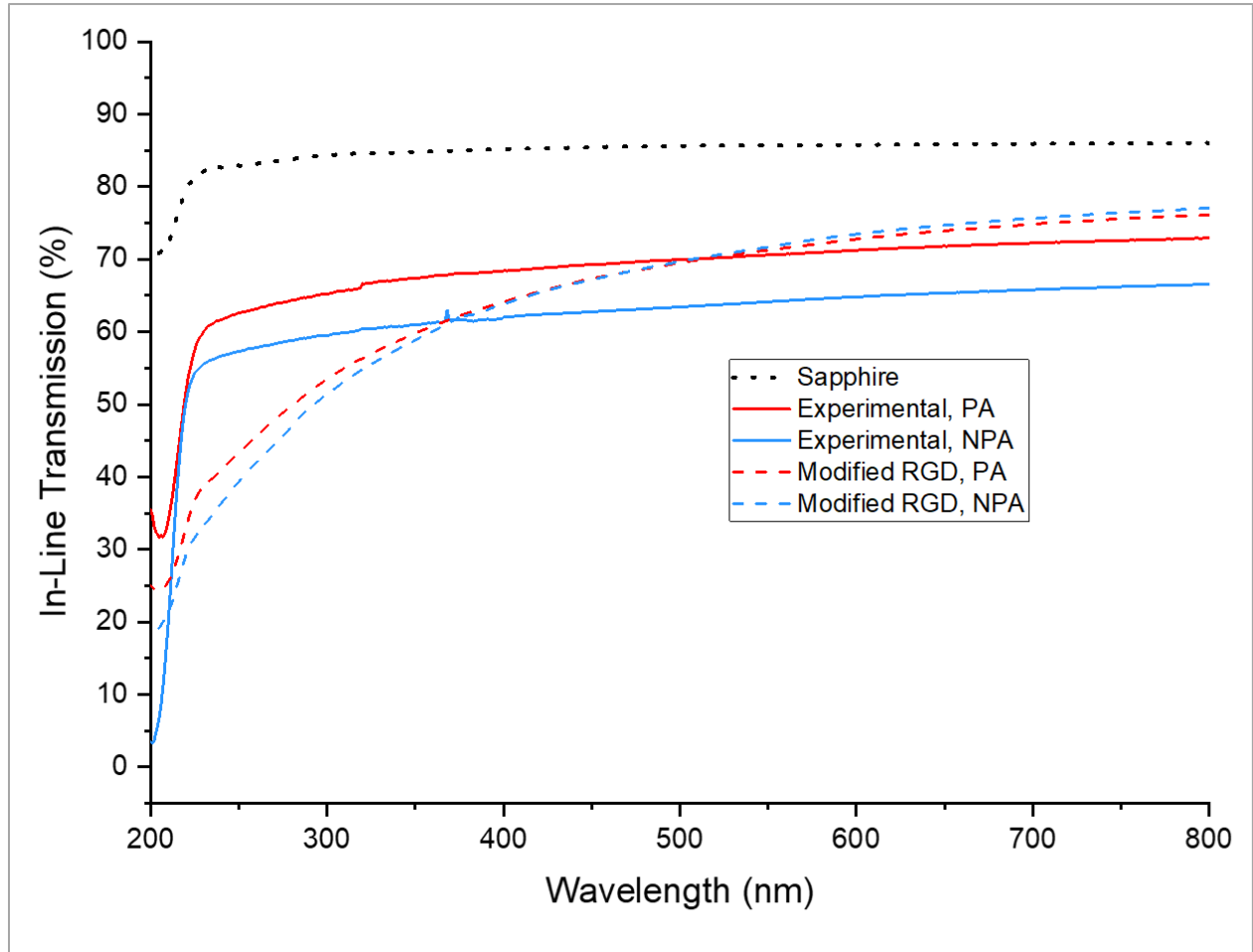
Figure 5.9. In-line transmission as a function of wavelength, illustrating how the model matches samples with different degrees of crystallographic orientation: $FWHM_{PA} = 11.38°$ and $FWHM_{NPA} = 13.4°$.

The reason for the discrepancy observed in Figure 5.9 is not well understood, though a few explanations are possible. One possible explanation is that the method in which the refractive index mismatch is calculated (Section 5.3.1) does not yield an accurate value and may result in a lower value than is actually the case for the samples. A lower value would incorrectly increase the overall in-line transmission. It is possible that some sort of correction factor is required in the mathematical derivation of the refractive index mismatch.

99

Another explanation is that accounting for wavelength dependent porosity using Rayleigh-Gans-Debye scattering theory may not be valid because the system is not refractive index matched ($\Delta n_p \approx 0.76$), as mentioned by Apetz.[7] This means that the assumption made in Section 5.3.3 that the scattering cross section of a spherical grain (Equation 38) can also be used for the scattering cross section of a spherical pore (Equation 39) is incorrect. Instead, Apetz states that Mie scattering theory must in applied to calculate the scattering cross section of a pore.[7] Such calculations can only be done numerically, so future work must be done to explore this.

Another reason for the discrepancy is that the use Rayleigh-Gans-Debye scattering theory may not even be valid when considering large-grained transparent ceramics. This is mentioned by Apetz,[7] where it is stated that the scattering cross section of a spherical grain ($C_{sca,g}$) can be approximated by Equation 38 only when the phase shift caused by the scattering grains is small. While Apetz does not specify what defines "small", it is assumed that the grain size of the samples produced in this research (>60µm) might not meet this criterion. Instead, a geometrical approach[78] or even a wave-retardation theory approach[79,80] may be more appropriate for predicting the in-line transmission of large-grained transparent alumina.

While the modified RGD model does not behave as well as expected, it is still a better overall fit for highly crystallographically oriented alumina than the original RGD model, and can be used to predict certain behaviors, specifically the relationship between crystallographic orientation and grain size. Figure 5.10, Figure 5.11, and Figure 5.12 show the in-line transmission as a function of wavelength of the modified RGD model and how the curves will shift as crystallographic orientation (FWHM) and grain size (G) is varied using hypothetical values. These figures all assume a sample thickness of d = 0.8mm, a porosity of p = 0.0001 (0.01%), and a pore radius of r_p = 10nm. FWHM values of 5°, 20°, and 45° are chosen as they represent the extremes of crystallographic orientation that are possible, with 5° corresponding to a high degree of orientation, and 45° corresponding to a low degree of orientation. Grain size values of 0.5, 50, and 100 microns are chosen as they similarly represent the extremes of grain size in polycrystalline transparent alumina. For a high degree of crystallographic orientation (FWHM = 5°), grain size dependency is effectively negligible, as shown in Figure 5.10. This is because the average misorientation angle between adjacent grains is so low that the refractive index mismatch between grains is effectively zero, eliminating grain size dependency entirely, even for extremely coarse grain sizes like 100µm. This can even be extrapolated to a further extreme: a single crystal of sapphire has a FWHM of 0°,

and the grains size is as large as the single crystal itself. In this extreme case, it is known that the in-line transmission will be at the theoretical max ($T_{ILT} = 84\%$), as shown in Figure 5.10. However, this is assuming that there are no absorption losses, which can equate to ~5 to 10% in optical loss.
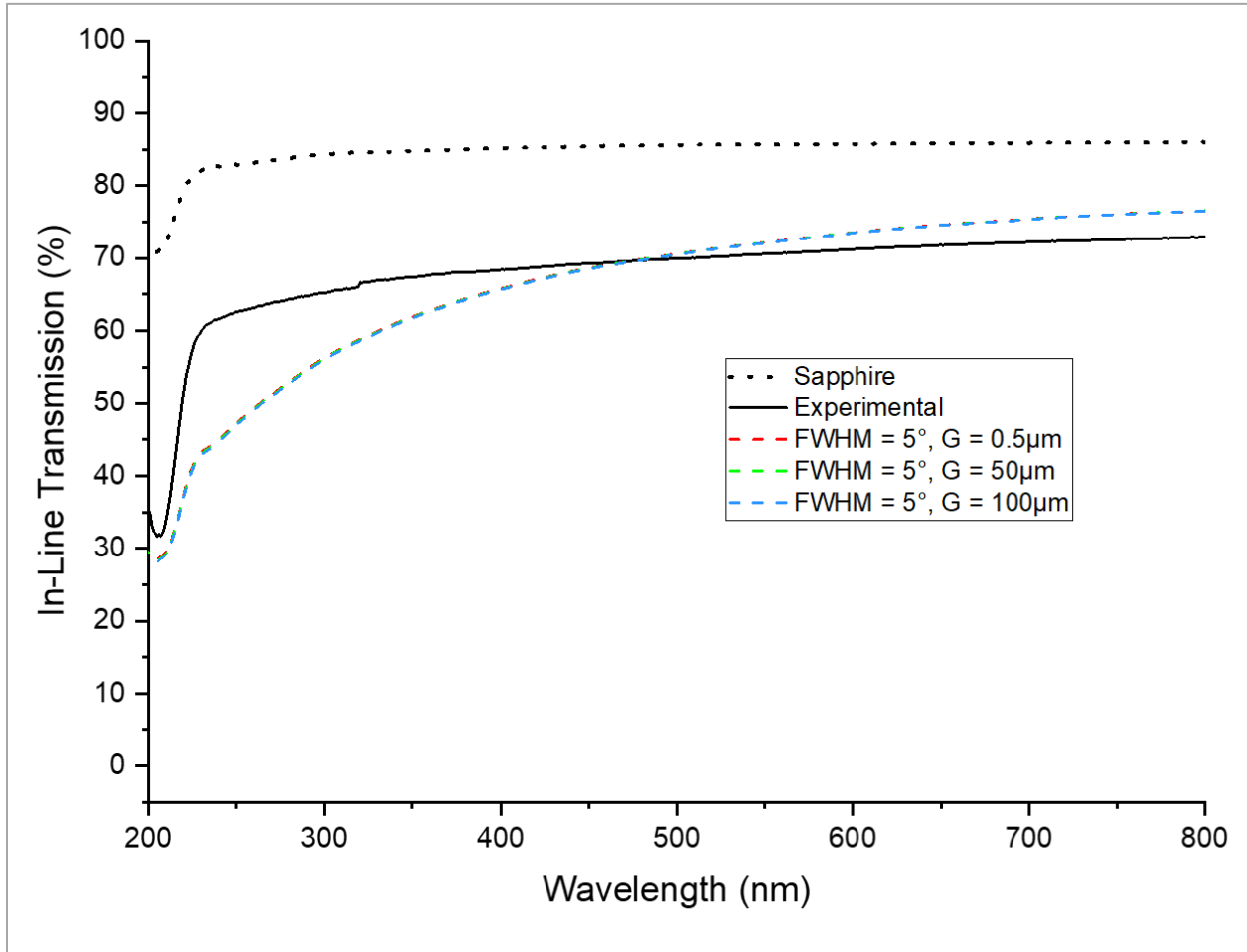
Figure 5.10. In-line transmission as a function of wavelength, illustrating how a grain size (G) affects the curve at high degrees of crystallographic orientation (low FWHM).

For intermediate degrees of crystallographic orientation (FWHM = 20°, Figure 5.11), grain size dependency does begin to become an issue. At small grain sizes (G = 0.5µm), the in-line transmission is still high across the entire optical spectrum. This is because the scattering cross section of the grains is small enough to minimize the light scattering intensity.[7] However, a notable decrease in the in-line transmission is observed at larger grain sizes. This is because the scattering cross section of the grains is now large enough to result in significant scattering, and the

intermediate crystallographic orientation results in a larger refractive index mismatch between adjacent grains that is unable to mitigate the scattering.
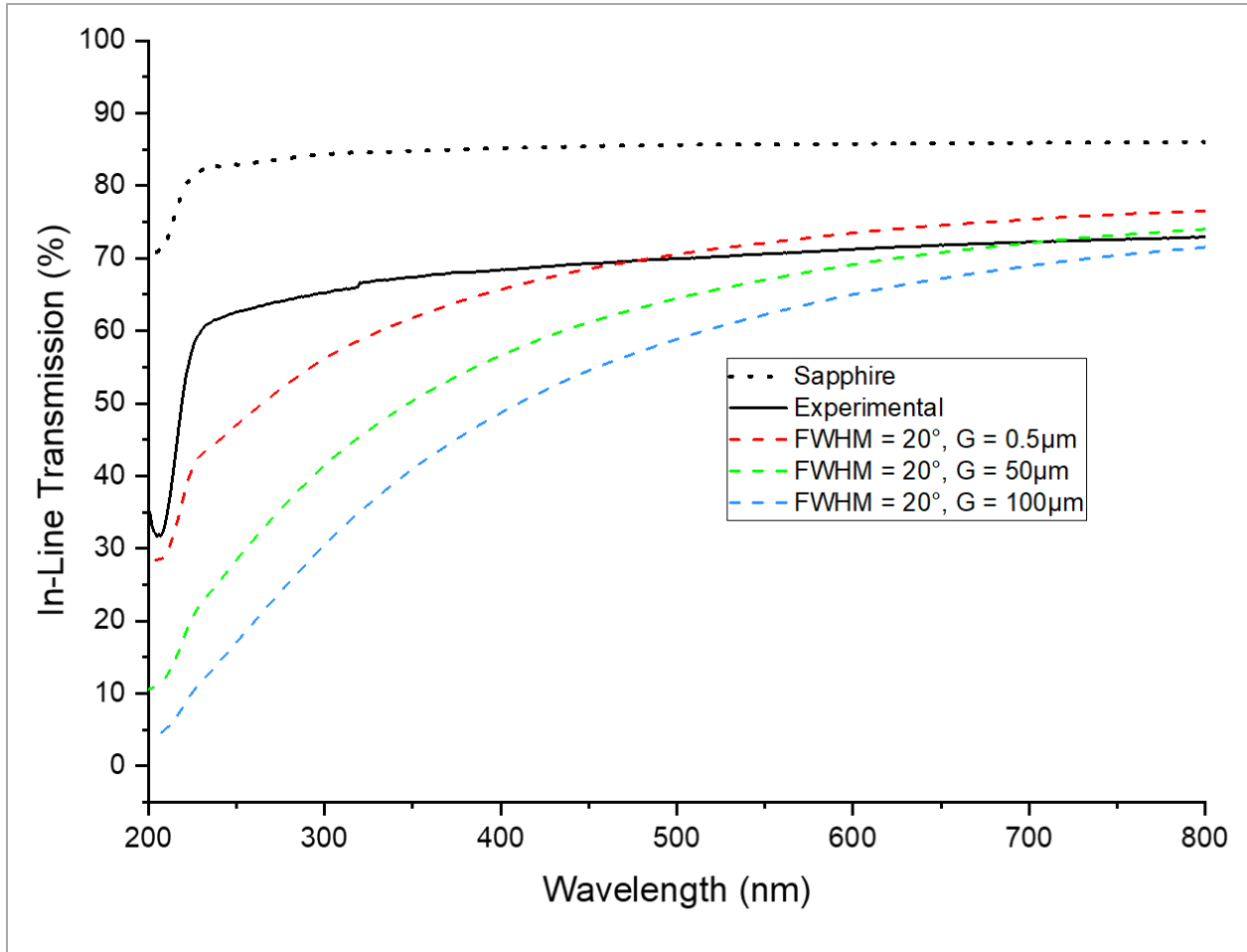
Figure 5.11. In-line transmission as a function of wavelength, illustrating how a grain size (G) affects the curve at intermediate degrees of crystallographic orientation (mid FWHM).

Grain size dependency becomes an even greater issue at low degrees of crystallographic orientation (FWHM = 45°, Figure 5.12). The intermediate and large grains (G = 50 & 100µm, respectively) result in a significant decrease in the in-line transmission, and high transparency is only achieved at a very small grain size (G = 0.5µm). In this hypothetical example, the large FWHM corresponds to effectively random crystallographic orientation, yielding a large refractive index mismatch that significantly scatters light.
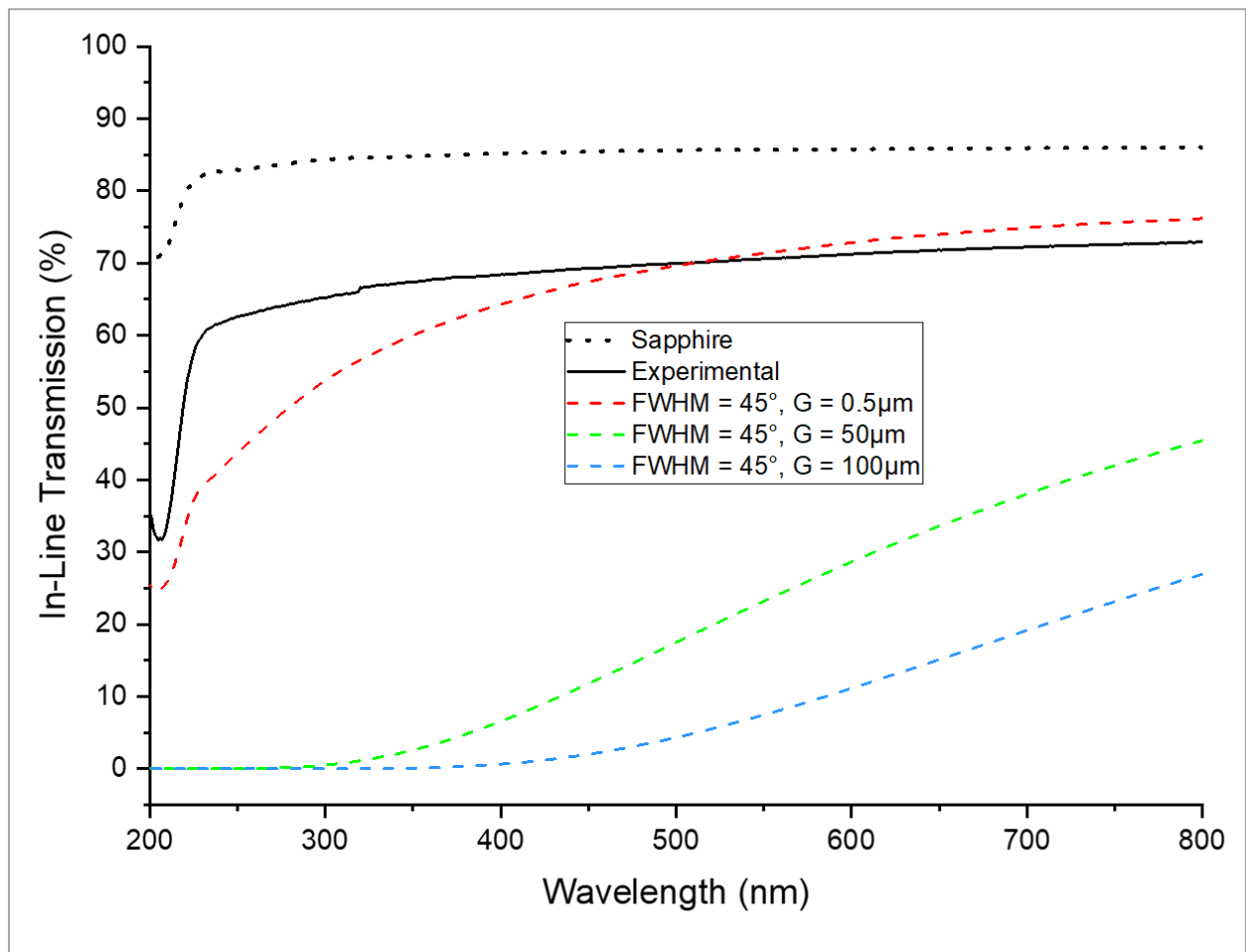
Figure 5.12. In-line transmission as a function of wavelength, illustrating how a grain size (G) affects the curve at low degrees of crystallographic orientation (high FWHM).

It is worth noting that in these hypothetical examples, the in-line transmission is still relatively high (T_{ILT} = 67% at 645nm) at large grain sizes (G = 100μm) with intermediate crystallographic orientation, as shown in Figure 5.11. This indicates that while grain size notably impacts in-line transmission of alumina, even an intermediate amount of crystallographic orientation can result in a high level of transparency. This suggests that there crystallographic orientation and grain size can be balanced during processing to achieve the desired properties. This emphasizes the importance of crystallographic alignment, and not just reducing grain size, for improving the optical properties of a birefringent ceramic like alumina.

5.5 Summary and Conclusions

The Rayleigh-Gans-Debye (RGD) model has been modified to account for several different wavelength-dependent variables: crystallographic orientation, absorption, porosity, and pore-size. When compared to an alumina sample with a high degree of crystallographic orientation and a large grain size, the modified RGD model matches the experimental data well. However, it does not predict differences between similarly aligned samples as well as expected, suggesting that more work must be done to confirm if some of the assumptions made during the derivation are valid. Additionally, hypothetical examples of varying crystallographic orientation and grain size have been performed, showing that even an intermediate amount of crystallographic orientation can significantly improve the optical properties at large grain sizes. Finally, this modified RGD model illustrates the importance of accounting for crystallographic orientation, which yields a more accurate representation of the optical data of birefringent ceramics such as alumina.

6. HOT-EXTRUSION OF ALUMINUM OXIDE

6.1   Contributions

The individuals listed below contributed the following tasks:

- Andrew Schlup: Pre-form fabrication, hot-extrusion, scanning electron microscopy, and data analysis

- Adam Smith: CAD of the graphite extrusion die

- Matthew Carr: Sample sectioning, density measurements, X-ray diffraction measurements, and data analysis.

6.2   Introduction

During preliminary testing in this research, the importance of straining and plastically deforming the sample during hot-pressing was observed, as higher degrees of strain lead to more primary recrystallization, resulting in greater densification.[14] Another processing method that can take advantage of the plastic deformation of alumina is hot-extrusion. Hot-extrusion of magnesia has been explored in the past, with promising results.[81–84] These methods involve pre-heating a magnesia rod and quickly transferring it to a tungsten extrusion can, where it is extruded at very high pressures and extrusion rates. Rice has discussed the unsuccessful attempts of extruding alumina, and has suggested that extrusion could be possible if the pre-form is heated in place and extruded at a much slower strain rate.[84] Additionally, Cheney explored the hot-extrusion of alumina powder in a molybdenum can, with minimal results.[85] Therefore, the feasibility of doing this at slow strain rates in a graphite die was explored.

A simple schematic of hot-extrusion of an alumina pre-form in a graphite die is shown in Figure 6.1. The alumina pre-form sits in-between two graphite wedges, and when the load is slowly applied at high temperatures, the pre-from should plastically deform and extrude through the decreasing cross section wedges. It is feasible that something like this could be scaled up to a large-scale continuous process, in which an alumina preform is partially extruded, the ram is backed out, another alumina pre-form is placed in the die, and the ram pushes on the new preform, which pushes on the first pre-form. A similar continuous hot-pressing method has already been shown to

be possible with alumina[4,34] and several other ceramics,[40] but this method only consolidates and densifies a powder charge; there is no bulk plastic deformation occurring. It is theorized that the plastic deformation that occurs during extrusion should result in densification of the preform, as well as some amount of crystallographic texture.
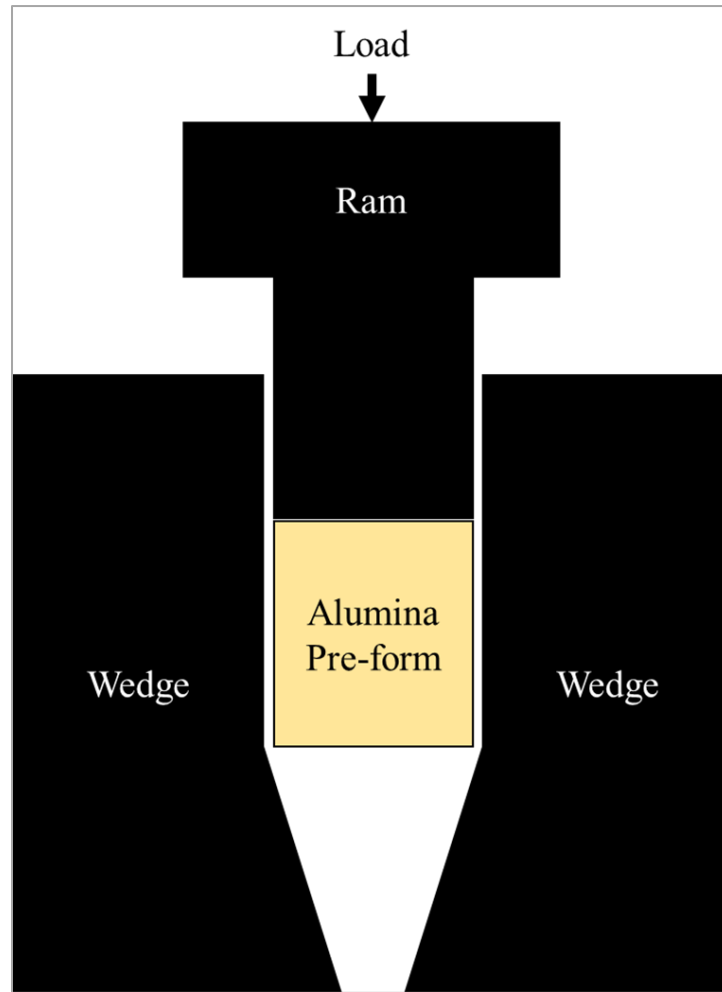
Figure 6.1. Schematic illustrating hot-extrusion of an alumina pre-form.

Initial testing with high density preforms ($\rho \approx 95\%$) yielded minimal results, as the part was simply too dense to extrude. Therefore, a pre-form with a lower density was prepared. A relative density of approximately 65% was chosen, as this is the density that Heuer et al.[13] observed their parts were at immediately prior to the forging step to create transparent alumina parts. It is thought that using a pre-form with this lower relative density will result in a greater degree of plastic deformation and hot-extrusion.

6.3 Experimental Methods

6.3.1 Pre-form Fabrication

An alumina pre-form was fabricated by hot-pressing and machining to a specific dimension. 117g of alumina powder with an equiaxed morphology (AA03, Sumitomo, 0.3-µm diameter) was poured into a 30x46.5mm rectangular graphite hot-press die. Graphoil and boron-nitride spray were used to separate the alumina powder from the graphite die parts. The hot-pressing procedure was similar to what is described in Section 3.3.2, except for the following parameters: T_{max} = 1200°C, t_{iso} = 30min, P_{max} = 10MPa, P_i = 1MPa, Pressure-application rate = 4.5MPa/min, Pressure-application Temperature = 1150°C, and a vacuum atmosphere of better than 112 millitorr (15Pa) maintained during the entire run. These parameters were chosen to intentionally produce a part with a relative density of approximately 65%.[13,45] The density of the pre-form was measured using the Archimedes method,[50] similar to what is discussed in Section 2.3.4., resulting in a relative density of 68.72%. The dimensions of the hot-pressed alumina part were approximately 30mm x 46.5mm x 25mm.

The hot-pressed alumina part was machined using a 150-grit resin-bonded diamond wheel and water lubricant to have the following dimensions: 1.5" x 1.125" x 0.75" (38.1mm x 28.6mm x 19.1mm). A slight chamfer was machined into the extrusion end of the pre-form, as shown in Figure 6.2.
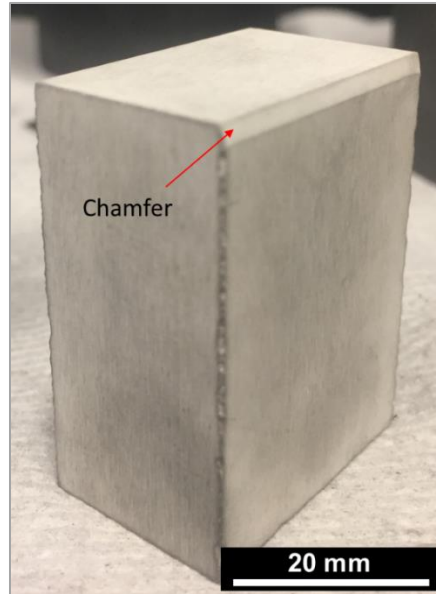

Figure 6.2. Macro image of the machined alumina pre-form.

6.3.2 Hot-Extrusion

A graphite die for hot-extrusion was designed via Computer Aided Design (CAD), as shown in Figure 6.3.a-b. The alumina pre-form was placed within the wedge-shaped graphite die, as shown in Figure 6.3.c. Graphoil, molybdenum foil, and boron-nitride spray were used to separate the extruded part from the graphite die, as well as assist in lubrication during extrusion. The wedges were shaped such that an extrusion ratio of 2:1 (50% reduction) could be achieved. The assembled extrusion die was placed in the resistively-heated graphite hot-press furnace (Centorr, Testorr[TM] series, and MTS, Model 312.21). and a vacuum was pumped for approximately 12 hours, until a 40 to 50 millitorr (5.3 to 6.7 Pa) vacuum was achieved. The furnace chamber was then backfilled with high-purity gettered nitrogen and allowed to flow continuously at approximately 4 liters/min and 2psi ($1.4x10^4$ Pa) for the duration of the hot-extrusion run. No load was applied to the extrusion assembly during heating at 25°C/min. When the extrusion temperature was reached (1800°C), the furnace was held for 5 minutes to allow the extrusion assembly to equilibrate in temperature. The load was manually applied at 0.5 kN increments, up to a maximum load of 7.0 kN (which corresponds to a pressure of approximately 12.8MPa). The maximum load was maintained until extrusion was complete (~4 minutes), wherein the load was removed and the furnace was shut off, allowing un-controlled cooling to room temperature. The displacement and load was recorded during the extrusion run.
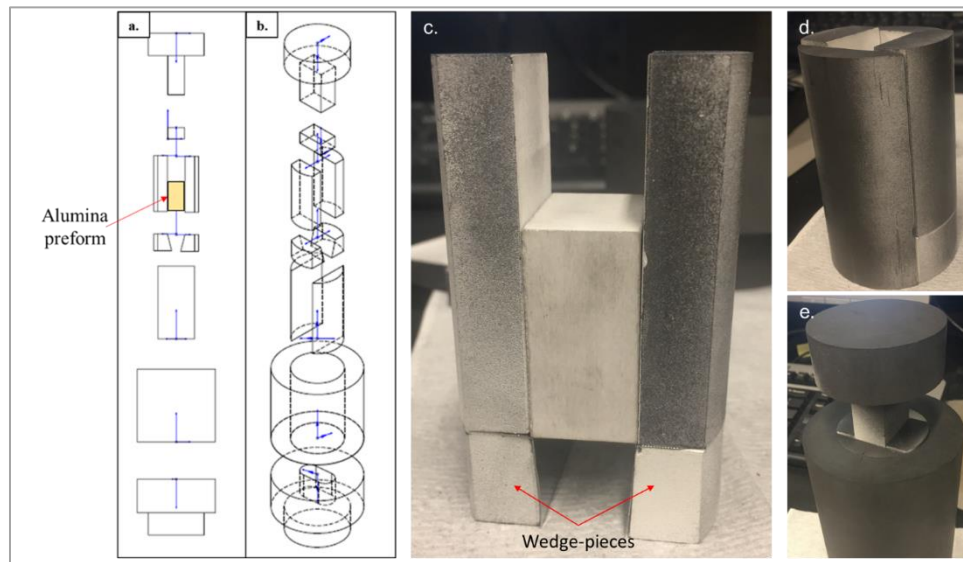
Figure 6.3. CAD drawing of the side (a.) and isometric (b.) views of the hot-extrusion die. The alumina pre-form sitting in above the wedge-pieces (c.), the assembly showing the D-spacers (d.), and the assembly showing the outer shell and extrusion ram (e.).

6.3.3 Sample Sectioning

The extruded alumina part was sectioned as shown in Figure 6.4. The relative density of each section was measured using the Archimedes method,[50] similar to what is discussed in Section 2.3.4. Samples were mounted such that the face of interest could be polished for further characterization.
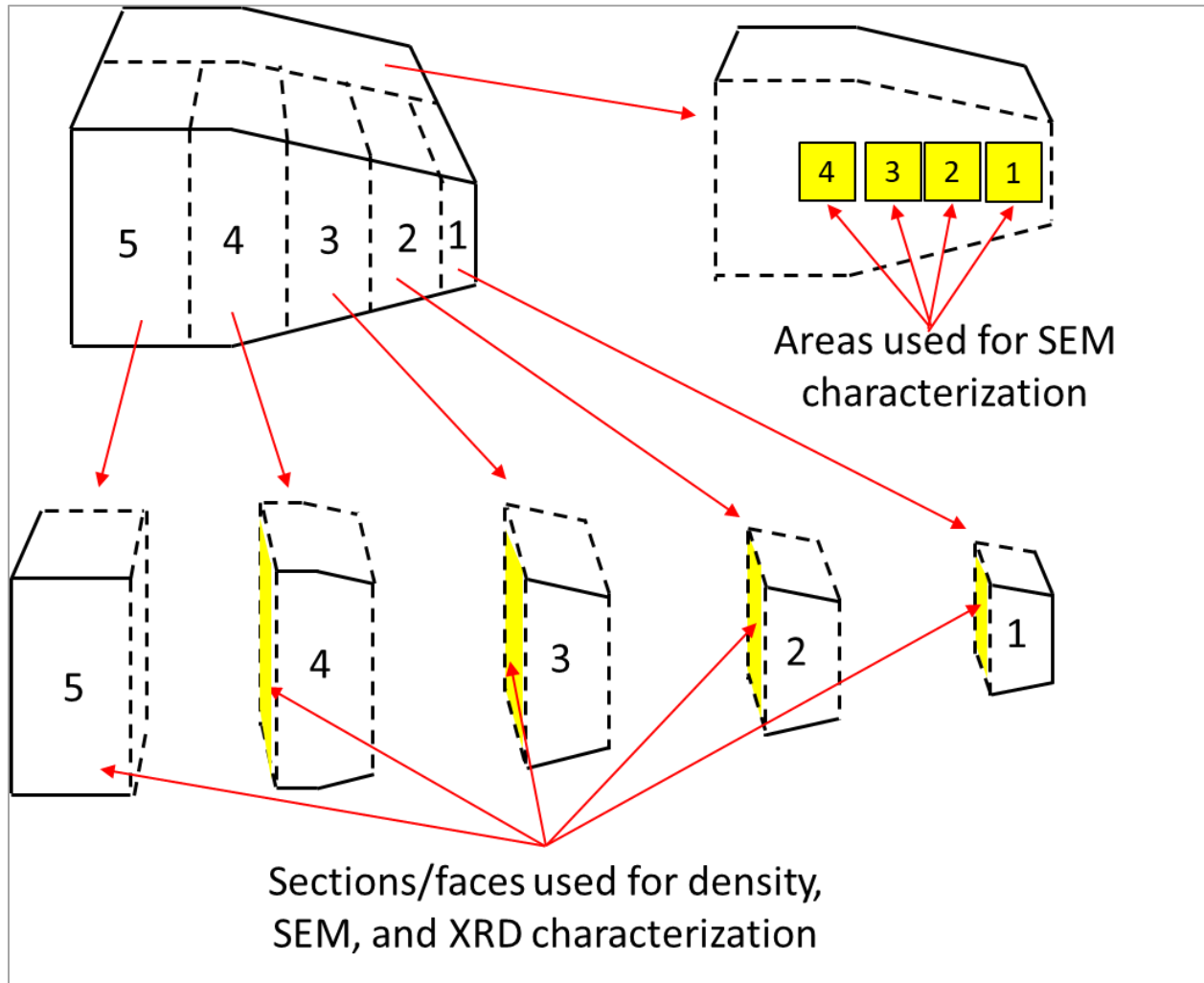
Figure 6.4. Schematic illustrating how the extruded sample was sectioned (dotted lines) for characterization. The highlighted areas indicate the areas/faces used for characterization.

6.3.4 Microstructural and Texture Characterization

The microstructure of the sectioned samples were characterized via SEM, similar to the methods described in Section 2.3.6. The crystallographic texture of the sectioned samples were semi-quantitatively measured via 2θ-XRD scans, as described in Section 2.3.5.

6.4   Results and Discussion

The extruded alumina part is shown in Figure 6.5, as well as how it appeared in the extrusion assembly immediately after extrusion. The difference between the initial state, extrusion zone, and fully extruded sections are evident. The sample decreased in width by approximately 7mm, or about 37%. The extrusion die was designed to result in a 50% reduction in width. This discrepancy is likely due to the graphoil that is used in the die design compressing during extrusion.

Figure 6.5. The alumina part after hot-extrusion.

Figure 6.6 shows the displacement and pressure data during the extrusion run. During the first 5 minutes of the extrusion run, the ram velocity is approximately 2.26 mm/min, then slows to approximately 0.55 mm/min for the duration of the extrusion run, even after the peak load of 7kN (~12.8MPa). Cheney et al.[85] reported significantly higher extrusion rates, on the order of 14,700 to 15,700 mm/min, with a peak load of ~2700kN (~400MPa). The significantly slower extrusion rates used in the current study are in agreement with the suggestions of Rice.[84]
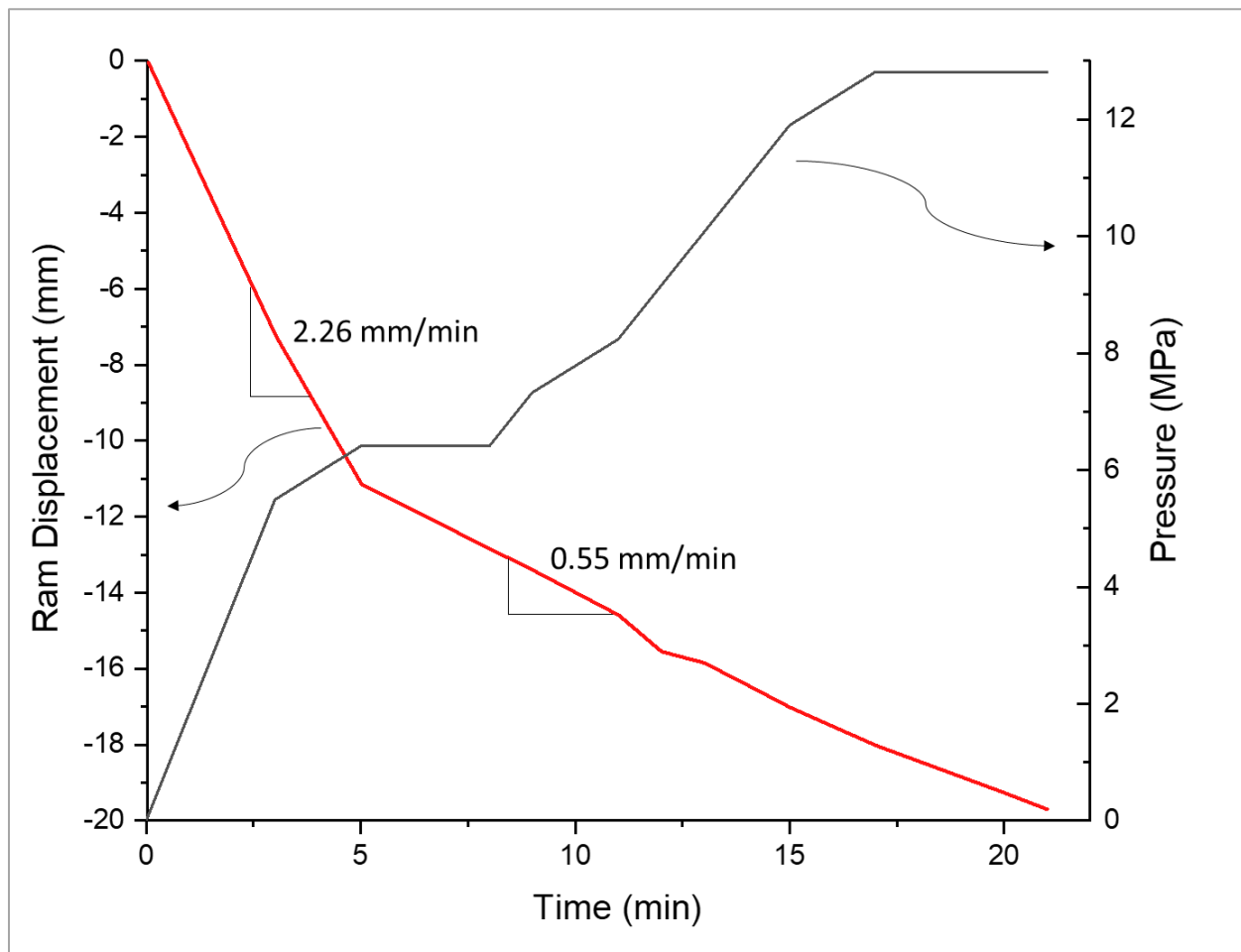
Figure 6.6. Ram displacement and pressure as a function of time during the hot-extrusion run.

Figure 6.7 shows the relative density as a function of extrusion distance. All sections experienced a significant increase in density from the initial 68.72%, indicating that this hot-extrusion method effectively causes the pre-form to densify, as expected. Additionally, the density of the extruded sections initially increase, then decrease, as they pass through the extrusion zone. The initial increase is expected, as the part should densify as it passes through the extrusion zone. In fact, the maximum relative density occurs after approximately 10mm of extrusion, which corresponds to the shift in ram velocity observed in Figure 6.6. The decrease in relative density of section 2 is not well understood and could simply be variation in the sample. The continued decrease in relative density of section 1, however, could likely be due to the pore-swelling phenomenon discussed in Section 2.4.3. As the pre-form moves through the extrusion zone, it should increase in density, as the wedges of the extrusion die contract more and more, causing the

pre-form to plastically deform and densify. However, when the end of the part exits the extrusion zone, there are no walls to continue to constrain the extruded section. If the pores in this extruded section are at a high pressure, then it is possible that the surrounding alumina microstructure will creep to relax the pressure within the pores, causing pore-swelling and de-densification.
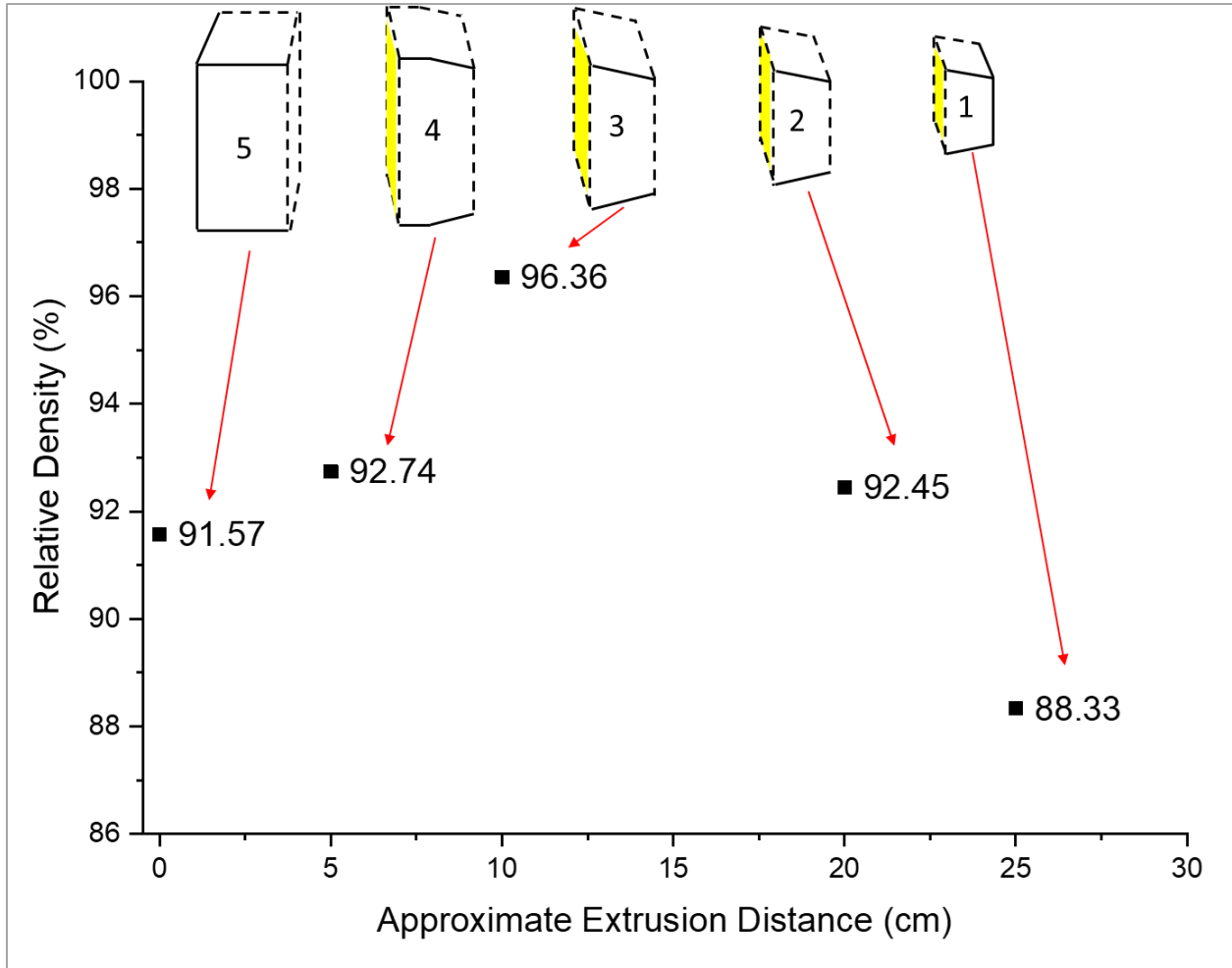
Figure 6.7. Relative density of the different extruded sections.

Figure 6.8 and Figure 6.9 show SEM micrographs of the extruded samples. Contrary to expectations, no morphological texture is observed in the microstructure, even at the fully-extruded section (section 1). The porosity of the different sections, however, do appear to correspond with changes in relative density in Figure 6.7. Cheney observed extensive morphological texture in the extruded alumina sections, likely due to their very high extrusion rates.[85] They observed minimal porosity, but there was extensive amounts of a liquid phase along

the grain boundaries. The liquid phase was not identified, though it could have been molybdenum from the molybdenum can that the alumina was extruded within. This liquid molybdenum phase could have helped to promote the morphological texture during extrusion.
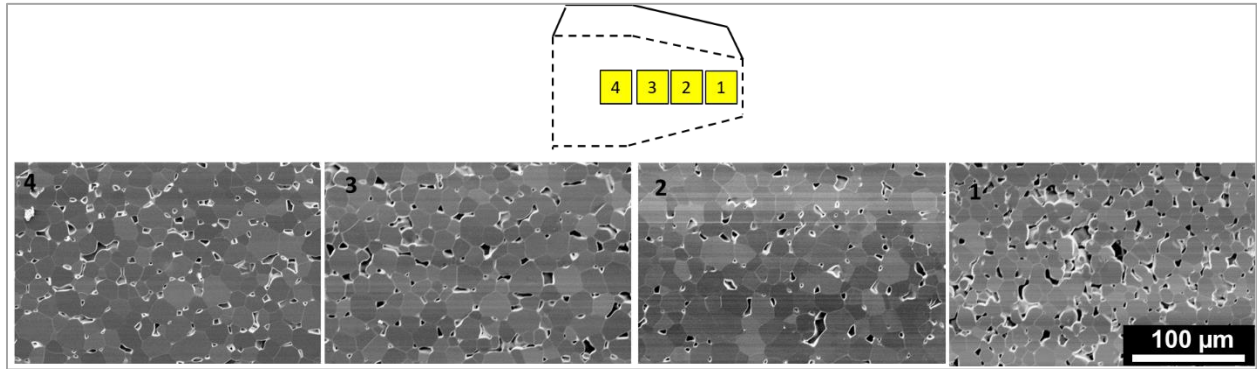
Figure 6.8. SEM micrographs of the extruded sections.
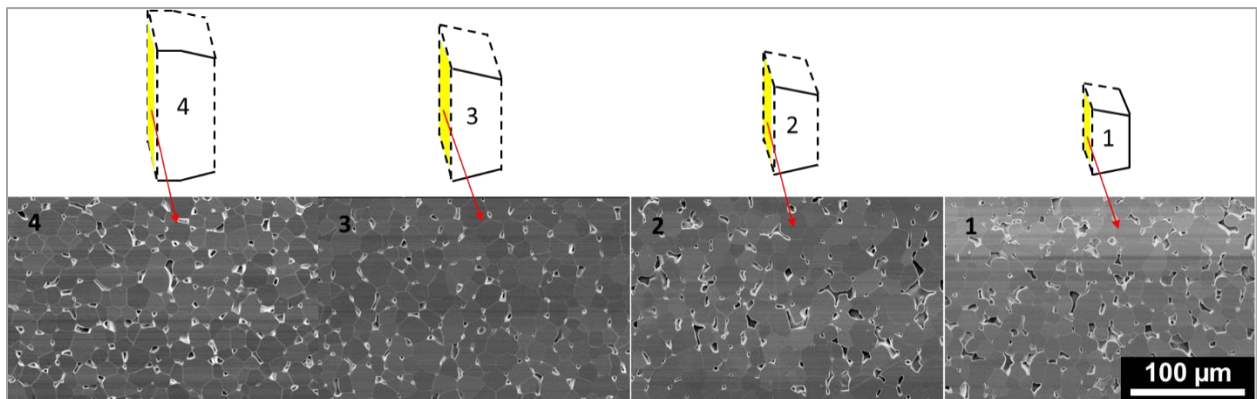
Figure 6.9. SEM micrographs of the extruded sections.

Figure 6.10 shows the 2θ XRD curves for the extruded sections. It can be seen that the intensity of the (110) and (300) peaks are increasing with sections that were pushed further through the extrusion zone. The (110) and (300) peaks correspond to the a-plane of alumina,[15] which is perpendicular to the c-plane of alumina. Yi et al.[15] observed a similar trend in magnetically aligned alumina, where the side of the sample oriented perpendicular to magnetic field direction experienced significant increases in the intensity of the (110) and (300) peaks. Given the extrusion orientation used in this study, plastic deformation should occur such that the c-plane of the alumina crystal structure will orient parallel to the extrusion direction, which results in the a-plane being perpendicular to the extrusion direction. Cheney did not report results regarding crystallographic

texture.[85] Heuer et al,[14] however, did observe crystallographic texture when hot-forging alumina, where the c-plane oriented parallel to the direction of radial strain. This increase in peak intensity shows that the hot-extrusion method used in this study is effective in crystallographically orienting alumina.
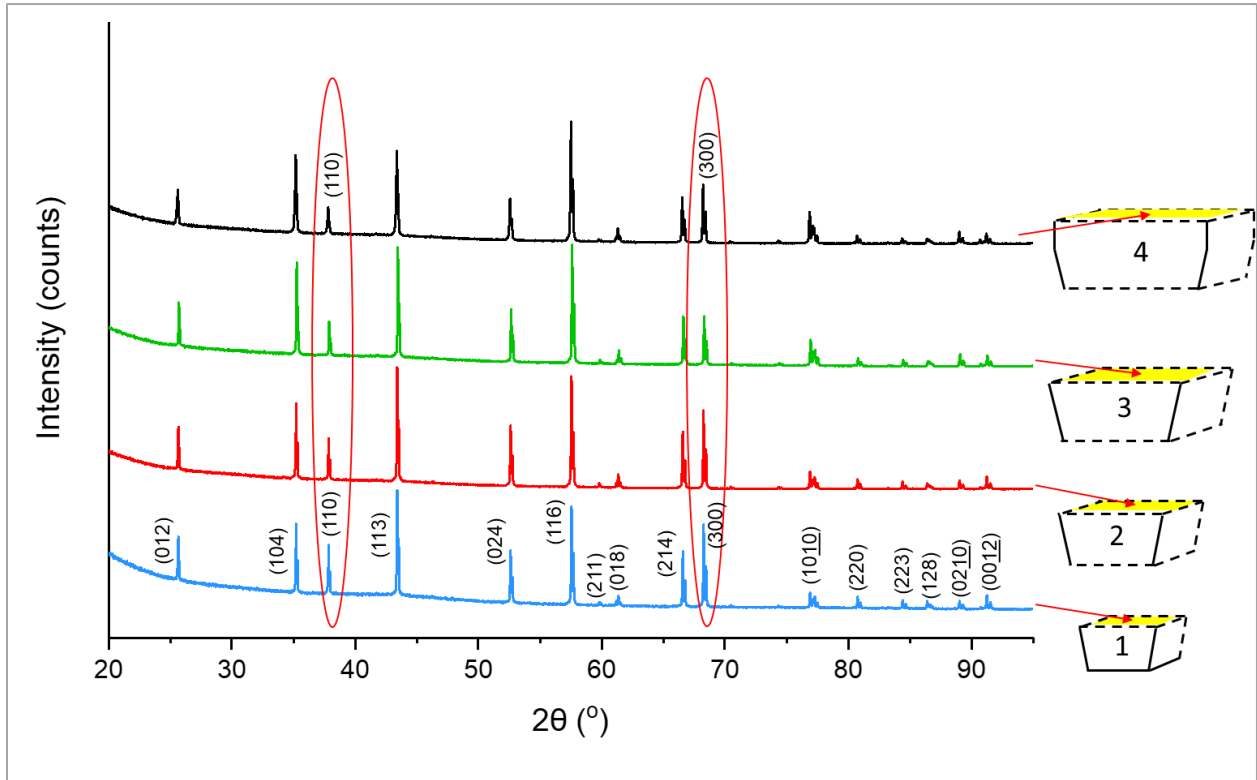
Figure 6.10. XRD scans of the extruded sections, with arrows indicating the face that was scanned.

6.5   Summary and Conclusions

Alumina pre-forms were processed and machined for hot-extrusion. A novel graphite hot-extrusion method was used, in which the alumina pre-form was extruded at a high temperature (1800°C), a low rate (0.55 to 2.26 mm/min), and a low pressure (≤12.8MPa). An overall increase in the density of the extruded part was observed, and a decrease in density of the section that exited the extrusion zone. This decrease in density is attributed to a pore-swelling phenomenon. No morphological texture is observed in the microstructures. However, noticeable crystallographic texture was confirmed via XRD, suggesting that this hot-extrusion method effectively orients alumina.

114

REFERENCES

1.   Harris DC, Johnson LF, Zelmon DE, Poston WB, Kunkel JD, Pascucci MR, et al. Refractive index of infrared- transparent polycrystalline alumina. Opt Eng. 2017;56(7).

2.   Krell A, Klimke J, Hutzler T. Advanced spinel and sub-μm Al2O3 for transparent armour applications. J Eur Ceram Soc. 2009;29(2):275–81.

3.   Krell A, Klimke J, Hutzler T. Transparent compact ceramics: Inherent physical issues. Opt Mater (Amst). 2009;31(8):1144–50.

4.   Peelen JGJ. Transparent hot-pressed alumina, II: Transparent versus translucent alumina. Ceram Int. 1979;5(3):115–9.

5.   Mao X, Wang S, Shimai S, Guo J. Transparent polycrystalline alumina ceramics with orientated optical axes. J Am Ceram Soc. 2008;91(10):3431–3.

6.   Hayashi K, Kobayashi O, Toyoda S, Morinaga K. Transmission Optical Properties of Polycrystalline Alumina with Submicron Grains. Vol. 32, Materials Transactions, JIM. 1991. p. 1024–9.

7.   Apetz R, Bruggen MPB Van. Transparent Alumina : A Light-Scattering Model. J Am Ceram Soc. 2003;86(3):480–6.

8.   Krell A, Hutzler T, Klimke J. Physics and Technology of Transparent Ceramic Armor : Sintered Al2O3 vs Cubic Materials. In: Nanomaterials Technology for Military Vehicle Structural Applications. 2005. p. 14-1-14–10.

9.   Krell A, Blank P, Ma H, Hutzler T, Van Bruggen MPB, Apetz R. Transparent Sintered Corundum with High Hardness and Strength. Am Ceram Soc. 2003;86(1):12–8.

10.   Liu P, Yi H, Zhou G, Zhang J, Wang S. HIP and pressureless sintering of transparent alumina shaped by magnetic field assisted slip casting. Opt Mater Express. 2015;5(2):441.

11.   Pringuet A, Takahashi T, Baba S, Kamo Y, Kato Z, Uematsu K, et al. Fabrication of Transparent Grain-Oriented Polycrystalline Alumina by Colloidal Processing. Am Ceram Soc. 2016;99(10):3217–9.

12.   Rhodes WH, Sellers DJ, Vasilos T. Hot-Working of Aluminum Oxide: 11, Optical Properties. J Am Ceram Soc. 1974;58(1–2):31–4.

13.   Rhodes WH, Sellers DJ, Heuer AH, Vasilof T. Development And Evaluation Of Transparent Aluminum Oxide. Lowell, MA; 1967.

14.   Heuer AH, Sellers DJ, Rhodes WH. Hot working of aluminum oxide. 1: Primary recrystallization and texture. J Amer Ceram Soc. 1969;52:468–74.

15.   Yi H, Mao X, Zhou G, Chen S, Zou X, Wang S, et al. Crystal plane evolution of grain oriented alumina ceramics with high transparency. Ceram Int. 2012 Sep;38(7):5557–61.

16.	Ashikaga T, Kim BN, Kiyono H, Suzuki TS. Effect of crystallographic orientation on transparency of alumina prepared using magnetic alignment and SPS. J Eur Ceram Soc. 2018;38(7):2735–41.

17.	Harris DC, Johnson LF, Cambrea LR, Baldwin L, Baronowski M, Zelmon DE, et al. Refractive index of infrared-transparent polycrystalline alumina. In: Window and Dome Technologies and Materials XV. 2017.

18.	Su X, Li S, Li J. Effect of potassium sulfate on the low-temperature formation of alpha alumina platelets from bayerite. J Am Ceram Soc. 2010;

19.	Su X, Li J. Low Temperature Synthesis of Single-crystal Alpha Alumina Platelets by Calcining Bayerite and Potassium Sulfate. J Mater Sci Technol. 2011;

20.	Hsiang HI, Chen TH, Chuang CC. Synthesis of α-alumina hexagonal platelets using a mixture of boehmite and potassium sulfate. J Am Ceram Soc. 2007;

21.	Trice RW, Halloran JW. Investigation of the physical and mechanical properties of hot-pressed boron nitride/oxide ceramic composites. J Am Ceram Soc. 1999;82(9):2563–5.

22.	Miklos F, Hunt M, Villalobos G, Baker C, Bayya S, Sanghera J, et al. Low absorption magnesium aluminate spinel windows for high energy laser applications. J Mater Res. 2014;29(19):2266–71.

23.	Morita K, Kim BN, Yoshida H, Hiraga K, Sakka Y. Spectroscopic study of the discoloration of transparent MgAl2O4spinel fabricated by spark-plasma-sintering (SPS) processing. Acta Mater. 2015;84:9–19.

24.	Rubat Du Merac M, Reimanis IE, Smith C, Kleebe HJ, Müller MM. Effect of impurities and LiF additive in hot-pressed transparent magnesium aluminate spinel. Int J Appl Ceram Technol. 2013;10:E33–48.

25.	Schlup AP, Costakis WJ, Rheinheimer W, Trice RW, Youngblood JP. Hot-pressing platelet alumina to transparency. J Am Ceram Soc. 2019;103(4):2587–601.

26.	Zhang X, Liang S, Zhang P, Zhao T, Bai Y, Bao CG, et al. Fabrication of transparent alumina by rapid vacuum pressureless sintering technology. J Am Ceram Soc. 2012;95(7):2116–9.

27.	Coble RL. Unitest States Patent: Transparent Alumina and Method of Preparation. United States: United States Patent Office; 3,026,210, 1962.

28.	Jiang D, Hulbert DM, Anselmi-Tamburini U, Ng T, Land D, Mukherjee AK. Optically Transparent Polycrystalline Al2O3 Produced by Spark Plasma Sintering. J Am Ceram Soc. 2007;91(1):151–4.

29.	Prakasam M, Michau D, Viraphong O, Largeteau A. Optimal sintering parameters for Al2O3 optoceramics with high transparency by spark plasma sintering. Adv Appl Ceram. 2016;115(6):333–41.

30.	Kim BN, Hiraga K, Morita K, Yoshida H, Miyazaki T, Kagawa Y. Microstructure and optical properties of transparent alumina. Acta Mater. 2009;57(5):1319–26.

31.   Kim BN, Hiraga K, Morita K, Yoshida H. Effects of heating rate on microstructure and transparency of spark-plasma-sintered alumina. J Eur Ceram Soc. 2009;29(2):323–7.

32.   Kim BN, Hiraga K, Morita K, Yoshida H. Spark plasma sintering of transparent alumina. Scr Mater. 2007;57:607–10.

33.   Grasso S, Yoshida H, Porwal H, Sakka Y, Reece M. Highly transparent α-alumina obtained by low cost high pressure SPS. Ceram Int. 2013;39(3):3243–8.

34.   Peelen JGJ. Transparent Hot-pressed Alumina. I: Hot pressing of alumina. Ceramurg Int. 1979;5(2):70–5.

35.   Fu P, Xu Y, Shi H, Zhang B, Ruan X, Lu W. The effect of annealing process on the optical and microwave dielectric properties of transparent MgAl2O4ceramics by spark plasma sintering. Opt Mater (Amst). 2014;36(7):1232–7.

36.   Morita K, Kim BN, Yoshida H, Hiraga K, Sakka Y. Influence of spark plasma sintering (SPS) conditions on transmission of MgAl2O4spinel. J Am Ceram Soc. 2014;98(2):378–85.

37.   Wang C, Zhao Z. Transparent MgAl2O4 ceramic produced by spark plasma sintering. Scr Mater. 2009;61(2):193–6.

38.   Vu MT. Densification and Characterization of Transparent Polycrystalline Spinel Produced by Spark Plasma Sintering. Rutgers; 2014.

39.   Rubat Du Merac M, Kleebe HJ, Müller MM, Reimanis IE. Fifty years of research and development coming to fruition; Unraveling the complex interactions during processing of transparent magnesium aluminate (MgAl 2 O 4) spinel. J Am Ceram Soc. 2013;96(11):3341–65.

40.   Munir ZA, Anselmi-Tamburini U, Ohyanagi M. The effect of electric field and pressure on the synthesis and consolidation of materials: A review of the spark plasma sintering method. J Mater Sci. 2006;41(3):763–77.

41.   Coble RL. Mechanisms of Densification During Hot-Pressing. In: Sintering and Related Phenomena. 1965. p. 329–50.

42.   Coble RL. Diffusion Models for Hot Pressing with Surface Energy and Pressure Effects as Driving Forces. J Appl Phys. 1970;41(12):4798–807.

43.   McClelland JD. Kinetics of hot-pressing. At Int. 1961;

44.   McClelland JD, Zehms EH. End-Point Density of Hot-Pressed Alumina. Am Ceram Soc. 1962;46(2):77–80.

45.   Mangsen GE, Lambertson WA, Best B. Hot Pressing of Aluminium Oxide. J Am Ceram Soc. 1960;43(2):55–9.

46.   Rice RW. Fabrication and Characterization Of Hot Pressed Al2O3. 1970.

47.   Oudemans GJ. Continuous hot pressing. Philips Tech Rev. 1968;2(2):45–54.

48. Sellers, D J P, Rhodes, W H L, Vasilos, T W. United States Patent, Method of Preparing Transparent Alumina. United States: United States Patent Office; 3,899,560, 1975.

49. Halmann M, Steinfeld A, Epstein M, Vishnevetsky I. Vacuum carbothermic reduction of alumina. Miner Process Extr Metall Rev. 2014;35(2):126–35.

50. ASTM Standard C693, 1993 (2013) Standard Test Method for Density of Glass by Buoyancy. ASTM International. 2013. 1–3 p.

51. Foster LM, Long G, Hunter MS. Reactions Between Aluminum Oxide and Carbon: The Al2O3-Al4C3 Phase Diagram. J Am Ceram Soc. 1956;39(1):1–11.

52. Morita K, Kim BN, Yoshida H, Hiraga K, Sakka Y. Influence of pre- and post-annealing on discoloration of MgAl2O4spinel fabricated by spark-plasma-sintering (SPS). J Eur Ceram Soc. 2016;36(12):2961–8.

53. Siriwardane R V., Poston JA, Robinson C, Simonyi T. Effect of additives on decomposition of sodium carbonate: Precombustion CO2 capture sorbent regeneration. Energy and Fuels. 2011;25(3):1284–93.

54. Wigmans T, van Doorn J, Moulijn JA. Temperature-programmed desorption study of Na2CO3-containing activated carbon. Fuel. 1983;62(2):190–5.

55. Rahaman MN. Ceramic Processing and Sintering. 2nd ed. 2003.

56. Seabaugh MM, Vaudin MD, Cline JP, Messing GL. Comparison of Texture Analysis Techniques for Highly Oriented α-Al2O3. J Am Ceram Soc. 2004;

57. Vaudin MD, Rupich MW, Jowett M, Riley GN, Bingert JF. A method for crystallographic texture investigations using standard x-ray equipment. J Mater Res. 1998;13(10):2910–9.

58. Costakis WJ, Schlup AP, Youngblood JP, Trice RW. Aligning α-Alumina Platelets via Uniaxial Pressing of Ceramic-filled Thermoplastic Polymer Blends for the Improvement of Final Sintered Transparency. J Am Ceram Soc. 2020;103(6):3500–12.

59. REED JS. Principles of Ceramics Processing. 2nd ed. 1995. 617 p.

60. Seabaugh MM, Kerscht IH, Messing GL. Texture Development by Templated Grain Growth in Liquid-Phase-Sintered-Alumina. J Am Ceram Soc. 1997;80(5):1181–8.

61. Reed JS. Introduction to the principles of ceramic processing. New York: Wiley; 1988.

62. International A. Standard Test Method for Flexural Strength of Advanced Ceramics at Ambient Temperature. Order A J Theory Ordered Sets Its Appl. 2018;94(Reapproved):1–15.

63. International A. Standard Test Method for Vickers Indentation Hardness of Advanced Ceramics 1. ASTM International. 2019. 1–10 p.

64. Shi XL, Xu FM, Zhang ZJ, Dong YL, Tan Y, Wang L, et al. Mechanical properties of hot-pressed Al2O3/SiC composites. Mater Sci Eng A. 2010;527(18–19):4646–9.

65. Kingery WD. Introduction to Ceramics. John Wiley & Sons, Inc.; 1960.

66.	Wachtman J, Cannon W, Matthewson M. Mechanical Properties of Ceramics. 2009.

67.	Heuer AH, Rhodes WH, Sellers DJ, Vasilos T. Microstructure Studies of Polycrystalline Refractory Oxides. 1967;(March 1966).

68.	Parish M V., Pascucci MR, Gannon JJ, Harris DC. Strength characteristics of transparent alumina and spinel ceramics. In: Window and Dome Technologies and Materials XV. 2017.

69.	Zhang M, Chang Y, Bermejo R, Jiang G, Sun Y, Wu J, et al. Improved fracture behavior and mechanical properties of alumina textured ceramics. Mater Lett. 2018;221:252–5.

70.	Carisey T, Leviri I, Brandon DG. Micro structure and mechanical properties of textured Al2O3. J Eur Ceram Soc. 1995;

71.	Sinani AB, Dynkin NK, Lytvinov LA, Konevsky P V, Andreev EP. Sapphire Hardness in Different Crystallographic Directions. Bull Russ Acad Sci. 2009;73(10):1380–2.

72.	Thomas ME. Vacuum-ultraviolet characterization of sapphire, ALON, and spinel near the band gap. Opt Eng. 1993;32(6):1340.

73.	Guo J, Ellis DE, Lam DJ. Electronic structure and energetics of sapphire (0001) and (11»02) surfaces. Phys Rev B. 1992;45(23):13647–56.

74.	Peck ER, Khanna BN. Dispersion of Nitrogen*. J Opt Soc Am. 1966;56(8):1059.

75.	Peck ER, Fisher DJ. Dispersion of Argon. J Opt Soc Am. 1964;54(11):1362–4.

76.	Ciddor PE. Refractive index of air: new equations for the visible and near infrared. Appl Opt. 1996;35(9):1566.

77.	Cuthbertson C, Cutherbertson M. On the Refraction and Dispersion of Carbon Dioxide , Carbon Monoxide , and Their Relations. Proc R Soc London Ser A, Contain Pap a Math Phys Character. 1910;83(561):151–71.

78.	Dalisa AL, Seymour RJ. Convolution Scattering Model for Ferroelectric Ceramics and Other Display Media. 1973;61(7).

79.	Raman C V., Viswanathan KS. The theory of the propagation of light in polycrystalline media. Proc Indian Acad Sci - Sect A. 1955;41(2):37–44.

80.	Kuna L, Mangeri J, Gorzkowski EP, Wollmershauser JA, Nakhmanson S. Mesoscale modeling of polycrystalline light transmission. Acta Mater [Internet]. 2019;175:82–9. Available from: https://doi.org/10.1016/j.actamat.2019.06.001

81.	Rice RW. Effect of Hot Extrusion, Other Constituents, and Temperature on the Strength and Fracture of Polycrystalline MgO. J Am Ceram Soc. 1993;76(12):3009–18.

82.	Rice RW, Hunt JG. Identifying Optimum Parameters of Hot Extrusions. 1965.

83.	Rice RW. 11. Hot Forming of Ceramics. 1970;

84.   Rice RW. Hot-Working of Oxides. Vol. 5, Magnesia, Alumina, Beryllia Ceramics: Fabrication, Characterization and Properties: High Temperature Oxides, Part III. ACADEMIC PRESS, INC.; 1970. 235–280 p.

85.   Cheney R. Studies Of The Brittle Behavior Of Ceramic Materials. Dayton, OH; 1964.

PUBLICATIONS

Published Articles

1. Schlup AP, Costakis WJ, Rheinheimer W, Trice RW, Youngblood JP. Hot-pressing Platelet Alumina to Transparency. Am Ceram Soc. 2019;103(4):2587–601.

2. Costakis WJ, Schlup AP, Youngblood JP, Trice RW. Aligning α-Alumina Platelets via Uniaxial Pressing of Ceramic-filled Thermoplastic Polymer Blends for the Improvement of Final Sintered Transparency. J Am Ceram Soc. 2020;103(6):3500–12.

In Preparation

1. A. Schlup, W. Costakis, J. Youngblood, R. Trice, Density Gradients in Transparent Pre-Aligned Platelet Alumina Processed via Hot-Pressing, (In Preparation)

2. A. Schlup, W. Costakis, J. Youngblood, R. Trice, Mechanical Properties of Transparent Alumina Produces via Hot-Pressing Pre-Aligned Platelet Alumina, (In Preparation)

3. A. Schlup, W. Costakis, R. Trice, J. Youngblood, Modifications to the Rayleigh-Gans-Debye Model for Crystallographically-Aligned Transparent Alumina, (In Preparation)

4. W.J. Costakis, A.P. Schlup, C. Meisel, J.P. Youngblood, R.W. Trice, Aligning α-Alumina Platelets via Direct Ink Writing for Sintered Transparency, (In Preparation).

5. W.J. Costakis, A.P. Schlup, J.P. Youngblood, R.W. Trice, Hot-Pressing of Equiaxed and Platelet Alumina Powders to Transparency, (In Preparation).

VITA

Andrew Schlup was born in Tacoma WA, and grew up in Pierce City, MO on his parents' cattle ranch. He attended Pierce City High School, then attended Missouri University of Science and Technology (Missouri S&T) in Rolla MO, earning a bachelor's degree in Ceramic Engineering. While at Missouri S&T, he worked as an undergraduate researcher working on various ceramic processing projects, including plasma-arc-welding of ultra-high-temperature ceramics, alumino-silicate sealing glass, and cemented carbides. He also had two separate internships. The first was at Dal-Tile International in El Paso TX, working on ceramic wall tiles, and the second was at G.E. Aviation in Evandale OH, working on advanced ceramics for turbine engines. Andrew has accepted a position with UES in Dayton OH, where he will work as a Research Scientist at the Air Force Research Lab upon the completion of his PhD at Purdue. When not playing in a lab making cool things out of ceramics, Andrew enjoys downhill longboarding and spending time with friends and family.